Multimodality Approach to Predicting Response of Vestibular Schwannomas to Radiation Therapy

by

Megan Margaret Jean Twiss

B.Sc. (Honours), Acadia University, 2006

A THESIS SUBMITTED IN PARTIAL FULFILLMENT OF
THE REQUIREMENTS FOR THE DEGREE OF

Master of Science

in

The Faculty of Graduate Studies

(Physics)

The University of British Columbia

(Vancouver)

January, 2009

© Megan Margaret Jean Twiss 2009

Abstract

Despite that most vestibular schwannomas are successfully treated with radiotherapy, current follow-up protocols entail years of serial magnetic resonance imaging (MRI) scans to ensure cessation of growth. This pilot study sought to identify early predictors of radiation treatment response using a non-invasive multi-modality imaging approach. We hypothesized that by combining information acquired from dynamic contrast-enhanced MRI (DCE-MRI), diffusion tensor imaging (DTI), and L-^{11}C-methionine positron emission tomography (MET-PET) treatment response could be identified sooner than the current several year waiting period. This thesis presents the baseline MRI and MET-PET results of the pilot study acquired to-date with follow-up data to be acquired in the next six months.

Baseline results suggest that DTI and DCE-MRI yield information that may be useful in identifying the response of vestibular schwannomas to radiotherapy. In particular, vestibular schwannomas display elevated mean diffusion coefficients relative to the contra-lateral cerebellum. Also, the novel use of arterial input functions derived from the anterior inferior cerebellar arteries has led to the successful implementation of DCE-MRI pharmaco-kinetic models which may be used to quantitatively monitor tumor response to radiotherapy. Furthermore, MET-PET has shown promise as a tool for evaluating response as all tumors exhibited enhancement under this modality as compared to the contra-lateral side of the brain. Single-voxel spectroscopy with 3T MRI has proven to be a poor technique with which to examine vestibular schwannomas since only two of eight spectra were acquired successfully. All of the techniques that have shown promise as investigatory tools of tumor response can potentially be implemented clinically in the near future.

Table of Contents

Abstract ii

Table of Contents iii

List of Tables vi

List of Figures vii

List of Abbreviations xi

Acknowledgements xii

Dedication xiii

1 Introduction 1
- 1.1 Motivation 1
- 1.2 Objectives 2

2 Background 3
- 2.1 Vestibular Schwannoma 3
  - 2.1.1 History 3
  - 2.1.2 Epidemiology 4
  - 2.1.3 Anatomical and Pathological Description 4
  - 2.1.4 Clinical Features and Diagnosis 7
- 2.2 Radiotherapy 8
  - 2.2.1 Stereotactic Radiosurgery and Fractionated Stereotactic Radiotherapy 8
  - 2.2.2 Radiation Biology 9
  - 2.2.3 Radiotherapy of Vestibular Schwannomas 12
- 2.3 Magnetic Resonance Imaging 19
  - 2.3.1 Magnetization and Signal Generation 19
  - 2.3.2 Spin Dynamics and Relaxation 21

2.3.3 Dynamic Contrast-Enhanced Magnetic Resonance Imaging . . . 22
2.3.4 Diffusion Tensor Imaging . . . 30
2.3.5 Magnetic Resonance Spectroscopy . . . 34
2.4 Positron Emission Tomography . . . 41
2.4.1 Imaging with Radioisotopes . . . 41
2.4.2 Positron Emission Tomography Overview . . . 42
2.4.3 Corrections . . . 45
2.4.4 Image Reconstruction . . . 45
2.4.5 Positron Emission Tomography of Brain Tumors with ^{11}C-Methionine . . . 46
2.4.6 ^{11}C-Methionine Positron Emission Tomography of Vestibular Schwannomas . . . 49

3 Materials and Methods . . . 51
3.1 Experimental Design . . . 51
3.2 Protocols . . . 52
3.2.1 Radiotherapy . . . 52
3.2.2 3T Magnetic Resonance Imaging . . . 53
3.2.3 1.5T Magnetic Resonance Imaging . . . 53
3.2.4 Positron Emission Tomography . . . 54
3.3 Analysis . . . 55
3.3.1 PET Reconstruction, Image Registration, and Regions of Interest . . . 55
3.3.2 Functional MRI Analysis . . . 55
3.3.3 PET . . . 59
3.3.4 Statistical Analysis . . . 59

4 Results . . . 61
4.1 Representative Case Studies . . . 61
4.2 Region of Interest Results . . . 73
4.2.1 DCE-MRI Results . . . 73
4.2.2 DTI Results . . . 78
4.3 MET-PET Results . . . 82
4.4 Single-voxel MRS . . . 85

5 Discussion . . . 88
5.1 DCE-MRI . . . 88
5.2 DTI . . . 89
5.3 MET-PET . . . 90

5.4 Spectroscopy 91
5.5 Summary of author's contributions 91

6 Conclusions 93

Bibliography 95

Appendices 103

List of Tables

2.1 Description of primary brain metabolites [63]. 39

3.1 Summary Patient Data 52
3.2 Summary Patient PET Data 54

List of Figures

2.1 Flip angle to optimize contrast and signal as a function of T_1 for $T_R = 4.3\ ms$. The range expected is $200 - 1800\ ms$ with T_1 values shortening with contrast arrival. 27
2.2 Two-compartment model of contrast-agent dynamics. 29
2.3 Single-shot EPI pulse sequence showing sequential coverage of FOV in k-space. G_x represents gradients applied along the x axis, while G_y shows gradients applied in the y direction. Echoes (when signal is acquired) are shown along the *Signal* axis of the diagram [2]. 33
2.4 PRESS imaging sequence. Notice the slice selective gradients applied along three orthogonal directions (G_m, G_p, and G_s) during the application of excitation pulses. Spoiling gradients are used before and after refocussing pulses to destroy undesirable magnetization [2]. 36
2.5 Cross-section of High Resolution Research Tomograph (HRRT). Notice the octagonal detector geometry. 43
2.6 Annihilation coincidence detection. 44
2.7 Illustration of different events associated with annihilation coincidence detection. Only a "true" coincidence event correctly localizes the annihilation. All other events result in erroneous lines of response and must be corrected for prior or during reconstruction of PET data. Note: LOR recorded as line joining two opposing detectors. 46
2.8 Chemical structure of L-[*methyl* -^{11}C]Methionine [1]. 47

3.1 Anterior Inferior Cerebellar Artery (AICA) used for arterial input function determination in DCE-MRI pharmaco-kinetic modeling. 57
3.2 Fitted AIF and measured signal intensity for ROI of AICA for one patient. 57

3.3 Fitted AIFs for all patients with population averaged-AIF for ROI of AICAs. 58

4.1 Post-contrast T_1-weighted image (MPRAGE) for P03. Tumor enclosed in yellow box and blown up for easier viewing, with radiological orientation directions indicated as: R = right, L = left, A = anterior, P = posterior. Small, non-enhancing regions of the tumor were considered to be cystic or necrotic. 62

4.2 A: $IAUC_{60}$ map, B: K_{trans} map, C: v_e map, D: v_p map, and E: mean diffusivity (MD) map for P03 about the tumor region identified in Figure 4.1. This color scale also applies to all (A thru E) parametric maps, although the ranges differ as follows :$(0 \leq K_{trans} \leq 0.5)$ min^{-1}, $0 \leq v_e, v_p \leq 0.5$. All maps are registered to T_1-weighted images and overlaid on corresponding T_1-weighted slice for morphological reference. . 63

4.3 Fractional anisotropy (FA) map for P03 modulated with respect to an eigenvector of the diffusion matrix. A yellow box encloses the location of the tumor. Regions where FA is high (close to one) appear opaque, with red, green, and blue indicating principal diffusion along the anterior-posterior , superior-inferior, and right-left directions, respectively. Mixtures of colors indicate principal diffusion along directions that are linear combinations of the principal diffusion directions described. Regions where FA is low (close to zero) appear more transparent. 65

4.4 MET-PET summed image for P03 overlaid with T_1-weighted image that has been registered to MET-PET space. A color scale for intensity similar to that shown in Figure 4.2 applies to this image with the exception that pixels appearing gray-white (as in the central portion of the tumor and the nose) have the highest activities. 66

4.5 Time activity curves for ROIs chosen within various tissues exhibiting increased activity on MET-PET for P03. Tumor ROIs seem to enhance later than both cerebellum and nasal tissues. 67

4.6 Post-contrast T_1-weighted image for P08. Tumor enclosed in yellow box. Unlike the tumor seen in Figure 4.1, this tumor displays homogeneous enhancement. 68

4.7 A: $IAUC_{60}$ map, B: K_{trans} map, C: v_e map, D: v_p map, and E: mean diffusivity (MD) map for P08 about the tumor region identified in Figure 4.1. This color scale also applies to all (A thru E) parametric maps, although the ranges differ as follows :$(0 \leq K_{trans} \leq 0.5)$ min^{-1}, $0 \leq v_e, v_p \leq 0.5$. All maps are registered to T_1-weighted image and overlaid on corresponding T_1-weighted slice for morphological reference. . 69
4.8 Fractional anisotropy (FA) map for P08 modulated with respect to an eigenvector of the diffusion matrix. A yellow box encloses the location of the tumor. Regions where FA is high (close to one) appear opaque, with red, green, and blue indicating principal diffusion along the anterior-posterior , superior-inferior, and right-left directions, respectively. Mixtures of colors indicate principal diffusion along directions that are linear combinations of the principal diffusion directions described. Regions where FA is low (close to zero) appear more transparent. 70
4.9 MET-PET summed image for P08 overlaid with T_1-weighted image that has been registered to MET-PET space. A color scale for intensity similar to that shown in Figure 4.2 applies to this image with the exception that pixels appearing gray-white (such as the nose) have the highest activities. 71
4.10 Time activity curves for ROIs chosen within various tissues exhibiting increased activity on MET-PET for P08. Tumor ROIs seem to enhance later than both cerebellum and nasal tissues. 72
4.11 Mean concentration-time curves for all tumor ROIs. ROIs excluded non-enhancing tumor regions. 74
4.12 Mean concentration-time curve for P01's tumor ROI including 2- and 3- parameter pharmaco-kinetic model fits. Note that 3- parameter model fits are shown for both individual and population-averaged AIFs. 75
4.13 $IAUC_{60}$ for mean of concentration of tumor ROIs. 75
4.14 Mean K_{trans} for tumor ROIs from 3-parameter fit. P01, P02, P03, and P07 had visibly cystic tumors. 76
4.15 Mean v_e for tumor ROIs from 3-parameter fit. P01, P02, P03, and P07 had visibly cystic tumors. 76
4.16 Mean v_p for tumor ROIs from 3-parameter fit. P01, P02, P03, and P07 had visibly cystic tumors. 77

4.17 Average mean diffusivity (MD) for tumor ROIs that both included and excluded cystic components. 79
4.18 Average mean diffusivity (MD) for tumor ROIs that excluded cysts and contra-lateral cerebellum ROIs. 80
4.19 Average FA for tumor ROIs that both included and excluded cysts. 80
4.20 Average FA for tumor ROIs that excluded cysts and contra-lateral cerebellum ROIs. 81
4.21 Tumor volumes as measured from post-contrast T_1-weighted images and MET-PET. 83
4.22 Stardardized uptake values (SUVs) for all tumors plotted versus time. Tumor ROIs were derived from summed MET-PET images, and SUV represents mean activity of the tumor normalized for injected dose and patient weight. 84
4.23 SUVs for tumor and control ROIs for summed MET-PET. . . 84
4.24 PRESS acquired single-voxel spectrum for P08. Metabolites identified using the LCModel are indicated with red arrows. The table to the right displays the ratios of the relative concentrations of metabolites to creatine (Cr). Only metabolites highlighted in blue have acceptable levels of measurement error. 86
4.25 PRESS acquired single-voxel spectrum for P06. Metabolites identified using the LCModel are indicated with red arrows. The table to the right displays the ratios of the relative concentrations of metabolites to Creatine. Only metabolites highlighted in blue have acceptable levels of measurement error. 87

5.1 Histogram for T_1-weighted signal intensities observed in P03 tumor (including cysts). 90

List of Abbreviations

VS	vestibular schwannoma
MRI	magnetic resonance imaging
DCE-MRI	dynamic contrast-enhanced MRI
DW-MRI	diffusion-weighted MRI
MRS	magnetic resonance spectroscopy
MET	^{11}C-methionine
PET	positron emission tomography
CPA	cerebellopontine angle
SRS	stereotactic radiosurgery
FSRT	fractionated stereotactic radiotherapy
CT	computed tomography
LINAC	linear accelerator
ADC	apparent diffusion coefficient
BBB	blood-brain barrier
CA	contrast agent
EES	extravascular-extracellular space
ROI	region of interest
VOI	volume of interest
DWI	diffusion-weighted image
MD	mean diffusivity
FA	fractional anisotropy
EPI	echo planar imaging
FOV	field of view
FLASH	fast low-angle shot
AICA	anterior inferior cerebellar artery
AIF	arterial input function
PK	pharmaco-kinetic
$IAUC_{60}$	initial area under the curve for first 60 seconds post-contrast
SUV	standardized uptake value

Acknowledgements

Special gratitude is extended to supervisor Stefan Reinsberg, who patiently provided invaluable guidance and voluminous instruction throughout the project. Dr. Montgomery Martin also provided assistance and contributed knowledge throughout the study's duration. Dr. Richard Shaffer helped regularly with patient recruitment, attended PET scans, and contributed advice and knowledge. Dr. Roy Ma was instrumental in conceiving the project and also attended many PET scans. Dr. Michael McKenzie and Dr. Alan Nichol were very helpful in recruiting patients and contributing advice. Dr. Burkhard Mädler and Dr. Alex MacKay assisted greatly in developing the DTI and MRS imaging protocols at the UBC facility. Appreciation is sent to the technologists at the BCCA and UBC 3T MRI Center who performed patient scans. A dedicated team of experts in the field of positron emission tomography facilitated the use of the High Resolution Research Tomograph. In particular, Dr. Vesna Sossi and Katie Dinelle were invaluable resources for this aspect of the study. Tom Ruth also helped in the development of the ethical approval for MET-PET, and chemist Salma Jivan was responsible for the synthesis and delivery of ^{11}C-methionine - an unprecedented tracer at the UBC PET Center. Thanks are extended to technologists Carolyn English and Caroline Williams who performed all preparatory work and patient scanning at the UBC PET Center.

Dedication

I would like to extend appreciation to my family for supporting my academic goals. Cyrus - thank-you for patiently waiting innumerable hours for me to come home and play. Graham - thanks for all of your help and support. Most of all, gratitude is extended to all of the patients who participated in this study.

Chapter 1

Introduction

1.1 Motivation

Vestibular schwannomas (VSs) are benign neoplasms and constitute approximately 6-10% of all brain tumors [31, 55]. Treatment generally includes one or a combination of three approaches: conservative observation, surgical resection, and radiotherapy. Due to their relatively slow growth, follow-up periods for VSs tend to be very long. Most VSs are successfully treated, so protracted follow-up intervals undoubtedly lead to unnecessarily high levels of patient anxiety. Current follow-up involves magnetic resonance imaging (MRI) at least once per year for a minimum 5 year duration to ensure cessation of tumor growth.

Radiotherapy has become very popular in recent years due to its reduced rates of complications in comparison to traditional resection [30]. Many centers have opted for prophylactic intervention with radiation treatment for tumors less than 30 mm in diameter (although some centers employ fractionated radiotherapy for tumors exceeding this size). This pilot study sought to identify early predictor(s) of radiation treatment response using a non-invasive multi-modality imaging approach. No studies existed that attempted to correlate multi-modality imaging data to radiation treatment response of VSs. It was hoped that by combining information acquired from dynamic contrast-enhanced MRI (DCE-MRI), diffusion-weighted MRI (DW-MRI), magnetic resonance spectroscopy (MRS), and ^{11}C methionine positron emission tomography (MET-PET), treatment response could be identified sooner than the current several year waiting period.

Some changes previously observed in radiation treated VSs include: vascular shut-down and modification, necrosis, cyst formation, enlargement or shrinkage, cellular proliferation, changes in microvessel density, and altered metabolite concentrations [3, 15, 31, 43, 68]. The functional MRI and MET-PET techniques employed in this study are capable of imaging many of these changes. In addition, most VS patients are in good general health during the course of their treatment and subsequent period of observation, so subjecting them to several imaging sessions is usually not problematic.

1.2 Objectives

By examining a small population of 10 VS patients, this pilot study primarily aimed to identify imaging techniques that were sensitive to pathological changes in VS tissue following treatment by radiation. Comparison of pre-treatment to post-treatment data helped identify correlations between treatment success or failure and pathological response as identified by several imaging techniques. The selection of a broad range of imaging modalities enhanced sensitivity to detection of treatment response.

The primary objective of this study seeded many secondary goals such as seeking the creation of a multifaceted MRI protocol that included the use of DW-MRI, DCE-MRI, and MRS for application to an eventual larger patient population. Furthermore, the use of ^{11}C-methionine PET (MET-PET) imaging of radiation-treated VSs led to a similar attempt to create a useful MET-PET protocol for VSs intended for use on a larger patient group in the future. Development of effective analysis software was sought to enable quantitative analysis of functional imaging data. In addition, an aim of the study was to design a larger trial for definitively testing the utility of functional imaging protocols and analysis programs for earlier detection of VS response to radiation treatment. Therefore, pilot data were acquired with the objective of determining an ideal imaging follow-up frequency and duration.

Chapter 2

Background

2.1 Vestibular Schwannoma

2.1.1 History

Since Rudolf Karl Virchow first described neuroglia, the cells comprising the connective tissue of the nervous system in 1846, vestibular schwannoma tumors have had many names. Due to various proposed cells and locations of origin, pseudonyms have included acoustic neurinoma, acoustic neurilemmoma, acoustic neuroma, and the most accurate description - vestibular schwannoma. With later advances in microscopy, the Schwann cell was correctly identified as the cell of tumor origin, and the vestibular portion of the 8^{th} (vestibulocochlear) cranial nerve was established as its predominant location of occurrence. Currently popular names in the literature are vestibular schwannoma and acoustic neuroma. Due to its common association with hearing reduction and loss, acoustic neuroma remains in popular use despite its histological inaccuracy. As vestibular schwannoma (VS) most aptly describes the origin of the tumor, it is the name henceforth applied [31, 55].

Successful removal of the first cerebellopontine angle (CPA) tumor is credited to Sir Charles Ballance in 1894, although the patient suffered from significant complications involving damage to the trigeminal and facial nerves. Complete preservation of these nerves, in addition to attempts to preserve hearing in the affected ear, has remained a challenge for surgeons due to the tumor's sensitive location. Despite many advances in conventional resection techniques, total nerve preservation has remained elusive and many centers have sought alternative measures for controlling VSs [31].

Radiation therapy has become a popular alternative for tumor control. Stereotactic radiosurgery (SRS) of a VS was first described by the inventor of the Leksell Gamma Knife radiosurgery (GK-SRS) unit, Lars Leksell, in 1971 [7]. Since the advent of SRS, doses have been gradually reduced in conjunction with improved dose conformity and increased awareness of the radiobiological effects of ionizing radiation. According to Kanzaki et al. [29],

Fractionated stereotactic radiotherapy (FSRT) is typically administered to VSs in 20-25 fractions over a 5-6 week period to give a total dose of 40-50 Gy. Many authors report radiotherapy control rates of moderately sized ($< 30\ mm$) VSs as greater than or equal to those achieved with traditional resection. In addition, radiotherapy reportedly yields better rates of hearing and trigeminal/facial nerve preservation when compared to traditional resection [3, 8, 16, 18, 21, 29, 30, 36, 37, 38, 52, 56, 58, 61].

2.1.2 Epidemiology

VSs are thought to comprise approximately 6-10% of all intra-cranial brain tumors (BTs) and represent approximately 78% of all CPA lesions. Recent series have indicated higher incidence rates presumably due to improved awareness of the presenting symptoms and diagnostic techniques. About 95% of all VSs are sporadic (unilateral). Bilateral VSs are associated with a hereditary disorder known as neurofibromatosis type 2 (NF2) and are regarded as pathologically distinct from the sporadic form. VSs most commonly arise in the fourth and fifth decades of life, and there is a slight female predilection. Additionally, observations of an inverse relationship between tumor growth/size and patient age were documented [31, 55].

2.1.3 Anatomical and Pathological Description

Under the World Health Organization's (WHO) Classification of Central Nervous System Tumors, sporadic VSs fall within Class 2, Tumors of the Cranial and Spinal Nerves, and section A, Schwannoma. Schwannomas are typically solitary masses involving the cranial and/or spinal nerve roots (rather than the peripheral nerves). The most common intra-cranial form of schwannoma involves the 8^{th} cranial (vestibulocochlear) nerve, although other forms can originate from the 7^{th} (facial), 5^{th} (trigeminal), 10^{th} (vagus), and other cranial nerves. As 8^{th} cranial nerve schwannomas arise most frequently (and about equally) from both the inferior and superior vestibular portions of the nerve, they are called vestibular schwannomas [31, 55].

Growth of Schwann cells is controlled by the NF-2 gene, located on the long arm of chromosome 22. A defect in this suppressor gene is theorized to cause both the sporadic and bilateral forms of VS. Known to be very genetically active, spontaneous mutations of the relatively small chromosome 22 are thought to be common. The defect is congenital in the bilateral form and is present in the germ cell line, while the sporadic form is postulated to arise from a homozygous mutation of the NF-2 genes later in life. In the

bilateral form, only one normal copy of the NF-2 gene is inherited (from the unaffected germ cell), and a somatic cell later suffers spontaneous mutation of the other NF-2 gene. Depending on which precursor cell line acquires the mutation, many cell lines, not just Schwann cells, can be affected. Patients with all cells affected form a subset of neurofibromatosis type 2 (NF2) and are prone to developing multiple meningiomas in addition to bilateral VSs. To develop sporadic VSs, both NF-2 genes must mutate in a specific Schwann cell precursor and sufferers are not predisposed to developing other neoplasms [31].

VSs tend to originate from the location where the glial (central) nerve sheaths are replaced by Schwann (peripheral) cells and fibroblasts. This junction, that essentially marks the boundary between the central and peripheral nervous system, is known as the Obersteiner-Redlich zone and often occurs near the ganglion of Scarpa, although its location can vary. Scarpa's ganglion consists of the cell bodies of the vestibular portion of the 8^{th} cranial nerve and is located in the outer part of the internal auditory (or acoustic) meatus (or canal). The vestibular nerve separates into inferior and superior groups of neurons that connect to various structures of the inner ear. Probably as a result of an excess of embryonic precursors to Schwann cells, most VSs arise from the vestibular portion of the 8^{th} cranial nerve. Incidences of VSs arising from the inferior and superior segments are approximately equal with about 50-60% occurring superiorly and 40-50% occurring inferiorly. An estimated 10% of "vestibular" schwannomas arise from the cochlear portion of the 8^{th} cranial nerve [31].

The nerve of origin, the 8^{th} cranial nerve, synapses with the medulla oblongata from the middle and inner ear via the internal auditory meatus (IAM). Early on, VSs are confined to the IAM, but left untreated many will grow and may compress neighboring nerves such as the cochlear component of the 8^{th}, and the 5^{th}, 6^{th}, and 7^{th} cranial nerves. The tumor tends to create problems by compressing nearby structures, rather than by infiltrating healthy parenchyma as many malignant neoplasms do. Due to their proximity to bone and air cavities, MRS of VSs poses particular challenges. Achieving a satisfactory level of magnetic field homogeneity by shimming is especially difficult. MRS of VSs is discussed in detail in Section 2.3.5 [31, 55].

VSs are usually well circumscribed, irregularly shaped, encapsulated lesions that largely displace their parent nerve. They tend to be mostly solid, although some are polylobulated with cystic lobules. Acystic tumors are usually hard and elastic in consistency, but there is reduced consistency in tumors with marked regressive phenomena such as hemorrhagic degenera-

tion that is observable in larger tumors. Histologically, VSs can be composed of Antoni A or Antoni B type cells, or a mixture of both. Larger VSs tend to have a looser textured/cystic extracellular matrix which is associated with Antoni B type cellularity. Smaller VSs are usually composed primarily of Antoni A type pathology, which is marked by a more compact cellular structure compared to the Antoni B type [31, 47].

Hyalin, a clear substance, is often produced as the epithelial tissue of the blood vessels degenerates. This hyalinization of the blood vessels is a prominent feature of schannomas and may appear with sinusoidal dilation assuming large proportions. Spontaneous hemorrhage followed by necrosis of such regions is not uncommon. Macrophages may infiltrate the hemorrhaged region to engulf and digest the hemoglobin that is released by dead red blood cells, resulting in hemosiderin deposits. Other degenerative events include enlargement, hyperchromasia of cell nuclei (where cells may stain abnormally intensely due to nuclei degeneration), and hypercellularity (atypical increase in cell concentration) [31].

Since necrotic and cystic regions represent primarily inactive tumor tissue, it was hoped that functional imaging techniques would enable their distinction. For instance, diffusion coefficients (of water) within degenerative areas, as identified with DW-MRI, should be higher than in solid tumor sections due to fewer numbers of diffusion-inhibiting tumor cells and microvessels. MRS can potentially reveal variations in metabolite concentrations between tumors with constitutional and physiological differences. Moreover, differences in contrast are predicted to manifest in DCE-MRI. Pharmacokinetic parameters, derived from the analysis of such data, can identify changes in tumor vasculature and blood flow into and out of the tumor. Finally, MET-PET was hoped to aid in identifying metabolically active tumor regions as compared to necrotic or other degenerative tissue areas [31].

Growth patterns are generally slow but can be quite variable as reflected in differences in symptom duration at the time of diagnosis. Larger tumors do not necessary grow faster than smaller tumors, and various elements are thought to contribute to growth rates. Likhterov et al. [36] report indications of non-linear growth and emphasize the need for long-term follow-up of VSs as periods of stability may not be prognostic of long-term control. Likewise, a proliferative period may not be predictive of continuous enlargement in the future. Events such as hemorrhage, cystic degeneration, and peritumoral edema can all cause abrupt tumor enlargement. Most VSs grow medially from their IAM origin along the easiest path to the CPA. Lateral growth is generally restricted by the fundus of the IAM, although some tu-

mors have been found past the fundus (within the labyrinth). Faster growth often ensues once the tumor invades the CPA, as it is no longer bounded by the IAM, and can lead to brain stem and cerebellar compression. Large VSs can burrow into the medulla oblongata and pons and can extend inferiorly to the foramen magnum and superiorly to the cerebellar tentorium. However, by employing several imaging modalities, it was hoped that parameters indicative of long-term treatment success or failure would be identified much sooner than the current follow-up period of several years. As treatment success rates exceed 90%, successfully treated patient populations should, in theory, share some common features [29, 31, 55].

2.1.4 Clinical Features and Diagnosis

Patients almost invariably present with some degree of sensorineural hearing loss. Unfortunately, many patients dismiss their hearing deterioration for long periods by erroneously attributing it to old age or physical trauma. Hearing loss is typically asymmetric and progressive for unilateral VSs, but approximately 10% of patients report sudden hearing loss. Compromise of inner ear vasculature could cause this sudden hearing loss. The most common pattern for hearing deterioration is high frequency hearing loss, together with reduced speech discrimination. Other early symptoms include tinnitus, disequilibrium with vertigo, and headache. Patients at later stages with larger tumors may suffer from facial weakness and/or numbness due to compression of the facial and trigeminal nerve. Other late symptoms include ataxia (loss of control of body movements), diplopia (double vision), dysphagia (difficulty swallowing), hemiparesis (paralysis of one side of the body), increased intra-cranial pressure, and cerebellar hemisphere syndrome. Cerebellar hemisphere syndrome encompasses neuro-ophthalmic signs such as nystagmus (rapid, involuntary eye movement) and depression of the ipsilateral corneal reflex, among other indications. Prior to the advent of MRI and CT technologies, evidence of this syndrome was valuable in determining whether a VS had grown beyond the confines of the IAM. Rarely, patients with larger tumors exhibit rapid neurological deterioration, most often as a result of a massive hemorrhage within the tumor or rapid cyst expansion [31, 55].

Despite high rates of hearing abnormalities in VS patients, only about 10% of patients experiencing classical symptoms of a VS will actually have a VS upon radiological examination. Generally, patients presenting with variable forms of hearing loss and/or balance problems will be screened for VS. Prior to screening with expensive imaging techniques such as MRI or

CT, hearing screening tests can be used to help rule out VS. For example, brain stem auditory evoked potentials are abnormal in 92-96% of patients with a VS. This technique provides a useful and cost-effective screening method for patients, such as children and adolescents, with a low probability of having a VS. Historically, computed tomography (CT) was the first imaging choice for identification of VSs as it was cheaper and more widely available than MRI. However, tumors next to bone (such as IAM-confined VSs) and smaller tumors ($<5\ mm$) are difficult to see with CT, and MRI has replaced CT as the main imaging modality. Typical diagnosis is made using a gadolinium-based contrast agent in contrast-enhanced T1-weighted MRI (CE-MRI). T2-weighted MRI is generally not used as the lesion may appear isointense with cerebral spinal fluid. After contrast administration, the tumor becomes bright and is often identifiable even when still confined to the IAM. That being said, CE-MRI mainly delineates regions of the tumor where breakdown of the blood-brain barrier has occurred. By using additional functional imaging techniques, this study aimed to identify additional tumor tissue not presenting with blood-brain barrier destruction. Meningioma, another CPA tumor, can mimic VS both clinically and radiologically, but careful examination of subtleties in radiologic findings can minimize wrongful diagnoses [4, 31, 55].

2.2 Radiotherapy

2.2.1 Stereotactic Radiosurgery and Fractionated Stereotactic Radiotherapy

There are two main ways to deliver radiation to diseased tissues: stereotactic radiosurgery (SRS) and fractionated stereotactic radiotherapy (FSRT). SRS involves the precise delivery of a known amount of ionizing radiation to a localized 3D target in a single delivery. FSRT differs from SRS in that lower doses are prescribed and delivered in multiple treatment sessions, or fractions, over a period ranging from days to several weeks. Maximizing exposure to diseased tissue and minimizing exposure to healthy surrounding tissue is paramount to successful treatment with SRS. Precise dose delivery relies upon sophisticated computer treatment planning techniques that use registered CT and MRI images for anatomical input. Treatment plans for both FSRT and SRS are tailored to each patient's unique anatomy so as to maximize dose to diseased matter and minimize dose to healthy and radiation-sensitive surrounding structures. Due to the lower doses involved in FSRT, dose delivery is not required to be as precise (although it often is)

as the damage to healthy surrounding tissues is limited by the reduced doses used. Therefore, non-invasive thermoplastic masks are typically used to minimize patient motion during FSRT. As they are not physically anchored to the skull, thermoplastic masks are easily removable and replaceable with each treatment fraction. These masks differ from the invasive head frames used to drastically reduce patient motion during SRS, where accuracy in dose delivery is much more crucial due to the higher doses involved. A typical head frame is secured to the periosteum of the skull with small pins. In addition, doses in FSRT are prescribed so as to produce therapeutic effects while concurrently limiting dose to sensitive structures (such as nerves) that lie within the main treatment field. Furthermore, between treatment fractions healthy tissues are given an adequate time to recover from any radiation damage that is sustained during treatment. Section 2.2.2 describes the principles behind fractionating treatment in more detail.

As already discussed, SRS may be administered with a ^{60}Co Gamma Knife or linear accelerator (LINAC) device. FSRT is usually delivered with a LINAC. Although most literature pertaining to SRS of VSs is based on GK delivery of radiation, Friedman et al. [21], Meijer et al. [40], Radu et al. [50], Okunaga et al. [46], Spiegelmann et al. [58], and Rutten et al. [52] report successful LINAC SRS of VSs. Additionally, in their comparison of LINAC and GK deliveries of SRS, Perks et al. [48] indicate the superiority of the GK in the 1990's, with respect to dosimetry, has dwindled due to the integration of micro multi-leaf collimator (mMLC) technology into LINAC machines.

2.2.2 Radiation Biology

Treatment with ionizing radiation causes various levels of damage and is intended to arrest or control the cellular proliferation associated with tumors. The excitation of electrons in molecules, caused by exposure to ionizing radiation, yields highly reactive free radicals (molecules with unpaired electrons) that degrade the structures necessary for cell survival. Radiation damage to the cell's phospholipid bilayer membrane can activate pathways leading to apoptosis (programmed cell death). The most important structural damage, however, is wrought on deoxyribonucleic acid (DNA), the largest molecule in the cell. Due to its fragile double stranded helix structure and vulnerable biochemical composition, DNA is highly susceptible to damage from photons (radiation) and free radicals. Single strand breaks and even multiple breaks on the same strand of a DNA molecule are often repaired by endogenous surveillance DNA endonucleases. As only one strand is damaged, the

intact complementary strand can serve as a repair template or temporary "splint" for a broken DNA molecule. The most devastating effects of radiation are double strand breaks. As there is no unbroken strand to act as a template, endogenous repair enzymes cease to function. Generally, there are four possible outcomes following a double strand break:

1. Spontaneous reannealing in correct orientation by means of a collision - this is extremely unlikely;

2. DNA damage activates endogenous cellular genomic surveillance system. This would trigger apoptosis. Early tumor shrinkage would be the clinical observation due to cell loss;

3. DNA damage only triggers activation of endogenous cellular genomic surveillance system after the cell enters the active cell cycle. In this case, observation of shrinkage would be latent due to delayed apoptosis (need to wait until tumor enters active growing phase);

4. DNA damage causes irreversible cellular growth arrest. Cells remain intact, but don't enter the active cell cycle. In theory, this scenario occurs as a result of direct damage to genes controlling and affecting cell cycle progression or control. Clinically, permanant stability in size would be observed (lack of growth).

The proliferative index of VSs is relatively low at 1-5%, indicating generally long cell cycle times, so one would expect tumor shrinkage to continue many years post-radiation-treatment. In fact, this phenomenon has been documented extensively in clinical GK-SRS of VSs. This is consistent with scenario 3 described previously. In addition, scenario 4 is well described for SRS-treated VSs. It was hoped that degenerative effects associated successful radiotherapy could be discerned with one or more functional imaging techniques. For example, DW-MRI could disclose reductions in cell and microvessel density by displaying higher apparent diffusion coefficients (ADCs). Since fewer structures would exist to restrict water movement, higher ADCs would be observed [36, 37].

Radiation-induced inhibition of tumor cell proliferation also occurs via progressive radio-obliteration of the tumor's vascular supply. Removal of the neoplastic vasculature might serve to explain many observations of late-manifesting VS shrinkage post-radiotherapy [29]. Vascular damage from radiation leads to hyalinization of arteriole walls and myointimal cell proliferation. Together these responses cause small artery and arteriolar occlusions that can lead to tumor cell ischemia and hypoxic cell death. It

is thought that SRS is superior to FSRT in producing vascular occlusion, although FSRT can still cause some secondary vascular effects [37]. Some observations of these effects would include a loss of central enhancement on Gd CE-MRI due to vascular obstruction, followed by delayed tumor shrinkage once ischemic cell loss predominated over ischemic cell swelling. Interestingly, this is a well documented phenomenon in radiation-treated VSs. Wide-scale cell death could also present as a reduction in uptake or contrast on MET-PET. Further, DCE-MRI could highlight reductions in metabolic requirements by showing decreases in local blood flow to the tumor. Finally, metabolite concentrations observed via MRS would manifest differently in pathologically altered tissues [37].

To increase radiation damage to DNA, one can maximize the interaction probability of radiation with DNA by delivering doses when cells are in metaphase: the stage in the cell cycle when DNA is in its most condensed form, or by simply increasing the dose. For tumors with high proliferative indices, fractionating the dose may be beneficial as it increases the probability that cells will be targeted during metaphase. Fractionating doses can also be beneficial in situations requiring reduced exposure to radio-sensitive structures. Traditional radiation therapy is based on fractionating treatments. The main ideas behind fractioning doses are summarized as the 4 "R's" of FSRT:

1. Reoxygenation: hypoxic cells are less likely to enter the cell cycle (metaphase in particular), so waiting between fractions can help tumor cells return to normal pO_2 levels;

2. Redistribution: delivery of multiple fractions increases the chances of treating cells while they are in metaphase;

3. Repopulation: this is only beneficial if healthy cells repopulate faster than neoplastic cells between fractions. This is related to the therapeutic index, defined as the ratio of the magnitude of therapeutic effect to the toxicity associated with the treatment. In other words, the therapeutic index increases if toxicity to normal tissue is minimized and toxicity to neoplastic cells is maximized (or maintained) with fractionation.

4. Repair: this is beneficial if endogenous cellular repair mechanisms are impaired for tumor cells.

The first two tenets of fractionating treatment are not significant for SRS. As higher doses are delivered in a single fraction, permanent DNA

damage is fairly likely even when cells are in their diffuse chromatin form (not in metaphase). Since VSs have low proliferative indices of 2.5-4, they are unlikely to be in metaphase and would not theoretically benefit from some aspects of fractionation. In addition, the last two R's are minimally relevant to SRS as this modality couples accurate delivery of dose with steep marginal dose gradients to limit damage to healthy surrounding parenchyma. After reviewing the 4 "R's" of fractionating treatment, it would seem that VS patients may not be ideal candidates for FSRT (barring contraindications to SRS such as a tumor diameter exceeding 30 mm). However, various camps (including the center where this study was based from) advocate in favor of FSRT over SRS in certain situations. In particular, some centers support using FSRT when patients still possess serviceable hearing. Due to the sensitivity of the 8^{th} cranial nerve and its inherent entanglement with the treatment target, FSRT may provide some nerve sparing effects. Damage incurred by the vestibulocochlear nerve during treatment fractions may be spared via the third tenet of the fractionating treatment principle. Unfortunately, no compelling long-term evidence exists that clearly demonstrates the superiority of one form of radiotherapy delivery over another [37].

Some authors argue in favor of fractionating treatment of VSs due to increased rates of hearing preservation and minimization of various neuropathies [18, 36, 56, 61]. Spiegelmann et al [58] advocate for fractionation when tumors compress the brain stem, or when tumor diameters exceed 30 mm - making microsurgical intervention very difficult. Limiting the SRS-delivered dose to sensitive brain structures, such as the brain stem, becomes exceedingly difficult once tumors reach larger proportions. FSRT offers therapeutic benefits while limiting exposure to critical nerves within the radiation-treatment field. In cases where VSs are very large ($\geq$ 30 mm), unavoidable exposure of the brain stem to radiation can be minimized with fractionation. Others contest that morbidities associated with SRS are comparable to FSRT results and argue SRS provides better long term tumor control, possibly due to the higher doses employed. To reiterate, there is no consensus on which form of radiotherapy is best for VSs [3, 16, 21, 37, 38, 40, 43, 46, 48, 50, 52, 58, 68].

2.2.3 Radiotherapy of Vestibular Schwannomas

Unlike the goal of complete removal of the tumor in microsurgery, radiotherapy aims to arrest tumor growth by affecting cell viability. Treatment success, or tumor control, is usually defined as an absence of tumor growth and/or shrinkage. Many centers define tumor control as freedom from sur-

gical resection. Successful removal of VSs using microsurgical techniques depends on an array of factors such as the surgeon's experience, the surgical approach used (there are 6), the tumor's size and relative location, and the patient's state of health. Microsurgery is often contraindicated for elderly patients and patients with comorbidities placing them at unacceptably high levels of risk during the surgical procedure. Due to the invasive nature of microsurgery, many complications are known to result such as facial and trigeminal neuropathy, hearing reduction or loss, and hydrocephalus, among others. Lunsford et al. [38] reported a $\frac{1}{200}$ mortality rate during the first month post-microsurgery. For these reasons, many centers promote SRS or FSRT for treatment of VSs less than 30 mm in maximal diameter and for patients with contraindications to microsurgery.

Some retrospective studies of SRS treated VSs indicate reduced morbidities in conjunction with comparable tumor control rates when compared to microsurgery. Also, SRS offers convenience to patients as it is minimally invasive and requires only a single visit to the hospital. Most patients are discharged on the same day and express only mild discomfort when skull-anchored head frames are used. FSRT is less convenient from the patient's perspective, as it requires multiple treatment sessions over a period of several weeks. Despite its seeming inconvenience, FSRT may provide a higher probability of hearing preservation - making patients more likely to tolerate the added burden of several treatment sessions. However, it is important to recognize subtleties involved with interpreting retrospective studies of radiation-treated VSs. Results are highly dependent on delivered dose, fractionation scheme (if applicable), mode of dose delivery, dose conformity and homogeneity, duration of follow-up period, and conventions used to measure the tumors. Due to their slow growth, reliable measurement methods are tantamount for meaningful assessments of treatment outcome [29, 53]. Nevertheless, taking into account such variability, many studies examining radiotherapy with similar dosing tout essentially equivalent rates of tumor growth control and treatment related morbidities despite using different types of GK and LINAC units [3, 16, 18, 21, 29, 36, 37, 38, 40, 43, 46, 48, 50, 52, 56, 58, 61, 68].

In the pioneering years, SRS-treated patients received up to 45 Gy at the tumor margin. However, patients suffered from unacceptably high rates of treatment-related morbidities including cranial neuropathy, hearing loss, and hydrocephalus. Over the years, as treatment planning and conformality improved, marginal doses were reduced to 16-20 Gy, and then to 12-13 Gy between 1992-1994, resulting in lower morbidity rates and similar levels of tumor control [7, 16, 21].

Andrews et al. [3] reported excellent outcomes from both SRS and FSRT of VSs. Low morbidities and comparable rates of trigeminal and facial nerve preservation were observed. FSRT was associated with a 2.5-fold higher rate of hearing preservation in patients with serviceable hearing prior to treatment. FSRT was administered in daily 2 Gy fractions over the span of 5 weeks, giving a cumulative dose of 50 Gy. GK-SRS was given in a single 12 Gy dose prescribed to the 50 % isodose line.

Selch et al. [56] reported a 92.4% 5 year actuarial rate of tumor control with FSRT given in 30 fractions of 1.8 Gy prescribed to the 90% isodose line. Transient tumor enlargement was observed in 25% of patients at 6 months post-treatment. Size reduction usually occurred within 12 months post-treatment. In addition, there was loss in central tumor enhancement 67% of the time using CE-MRI at approximately 6 months post-FSRT.

Hearing preservation following FSRT of 34 VS patients was examined at the British Columbia Cancer Agency, Vancouver Center, by Thomas et al. [61]. Patients with serviceable hearing - defined as having Gardner-Robertson Class 1 or 2 hearing - received LINAC FSRT, while functionally deaf patients were given LINAC SRS. Furthermore, patients with serviceable hearing were required to have a speech reception threshold that was less than 50 dB and speech discrimination exceeding 50%. For FSRT, which was the focus of this exposition, a total of 50 Gy was administered in 25 fractions spread over 5 weeks. Overall, 97% of FSRT patients remained resection-free, and there were no incidences of long-term trigeminal neuropathy. The facial nerve complication rate was 6%. Moreover, the 2, 3 and 5-year actuarial hearing preservation rates were 63%, 63%, and 56%, respectively. However, the actuarial preservation rate of pre-FSRT Gardner-Robertson hearing grade was 53.8%, 45.5%, and 28.9% at 2, 3, and 5 years post-treatment, respectively. An important finding was that the dose to the cochlea was the only prognostic factor for hearing preservation post-FRST.

In an examination of LINAC SRS-treated VS patients, Friedman et al. [21] stated the VS's anatomy make it an ideal candidate for SRS as it has a well-demarcated border and is non-invasive to neighboring tissues. This allows treatment planners to conform sharp dose gradients at the tumor's border, thus sparing healthy tissues. They also noted that the probabilities of neuropathies are proportionate to the tumor volume and dose delivered. Median marginal doses were 12.5 Gy and lesions were treated to the 70-80% isodose line. The number of isocenters varied from 1 to 14 depending on the shape of the tumor.

Chopra et al. [16] reviewed 216 treatment naive, unilateral VS patients treated with GK-SRS between 1992-2000. Patients received 12-13

Gy marginal dose and were followed-up with MRI scans for a median of 68 months. They reported a 98.3% actuarial tumor control rate with failure defined as a 1 *mm* size increase in diameter in 2 dimensions, or a 2 *mm* increase in diameter in 1 dimension. No patients experienced facial neuropathy and 94.9% of patients were free of trigeminal neuropathy at 10 years follow-up. Hearing levels, however, continued to decline up to 5 years after treatment. Late hearing loss differed from facial and trigeminal neuropathy which tended to manifest within 3 years of treatment. The authors suggested reasons for latent hearing loss may have included indirect radiation effects like vascular effects and metamorphosis of the tumor remnant.

Beegle et al. [8] examined the effects of treatment planning quality on outcome of SRS of VSs. In particular, conformity of the isodose to tumor shape and magnitude of the dose gradient were studied. A total of 294 patients were treated at the marginal isodose line of 12.5 Gy. Mean follow-up duration was 40 months and there was an actuarial local tumor control (defined as zero growth) rate of 91%. There were no correlations found between conformity and gradient indices and tumor control. Of the patients treated with a mean marginal dose of 12 Gy, only 1% had facial weakness and 0.7% experienced facial numbness. The authors concluded that treatment dose showed the greatest correlation to the incidence of cranial neuropathy, especially in tumors exceeding 4 cm^3. Each 250 cGy dose increase above 12.5 Gy increased the risk of cranial neuropathy by 600%.

Linskey et al. [37] vehemently argued against the use of FSRT for reasons mainly discussed in section 2.2.2. The authors maintained that SRS was the treatment strategy with the best chance of accomplishing permanent control of late-responding tumors like VSs. Marginal doses of 12-13 Gy and 14-16 Gy were recommended for patients with hearing and without hearing, respectively. Complications should be limited via precise 3D alignment of treatment volume to tumor volume by enlisting complex multi-isocenter planning. FSRT should be used for tumors larger than 35 *mm* in order to limit damage to sensitive surrounding structures. Originally, SRS was designed to yield doses causing liquefaction necrosis within the tumor volume. As discussed earlier, such high doses led to unacceptably high complication rates. Later it was learned that necrosis-producing dose levels were not required to inactivate neoplasms biologically or achieve permanent growth cessation of benign tumors. The author emphasized the goal of achieving permanent tumor control and advised against excessive attempts to reduce potential complications that may increase the chances of tumor recurrence.

Between 1987 and 2002, 829 VS patients underwent GK-SRS in a retrospective review by Lunsford et al. [38]. Patients treated after 1992 received

lower marginal doses of 12.5-13 Gy compared to patients treated in earlier years. Of 252 patients followed for longer than 10 years, 98% remained free of surgical intervention. Of 157 patients followed for 10-15 years, 73% experienced reduction in tumor volume, 25.5% had no volume change, and 0.8% required intervention for management of hydrocephalus. No patient developed radiation-induced malignant or benign tumors (defined as a distinct neoplasm arising from within the initial radiation field greater than 2 years post-SRS). Also, early hearing loss was noted as rare and tended to occur between 6 and 24 months post-treatment. Incidences of trigeminal and facial neuropathies in patients treated with 13 Gy marginal doses were 3.1% and <1%, respectively. Between 1991-2001, 313 unilateral VS patients received marginal doses between 12-13 Gy, and the 6 year actuarial resection-free tumor control rate was 98.6%. Perhaps the most important finding, **no differences in tumor control rates were noted for patients in the 12-13 Gy group and those treated with higher prescribed doses in earlier years**.

In accordance with the hypothesis of Linskey et al. [37], Meijer et al. [40] concluded that LINAC SRS yielded tumor control rates superior to FSRT (100% and 94%, respectively, for 5 year actuarial tumor control). Like Linskey et al., the authors suggested that VS's were late-responding tissues with low proferative indices. Therefore, since surrounding brain and nerve tissues are also late-responding, the therapeutic index should not increase with fractionation. SRS-treated patients received between 10 and 12.5 Gy depending on the year of treatment, and FSRT treatment was 5 fractions of 400 cGy or 500 cGy depending on the year of administration. In addition, the authors suggested that the higher rates of hearing preservation seen in FSRT, when compared to SRS as reported by Andrews et al. [3], could be attributed to higher dose inhomogeneity within the GK-SRS group rather than to fractionation, since GK-SRS gives higher maximal dose to the cochlear nerve.

A small study by Radu et al. evaluated LINAC (with mMLCs) SRS of VSs in 22 patients [50]. A marginal dose of 12 Gy was prescribed and patients were followed for a median 18 month period. There was a 100% tumor growth control rate and a 71% preservation rate of serviceable hearing. Two patients experienced transient trigeminal neuropathy and 1 patient had slight facial weakness.

Okunaga et al. [46] extensively reviewed LINAC SRS of VSs. They suggested that transient tumor growth and loss of central enhancement on Gd CE-MRI were typical tumor responses to SRS. A total of 46 unilateral VS patients received median marginal doses of 14 Gy and median maximum

doses of 23.2 Gy. Dose to the brain stem was limited to 10 Gy. Tumor changes were considered significant when volumes changes exceeded 20%. Of the 42 patients followed for longer than 1 year, 45.2% exhibited transient enlargement (that peaked at a median of 4 months) post-SRS followed by shrinkage, 4.8% had no change, and 31% showed direct shrinkage. There was loss in central enhancement on Gd CE-MRI in 88.1% of these cases. Of 42 patients followed for more than 1 year, 73.8% decreased in size, while 81.6% of 38 patients followed for more than 2 years showed volume reduction. Of 18 patients followed for longer than 5 years, all experienced tumor shrinkage. Of particular interest, 11 patients failed to demonstrate shrinkage until 7 years post-SRS. This is perhaps reflective of the variable growth rates of VSs and supports theories in favor of SRS over FSRT due to the late-responding nature of the tumor tissue. Overall, 91.9% of patients experienced no changes in hearing, while 8.1% suffered hearing loss. The rate of trigeminal neuropathy was 2.4%, and facial neuropathy occurred 4.8% of the time.

LINAC SRS of 26 VS patients was reviewed by Rutten et al. [52]. Using a 6 MV Orion LINAC, a mean marginal dose of 12.1 Gy was delivered to the 80% isodose at the tumor periphery. Four or five arcs were used with 1 isocenter; no mMLCs were used. Maximum dose to the brain stem was limited to 10 Gy. Although a transient size increase was observed in many cases, most tumors regressed to pre-SRS volume or smaller within 12-20 months post-SRS. There was a 94.7% probability of tumor control at 5 years. There were no incidences of facial neuropathy and transient trigeminal neuropathy was observed in 8% of patients, possibly due to reversible edema. The authors stated that the maximum dose to the brain stem was the most important predictor of facial/trigeminal neuropathy and toxicity in this study.

Yang et al.[68] examined results of GK-SRS for 61 patients with histopathologically confirmed VSs (all had been previously partially resected). Despite the relatively low marginal doses of 12-13 Gy that were prescribed, many larger tumors showed severe swelling post-treatment. There was occasional failure of GK-SRS for cystic tumors due to cystic expansion. Since 2000, their center has treated patients with GK-SRS 4-6 months after microsurgery to enable maximal differentiation of post-operative changes and residual tumor.

Patients were followed-up regularly post-SRS using MRI. Four and eight year actuarial tumor control rates were 96.5% and 93.5%, respectively, where tumor control was considered to be less than 1 mm growth in any 2 dimensions, or less than 2 mm growth in 1 dimension only. Temporary tumor

swelling was noted in many cases within 3-10 months post-treatment, but resolved spontaneously without intervention. Histologically, there was no difference in relative abundances of Antoni Type A and B cells in cystic and solid tumors. However, cystic VSs were found to have greater amounts of thrombotic vessels and abnormal vessel proliferation. Both of these findings were thought to contribute to higher rates of intratumoral hemorrhage associated with cystic VSs. After draining cystic VSs prior to SRS treatment, control rates were actually found to be higher than for solid tumors. The authors hypothesized that capillary endothelium damage caused interruptions in blood flow and subsequent ischemic tumor cell death (see 2.2.2). In addition, the abnormal vessels in neoplasms tend to be more radiosensitive than normal blood vessels. As cystic VSs were found to have more abnormal vasculature in comparison to solid tumors, this could help explain their enhanced response to SRS. Complementing vascular effects, DNA damage would also be higher in cystic tumors as their cell density is lower than that of solid VSs.

In a study by Spiegelmann et al. [58] of 48 VS patients treated with LINAC SRS, the mean marginal dose was 1455 cGy. Loss of central enhancement on Gd CE-MRI was observed in many cases between 3 and 6 months post SRS. This change was usually transient and was not correlated with poor prognosis. Early enlargement accompanied by loss of contrast enhancement was observed in 11 patients during the first year post-SRS. However, all of these tumors eventually had volume reductions (relative to the pre-SRS volume) within the follow-up period. 75% of tumors had volume reductions later than 12 months post-treatment, and the peak incidence of shrinkage was between 2 and 3 years.

A 98% tumor control rate was achieved with a 71% rate of hearing preservation. Trigeminal neuropathy occurred in 18% of cases and was always associated with facial neuropathy. Although facial neuropathy occurred 24% of the time, all cases improved or resolved over time. It was found that dose and tumor volume were closely related to incidence of neuropathy. During the relatively short follow-up period, lowered doses did not seem to affect tumor control rates. Finally, the authors advocated for FSRT when tumors are compressing the brain stem or have intracisternal diameters exceeding 30 mm and microsurgery is contraindicated. Observation was suggested as the course of action for elderly patients with intracanalicular tumors, especially when serviceable hearing still exists.

2.3 Magnetic Resonance Imaging

2.3.1 Magnetization and Signal Generation

Magnetic resonance imaging (MRI) is based on the phenomenon of nuclear magnetic resonance. Nuclei used for imaging in MRI possess an intrinsic angular momentum called *spin*. The magnitude of this quantity, as derived from principles of quantum mechanics, is expressed as

$$|\vec{S}| = \hbar\sqrt{I(I+1)} \tag{2.1}$$

where I is the nuclear spin quantum number that assumes values of positive integral multiples of 1/2 (including zero - but values exceeding four are rare), and $\hbar = \frac{h}{2\pi}$, where h is Planck's constant. Within the framework of quantum mechanics, the direction of $|\vec{S}|$ is undetermined until a unidirectional external magnetic field is applied. For instance, the z components of a nucleus' spin, S_z, following the application of an external magnetic field, $\vec{B}_0$, along the z-axis are given by

$$S_z = m_l\hbar \tag{2.2}$$

where $m_l = \pm I, \pm I(I-1), ...$ giving $2l+1$ projections of $|\vec{S}|$ along the arbitrarily chosen axis (z in this case).

The most widely used nucleus in MRI is the proton (^{1}H) as it is the most abundant element in the human body. The proton has a nuclear spin quantum number of 1/2, and m_l assumes values of $\pm 1/2$ corresponding to spin-up (parallel) and spin-down (anti-parallel) values. Since the proton has both charge and angular momentum, its circular motion gives rise to a magnetic field and magnetic dipole moment, $\vec{\mu}_p$. $\vec{\mu}_p$ is related to $|\vec{S}|$ via

$$\vec{\mu}_p = \gamma|\vec{S}| \tag{2.3}$$

where γ is the gyromagnetic ratio (units HzT^{-1}), a constant of proportionality specific to a given nucleus.

The energy of interaction between $\vec{\mu}_p$ and $\vec{B}_0$ is described as

$$E = -\vec{\mu}_p \cdot \vec{B}_0. \tag{2.4}$$

The magnetic moment experiences a torque and will try to align with the field to minimize the energy of interaction. From equations 2.1, 2.2, and 2.3, the equilibrium energy states for protons residing in $\vec{B}_0$ directed along the z-axis are

$$E = -\gamma S_z B_0 = -\gamma m_l \hbar B_0 = \pm\frac{\gamma}{2}\hbar B_0. \tag{2.5}$$

Consequently, protons in the body immersed in $\vec{B}_0$ constitute a system with well-defined energy levels. These levels can be detected by applying secondary, time-varying electromagnetic fields to induce transitions between the energy levels. This effect is known as resonant absorption. Given an externally applied radiowave of frequency, ω_0, the following relationships can be written

$$\hbar\omega_0 = \Delta E = -\gamma\hbar B_0 \tag{2.6}$$

where ΔE is the difference in energy levels for protons immersed in B_0. Equation 2.6 is known as the Larmor relationship, and it describes the connection between the magnitude of $\vec{B}_0$ and the resonant frequency, ω_0, at which nuclei (protons, in this case) precess about the direction of the applied field.

In an equilibrium situation, the number of protons in the lower energy (spin-up) state slightly exceeds the number of protons in the higher energy (spin-down) state. Thus, there exists a net magnetization, $\vec{M}$, within the body. Following excitation, this balance is shifted slightly in favor of spin-down protons. The subsequent emission of radiation that ensues as excited protons relax to their equilibrium state is detectable and forms the basis for signal in MRI. The population distribution of protons in the spin-up ($N\uparrow$) and spin-down ($N_\downarrow$) energy states is described with the Boltzmann distribution

$$\frac{N\uparrow}{N\downarrow} = e^{\frac{-\Delta E}{k_B T_s}} \simeq 1 - \frac{-\gamma\hbar B_0}{k_B T_s} \tag{2.7}$$

where k_B is Boltzmann's constant and T_s is the sample temperature. By Taylor expansion, one can see that the excess of spin-up energy states is quite small at body temperature. At equilibrium, the spin excess is given as

$$(N\uparrow - N\downarrow) \simeq N\frac{\hbar\omega_0}{2k_B T_s} \tag{2.8}$$

where N is the total number of spins in the sample. Despite the spin excess being millions of times smaller than the total spin amount, the incredibly large number of protons in the body (on the order of Avogadro's number per few grams of body tissue) allow for measurable signal generation. At equilibrium, the magnitude of the net magnetization, M_0, is given as

$$M_0 = \frac{\rho_0\gamma^2\hbar^2 B_0}{4k_B T_s} \tag{2.9}$$

where ρ_0 reflects the spin or proton density of the sample. By applying radiofrequency (RF) pulses at the Larmor frequency, $\vec{M}$ is flipped from its equilibrium alignment with B_0 to an angle determined by the duration and strength of the RF pulse [20, 22].

2.3.2 Spin Dynamics and Relaxation

The dynamics of $\vec{M}$ describing its return to equilibrium following excitation are described by the empirical Bloch equation

$$\frac{d\vec{M}}{dt} = \vec{M} \times \gamma\vec{B}_0 - \frac{M_x\hat{x} + M_y\hat{y}}{T_2} - \frac{(M_z - M_0)\hat{z}}{T_1} \tag{2.10}$$

The first term of equation 2.10 describes the motion of free spins under the influence of $\vec{B}_0$, while the last terms account for the relaxation effects following RF excitation. T_1 is a decay constant characterizing the time taken for excited protons to transfer energy that was absorbed during RF excitation to their surrounding environment or lattice. This mode of energy transfer is longitudinal relaxation, as it portrays the dynamics of the z-component of net magnetization following RF excitation. By assuming $\vec{B}_0$ is applied along the z-axis and using appropriate initial conditions, equation 2.10 can be solved for longitudinal relaxation

$$M_z(t) = M_0(1 - e^{-t/T_1}). \tag{2.11}$$

Similarly, relaxation of tranverse components of $\vec{M}$ lying in the plane perpendicular to $\vec{B}_0$ are described via

$$M_\perp(t) = M_0 e^{-t/T_2}. \tag{2.12}$$

Transverse relaxation reflects energy loss that occurs due to spin-spin interactions. As a result, $\vec{M}$ is de-phased and transverse signal is eventually lost at a rate defined by the decay constant, T_2. A second rate constant, T_2^*, embodies phase de-coherence that arises due to both local magnetic field inhomogeneity and spin-spin interactions. T_2^* times are always shorter than T_2 times.

During relaxation, the precession of $\vec{M}$ generates varying magnetic flux in the transverse plane. The changing flux induces a voltage (signal) in a nearby receiving coil that reflects the magnitude of the transverse magnetization as a function of time. Thus, the detected signal is known as free induction decay (FID).

By superimposing gradient magnetic fields on $\vec{B}_0$, the local Larmor frequency is varied. Therefore, spatial localization of signal can be achieved. Depending on the combination of RF pulses and gradients used, a multitude of signals can be generated with MRI to highlight various features of interest in tissue. Pulse sequence diagrams illustrate the temporal relationship between gradients and RF pulses during an MRI acquisition [20, 22].

2.3.3 Dynamic Contrast-Enhanced Magnetic Resonance Imaging

Basic Theory

Dynamic contrast-enhanced MRI (DCE-MRI) involves injecting the patient with a paramagnetic material, such as gadolinium, that affects the T_1 and T_2 relaxation rates of tissues. As gadolinium (Gd) is toxic to humans in its pure form, it is commonly chelated into a relatively safe composition such as Gd-DTPA. As Gd-DTPA has a relatively low molecular weight ($<$ 1000 Daltons), it rapidly diffuses from the vasculature into extracellular spaces. Thus, the contrast agent (CA) accumulates in tissues and relaxation rates are shortened. Since changes in T_1 far exceed alterations in T_2, most DCE-MRI sequences employ fast, T_1-weighted pulse sequences to visualize maximal changes in contrast. By rapidly acquiring T_1 weighted images over time, the dynamics of contrast uptake within tissues can be observed and quantified.

A steady-state incoherent imaging technique was used for T_1-weighted DCE-MRI imaging of VSs. Steady-state incoherent imaging with gradient echoes enables very fast imaging by reducing the repetition time, T_R, between RF excitation pulses. Use of a fast imaging sequence is tantamount for adequate time resolution of the dynamic processes involved in contrast uptake in tissues. Since $T_R < T_1$ and, often $T_R \leq T_2$, the longitudinal magnetization and/or transverse magnetization does not fully relax to its thermal equilibrium value prior to the next excitation pulse. However, by intentionally using RF spoiling pulses to effectively destroy any residual transverse magnetization, only the longitudinal component of magnetization abides. Thus, the transverse magnetization remaining before the subsequent excitation pulse is rendered incoherent (spoiled), and the generated signal is inherently T_1-weighted. Clearly, tissues with shortened T_1 times will generate more signal as their longitudinal recovery is faster - making more magnetization available for subsequent RF excitation.

Following the application of several RF excitation pulses, a dynamic equilibrium, known as the steady-state, is established where the same longitudinal magnetization exists before each RF pulse. The steady-state is marked by identical behavior and magnetization values within each RF cycle (for each T_R). This situation is realized when the loss in longitudinal magnetization following an RF excitation pulse is completely re-grown between pulses.

The following is a derivation, based on Haacke et al. [22], of the signal

generated from a simplified steady-state incoherent imaging sequence. Instead of using spoiling gradients to de-phase the transverse signal, $T_R >> T_2$, creating a situation where transverse signal is "naturally" nullified. The result, however, applies equally as well to pulse-sequences employing RF spoiling pulses, such as fast low-angle shot (FLASH) - a spoiled gradient echo sequence.

Immediately after the first RF excitation pulse (time = 0^+), the longitudinal magnetization is

$$M_z(0^+) = M_0 \cos\theta \tag{2.13}$$

and the transverse magnetization is

$$M_\perp(0^+) = M_0 \sin\theta \tag{2.14}$$

where $M_{z,\perp}(0^+)$ is symbolic of magnetization **immediately following** excitation, and M_0 is the value of longitudinal magnetization at thermal equilibrium. The transverse magnetization at a time t_n following the application of an RF excitation pulse giving a flip angle θ decays according to

$$M_\perp(t_n) = M_\perp(0^+)e^{-t_n/T_2}, \quad 0 < t_n < T_R \tag{2.15}$$

where t_n is the relative time within each cycle, defined as

$$t_n \equiv t - nT_R \tag{2.16}$$

and t is the total time from the first excitation pulse. In the spoiled case, any residual transverse magnetization at T_R would be destroyed. The longitudinal magnetization re-grows during this same period via

$$M_z(t_n) = M_0 - (M_0 - M_z(0^-))e^{-t_n/T_1} \tag{2.17}$$

where $M_z(0^-)$ is the longitudinal magnetization that is **available for excitation** in a given cycle at a time ($= 0^-$) just prior to application of the next excitation pulse.

After n pulses, the transverse magnetization is

$$\begin{aligned} M_\perp((n+1)T_R^-) &= M_\perp(nT_R^+)e^{-T_R/T_2} \\ &= M_z(nT_R^-)\sin\theta e^{-T_R/T_2} \end{aligned} \tag{2.18}$$

where the expression for transverse magnetization has been substituted using equation 2.14 with M_0 replaced by $M_z(nT_R^-)$, the total amount of recovered

longitudinal magnetization available for excitation by the n^{th} pulse. As the exponential in equation 2.18 goes to zero, so does the transverse magnetization. The longitudinal magnetization recovered after the n^{th} pulse is

$$M_z((n+1)T_R^-) = M_z(nT_R^-)\cos\theta e^{-T_R/T_1} + M_0(1 - e^{-T_R/T_1}). \tag{2.19}$$

After many RF pulses have been applied, the amount of longitudinal magnetization that is recovered due to T_1 decay will equal the amount of longitudinal magnetization that is lost due to RF excitation. Assuming that this steady-state is reached by the n^{th} pulse, the steady-state equilibrium value of M_z is defined as

$$M_z(mT_R^-) = M_{ze}, \quad m \geq n. \tag{2.20}$$

With some rearrangement of equalities, the steady state signal (representing transverse magnetization from a 3-dimensional sample volume, known as a voxel) following the application of an RF pulse with a flip angle θ is

$$S(\theta, T_E) = \frac{S_0 \sin\theta(1 - e^{-T_R/T_1})}{1 - e^{-T_R/T_1}\cos\theta} e^{-T_E/T_2^*} \tag{2.21}$$

where t_n has been replaced with T_E, the "echo time" at which the signal is acquired, S_0 is substituted for M_0, and T_2^* replaces T_2 [22, 26]. It is important to note that a "voxel" is a 3-dimensional sample volume (usually cubical) that is ultimately represented as a pixel, or 2-dimensional map. Thus, contributions to the effective pixel signal arise from a finite depth that is defined by the voxel's dimensions.

FLASH was used for DCE-MRI of VSs. Since $T_E << T_2^*$, the signal from FLASH can be written as

$$S(\theta, T_E) = \frac{S_0 \sin\theta(1 - e^{-T_R/T_1})}{1 - e^{-T_R/T_1}\cos\theta}. \tag{2.22}$$

Allowing $S(\theta, T_E)$ to vary with time as $S(t)$ and setting $S_0 = S(t = 0)$, we can solve for T_1 of tissues post-CA administration (T_{1post}) throughout time

$$T_{1post}(t)^{-1} = \frac{-1}{T_R} \ln\left(\frac{S(t) - S(0)\sin\theta}{S(t)\cos\theta - S(0)\sin\theta}\right) = R_{post}(t) \tag{2.23}$$

where $R_{post}(t)$ is the relaxation rate at time t. Within the range of concentrations used for DCE-MRI of VSs, relaxation rates are linearly related to changes in CA concentration. Thus, quantifying changes in relaxation rates is imperative for meaningful quantitative analysis of CA uptake. Differences

in $R_{post}(t)$ and R_{pre} - the relaxation rate prior to contrast administration - are related to changes in CA concentration, $[C]$, via

$$R_{post} - R_{pre} = a([C]_{post} - [C]_{pre}) \quad (2.24)$$

$$\Delta R = a\Delta[C] \quad (2.25)$$

where a is a constant determinable from a calibration scan where concentrations of CA are precisely known. Note that equation 2.25 is merely an alternate form of equation 2.24. The constant of proportionality, a, is known as the relaxivity.

In order to determine baseline, or pre-contrast T_1 values, two repetitions of the FLASH sequence are used to eliminate the unknown quantity $S(0)$ in equation 2.23. Since the inherent properties of tissues are not affected by the timing of pulse sequences, $S(0)$ is constant from scan to scan. Either T_R or the flip angle is varied while all other parameters are kept constant. For example, repetition one with $\theta = \theta_1$ gives signal S_1, and repetition two with $\theta = \theta_2$ yields signal S_2 as

$$S_1 = S(0)\sin\theta_1 \frac{1 - e^{-T_R/T_1}}{1 - \cos\theta_1 e^{-T_R/T_1}} \quad (2.26)$$

$$S_2 = S(0)\sin\theta_2 \frac{1 - e^{-T_R/T_1}}{1 - \cos\theta_2 e^{-T_R/T_1}}. \quad (2.27)$$

Taking the ratio of S_1 to S_2 and solving for T_1 gives the pre-contrast T_1 value

$$T_1^{-1} = -\frac{1}{T_R}\ln\left(\frac{1 - \frac{S_1\sin\theta_2}{S_2\sin\theta_1}}{\cos\theta_2 - \frac{S_1\sin\theta_2}{S_2\sin\theta_1}\cos\theta_1}\right) \quad (2.28)$$

which can be substituted for T_1 in equation 2.26 or 2.27 to solve for $S(0)$

$$S(0) = S_{1,2}\frac{(1 - \cos\theta_{1,2}e^{-T_R/T_1})}{\sin\theta_{1,2}(1 - e^{-T_R/T_1})}. \quad (2.29)$$

Once $S(0)$ is known, relaxation rates can be calculated using equation 2.23 and concentrations can be computed from equation 2.24.

Returning briefly to equations 2.24 and 2.25, a sample calculation of relaxivity is

$$a = \frac{{T_{1m}}^{-1} - {T_{1n}}^{-1}}{[C_m] - [C_n]} \quad (2.30)$$

where $m, n = 1, 2, ...k$, representing k samples with known concentrations of CA. T_1 values are determined from equation 2.28. Ultimately, concentrations of CA are computed throughout the dynamic acquisition since

$$\Delta[C(t)] = \frac{1}{a}\left(T_{1post}(t)^{-1} - T_{1pre}{}^{-1}\right) \tag{2.31}$$

[22].

Justification for Flip Angles Used

Two important factors must be considered when deciding what flip angle to use during DCE-MRI. First, there must be adequate overall signal to achieve a useful signal to noise ratio. Second, there should be good contrast between the region of interest (tumor) and healthy surrounding tissue throughout the dynamic acquisition. Maximizing contrast enables the visualization of a range of CA concentrations during the time course of image acquisition. In other words, there must be a balance between signal intensity and contrast for a decent depiction of CA dynamics. The signal from a FLASH sequence as described by equation 2.22 is maximized with respect to flip angle θ to give θ_E - the Ernst angle

$$\theta_E = \cos^{-1}(e^{-T_R/T_1}). \tag{2.32}$$

For two tissues with relaxation times T_a and T_b, a FLASH imaging sequence yields a signal difference (contrast), based on equation 2.22, of

$$\Delta S = \sin\theta\left(\frac{1-E_a}{1-\cos\theta E_a} - \frac{1-E_b}{1-\cos\theta E_b}\right) \tag{2.33}$$

where $E_{a,b} = e^{-T_R/T_{1a,b}}$. According to Haselhoff [23], maximizing contrast with respect to flip angle results in θ_d - the flip angle yielding the greatest contrast between two tissues with T_1 values T_a and T_b

$$\theta_d = \cos^{-1}\left(\frac{-E_1^2 + E_1 - 1 + d^2 + \sqrt{E_1^4 - E_1^2(2d^2+2) + d^4 - d^2 + 1}}{E_1^2 - 2E_1 - d^2}\right) \tag{2.34}$$

where

$$d = \frac{|e^{-T_R/T_a} - e^{-T_R/T_b}|}{2}$$

and

$$E_1 = \frac{e^{-T_R/T_a} + e^{-T_R/T_b}}{2}.$$

Figure 2.1 depicts the θ_E and θ_d for a range of T_1 values. θ_d is the flip angle giving maximum contrast for a given T_1 as compared to $T_1 = 950\ ms$ - the approximate T_1 value of healthy gray matter at 1.5 T. Since the cerebellum surrounds most VSs and it is made of gray matter, this T_1 was chosen to represent the neighboring healthy parenchyma.

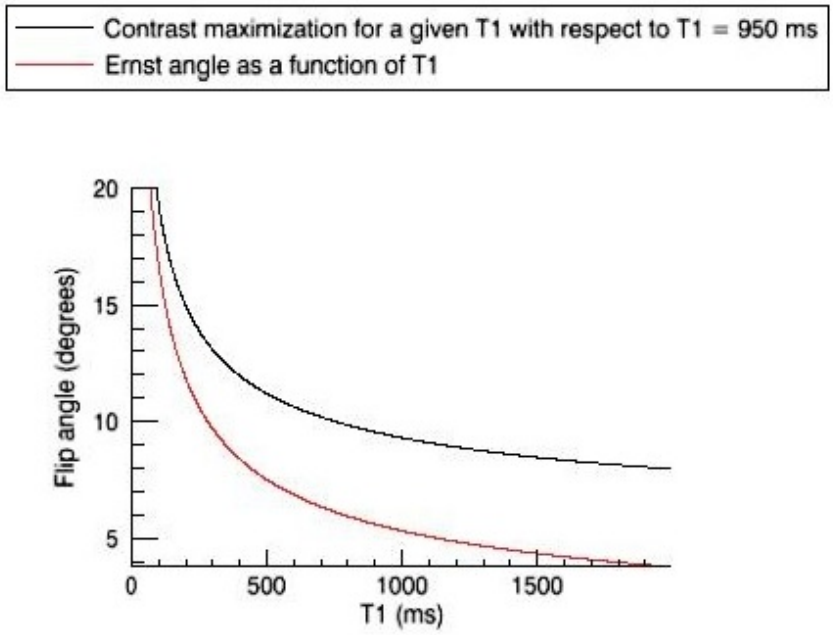

Figure 2.1: Flip angle to optimize contrast and signal as a function of T_1 for $T_R = 4.3\ ms$. The range expected is $200 - 1800\ ms$ with T_1 values shortening with contrast arrival.

As CA tends to accumulate rather quickly in tumor tissue (perfusion-limited), a flip angle of 15° was chosen to provide maximal contrast following CA injection. This flip angle should also provide adequate contrast and signal for the range of T_1 values expected ($200 - 1800\ ms$). Note that in Figure 2.1, contrast is zero at $T_1 = 950\ ms$. That is, contrast is maximized for T_1 values infinitesimally close to $T_1 = 950\ ms$ at the corresponding flip angles in the graph, but there ceases to be any contrast between tissues with

identical T_1 values.

Contrast Agent Behavior and Pharmacokinetic Modeling

Following bolus injection of a CA, three main events occur. First, during the "first pass" the CA passes through the capillary bed, where it is temporarily confined within blood plasma of the intravascular space (IVS). In most tissues, this only lasts for a few cardiac cycles. Due to the presence of the blood-brain barrier (BBB) in the healthy brain, however, CA cannot escape from the IVS. Brain tumors, such as VSs, are often associated with abnormal vasculature and BBB abnormalities (or entire absence). Thus, in the second step of CA kinematics, the CA passes from the IVS into the extravascular-extracellular space (EES) of the VS. The rate of passage of the CA into the EES depends on factors such as blood flow and the permeability and surface area of microvessels. Once the CA has entered the EES, it does not cross the cell membrane and diffusion within the EES governs its behavior. An estimated 12-45% of CA leaks into the EES within the first pass. In the case of brain tumors, where vascular permeability far exceeds inflow of blood, blood perfusion is usually the factor that dominates delivery of CA to the tumor. Alternatively, in situations where the blood-brain barrier is intact, CA transport to the EES is controlled mostly by transport across endothelial (capillary) walls. Finally, after several minutes or hours (depending on the properties of the tissue), the CA diffuses back into the IVS and is eventually excreted. These dynamics are modeled in Figure 2.2 [17].

Once the CA has accumulated in a region of interest, it causes shortening of T_1 values in its vicinity. Thus, changes in CA concentration can be estimated using the techniques described in Section 2.3.3. Furthermore, models representing the kinematics of CA within the body, such as the two compartment model depicted in Figure 2.2, enable the estimation of rate constants describing the movement of CA within the body.

The two-compartment model shown in Figure 2.2 is known as the modified Kety model [62] and is described mathematically as

$$C_t(t) = v_p C_p(t) + K_{trans} \int_0^t C_p(t') e^{\frac{-K_{trans}}{v_e}(t-t')} dt'. \tag{2.35}$$

Note that variables are defined graphically in Figure 2.2. K_{trans} is a rate constant describing the transfer of contrast agent between the blood plasma and the extra-vascular extra-cellular space (EES), v_e is the fractional volume

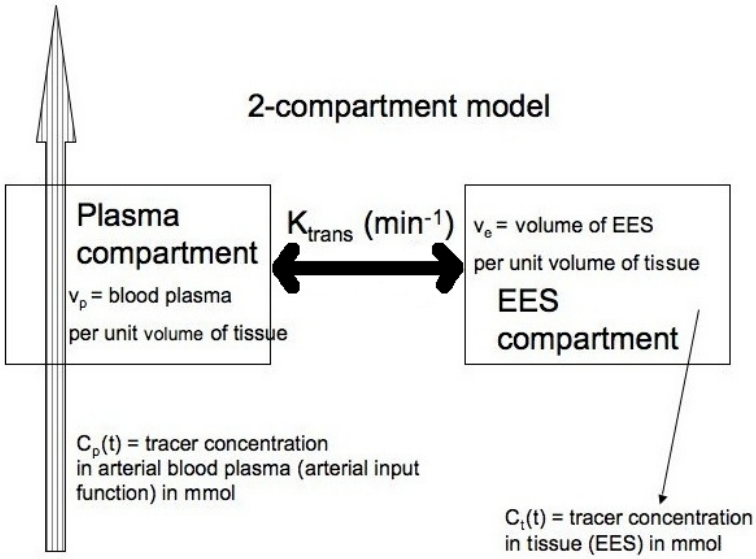

Figure 2.2: Two-compartment model of contrast-agent dynamics.

component of the EES per unit volume of tissue, and v_p is the fractional blood plasma volume per unit volume of tissue.

DCE-MRI of VSs

In a DCE-MRI study by Ikushima et al. [25], VSs showed a slow but steady increase in enhancement following administration of gadopentate dimeglumine. No peak was observed during the 210 s scan duration, and images were acquired every 30 s. The authors placed ROIs on solid tumor regions, and avoided discernibly cystic and necrotic areas. Enhancement was characterized as homogeneous, and the gradual pattern of enhancement differed from that observed for meningiomas - which was much more rapid.

A similar pattern of CA uptake in VSs was observed by Vogl et al. [65]. There was no wash-out or drop-off effect observable within the scanning duration of 360 s, but there was lots of variation in the value at which signal plateaued.

Cha et al. [13] examined seven patients with meningioma, a benign brain tumor that is similar in location and size to vestibular schwannoma, using steady-state T_1-weighted DCE-MRI. Reported K_{trans} values for this population ranged from 0.04 to 1.4 min^{-1}. These tumors were considered

to be highly vascular without much presence of a blood-brain barrier. This range of K_{trans} may serve as a guide for the K_{trans} values expected for vestibular schwannomas.

Thus, it is reasonable to expect VSs to exhibit relatively gradual increases in CA accumulation based on previous observations [25, 65]. Cystic or necrotic components within VSs are likely to appear hypointense, since these regions are removed from the main vasculature. Moreover, fibrotic tissue arising as a result of radiation damage is likely to appear hypointense due to its reduced blood vessel density relative to viable tumor tissue. Disruptions in vasculature caused by radiotherapy could manifest as altered uptake patterns. Furthermore, regions that were previously hyperintense could appear hypointense with the onset of radiation-induced fibrosis and necrosis. Enhancement in these regions is primary governed by diffusion, and it is likely to occur very slowly.

2.3.4 Diffusion Tensor Imaging

Protons within water molecules tend to move in random directions in a manner that depends on the local properties of the tissue they are immersed in. Properties of tissues affecting the diffusion of water include cellular density (relating to tissue type), edema, cysts, necrosis, local vascularity/perfusion, and generalized motion of the tissue (i.e. from voluntary or involuntary body movements). For instance, water within cysts tends to move relatively freely - leading to large diffusion coefficients. Conversely, water in the EES of dense tumor tissue is impeded by the presence of numerous cell walls and demonstrates relatively low diffusion coefficients. Transverse magnetization decays at the usual rate determined by T_2, but suffers from additional decay governed by T_2^* once a gradient is applied. By applying a pair of symmetric, uniform gradient pulses (with a spin-echo 180° RF pulse between them) to first de-phase, and then re-phase signal lost to T_2^* decay, protons in water that have moved between gradient applications will fail to re-phase - causing a reduction in signal that is secondary to unrecoverable T_2 decay. This is known as the Stejskal-Tanner experiment. To describe this experiment further, suppose that the proton travels to a new position every t_d seconds, in an small step size of δ, and that it is subjected to a pair of symmetric, unidirectional gradient pulses G that are separated by a 180° RF pulse within the main magnetic field. In addition, it is assumed that a spin-echo sequence is used with an echo time T_E. After a large number steps, N, the net signal after the first echo is given as

$$S = S(0)e^{-D\gamma^2 G^2 T_E^3/12} e^{-T_E/T_2} \tag{2.36}$$

where $S(0)$ is the signal without diffusion gradients, S is the signal after diffusion gradients are applied, and $D = \delta^2/2t_d$ - the diffusion coefficient for this particular model of diffusion. The Stejskal-Tanner method reflects scalar, or one-dimensional diffusion only. Equation 2.36 is commonly written as

$$S = S(0)e^{-bD}e^{-T_E/T_2} \tag{2.37}$$

where $b = \gamma^2 G^2 {T_E}^3/12$. This is typically referred to as the 'b-value', and it is quadratically related to the strength of the diffusion gradient [22].

In diffusion tensor imaging, diffusion gradients are applied in a minimum of 6 non-colinear, non-coplanar directions with at least two different b-values (zero and one non-zero) to acquire a set of diffusion weighted images (DWIs). As the gradient directions are varied, the images will reflect the amounts of diffusion along the direction of each gradient's application. DWIs must be acquired in a minimum of 6 directions to enable the determination of the complete diffusion tensor $\vec{D}$. Six, rather than nine directions are required since $\vec{D}$ is a symmetric matrix ($D_{ij} = D_{ji}$). Taking into account the tensor nature of this form of diffusion imaging, the acquired signal is related to the diffusion coefficients (for each given direction) and the symmetric matrix of b-values by

$$\ln\left(\frac{S(\vec{b})}{S(\vec{b}=0)}\right) = -\sum_{i=1}^{3}\sum_{j=1}^{3} b_{ij}D_{ij} \tag{2.38}$$

where $S(\vec{b})$ represents the signal acquired for a given element of the b-matrix. Note that the b-matrix encapsulates the attenuating effects of all diffusion gradients (applied in all six directions) [5].

Following acquisition of a set of DWIs, $\vec{D}$ can be estimated by fitting equation 2.38 to each voxel signal using multivariate linear regression. Since $\vec{D}$ is also limited by the diffusion time (duration of gradient pulses used), it is really an estimate of the true diffusion. Thus, elements of the diffusion tensor are commonly referred to as the apparent diffusion coefficients (ADCs). This technique is particularly useful when anisotropy within tissues is expected. An example of healthy, anisotropic brain parenchyma is white matter. Water diffuses preferentially along the longitudinal axis of neuron axons, while axial movement is restricted by axons' walls. Local variations in tumor cell density (reflecting histological cell type), cyst formation, necrosis, and regional differences in vascularity are all possible in VSs. Therefore, tissue isotropy cannot be assumed and diffusion tensor imaging enables examination of the anisotropy of VSs.

Once $\vec{D}$ is estimated, the mean diffusivity (MD), or orientationally averaged value of $\vec{D}$, is given as

$$\langle D \rangle = \frac{(D_{xx} + D_{yy} + D_{zz})}{3} \tag{2.39}$$

or

$$\langle \lambda \rangle = \frac{(\lambda_1 + \lambda_2 + \lambda_3)}{3} \tag{2.40}$$

where λ represents the eigenvalues of the diffusion tensor. Another quantity of interest is fractional anisotropy (FA). FA is a higher moment of $\vec{D}$ that characterizes the extent to which tissues deviate from isotropic behavior

$$FA = \sqrt{\frac{3((\lambda_1 - \langle\lambda\rangle)^2 + (\lambda_2 - \langle\lambda\rangle)^2 + (\lambda_3 - \langle\lambda\rangle)^2)}{2(\lambda_1^2 + \lambda_2^2 + \lambda_3^2)}}. \tag{2.41}$$

One method of performing DTI is through the use of echo planar imaging (EPI) sequences. EPI can be single or multi-shot, meaning one or several excitation pulses can be used to generate a signal. In single-shot EPI, gradients are rapidly switched on and off following excitation in both the phase and frequency-encoding directions while signal is constantly acquired. Gradients are varied in a systemic manner so that diffusion-weighted data from the entire field of view (FOV) are recorded. EPI sequences enable rapid data acquisition so that imaging times are relatively short. Figure 2.3 illustrates a single-shot EPI sequence.

Diffusion-Weighted Magnetic Resonance Imaging of VSs

In a study of diffusion weighted MRI of VSs, Pavlisa et al. [47] observed that VSs had higher ADCs compared to meningiomas. During analysis, obvious regions of cystic or necrotic tissue were excluded. The authors hypothesized that higher ADCs were likely due to lower cellular density in VSs. They proposed that elongated Schwann cells may have contributed to a higher degree of water diffusion, as compared to meningiomas. Additionally, it was thought that the EES of VSs contained an excess of microcystic components contributing to the higher overall ADC values.

Sener et al. [57] examined 6 pathologically confirmed VSs using DWI. There was no evidence of gross cystic degeneration, fatty degeneration, or hemorrhage in the tumors, although some small cysts were present. Normal ADCs of the pons, middle cerebellar peduncle, and cerebellum were obtained for comparison. VSs were noted to be isointense to normal brain

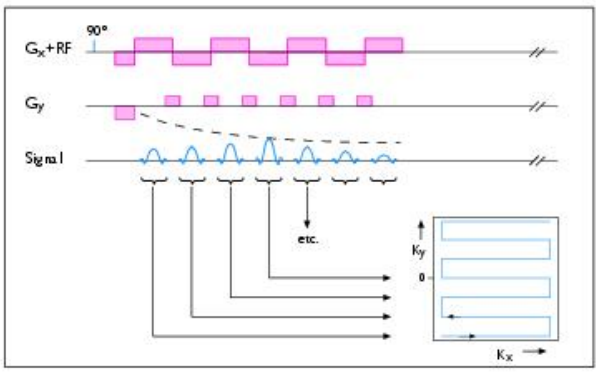

Figure 2.3: Single-shot EPI pulse sequence showing sequential coverage of FOV in k-space. G_x represents gradients applied along the x axis, while G_y shows gradients applied in the y direction. Echoes (when signal is acquired) are shown along the *Signal* axis of the diagram [2].

parenchyma, and their ADCs were prominently larger than those of the control regions. The authors suggested that this indicated relatively low nuclear to cytoplasm ratios causing increased movement of water within VSs. This is in accordance with observations made by Pavlisa et al. [47]. The authors concluded that VSs were "solid tumors with a relatively loose extracellular matrix".

Bonneville et al. [10] stated that DWI of solid VSs commonly reveals elevated ADCs as compared to healthy parenchyma. The range of reported ADC values was $[1.1 - 1.7] \cdot 10^{-3}\ mm^2/s$.

In agreement with previous reports, Yamasaki et al. [67] found that ADCs were higher for VSs versus meningiomas. The mean ADC was within the range provided by Bonneville et al. [10]. The authors suggested that higher ADCs may be reflective of lower density Antoni B type cellularity in VSs.

Thus, VSs are expected to demonstrate elevated diffusion tensor components relative to healthy brain parenchyma. Depending on the degree of tissue anisotropy present before and after radiation therapy, FA values may increase or decrease depending on the degree of tissue destruction induced by treatment. In addition, ADCs may aid in identifying tumors with predominantly Antoni type A or B cellularity.

2.3.5 Magnetic Resonance Spectroscopy

Basic Theory

Magnetic resonance spectroscopy (MRS) is a non-invasive technique that enables the *in vivo* observation of metabolites, or chemical compounds, involved in biochemical processes in the body. Since most metabolites contain ^{1}H, some can be visualized using standard MRI hardware. MRS harnesses the chemical shift - a physical phenomenon causing local magnetic field variations due to differing chemical environments- to measure metabolite concentrations in selected volumes of interest (VOI). In other words, the local magnetic field that determines a proton's Larmor frequency (see equation 2.6) is really the sum of the externally applied magnetic field, B_0, and the small magnetic fields generated by electrons and protons in the surrounding molecular structures. Thus, resonant frequencies of metabolites differ in a manner that is directly related to chemical structure.

As a consequence of the chemical shift, the Larmor frequency is modified to

$$\omega_{eff} = \gamma B_0(1 - \chi) \tag{2.42}$$

where χ is the shielding or screening constant - a quantity reflecting local magnetic field variations caused by a proton's surrounding chemical environment - and B_0 is the main magnetic field. In general, χ is a tensor quantity, since chemical environments can be anisotropic. To enable universal comparisons of metabolite concentrations, chemical shift is expressed as a parts per million (ppm) deviation from a standard reference frequency

$$\delta = \frac{f_{sample} - f_{ref}}{f_{ref}} \cdot 10^6 \tag{2.43}$$

where f_{sample} is the measured frequency of the sample, and f_{ref} is the frequency of the standard reference sample. This approach permits direct comparisons of metabolite concentrations - regardless of B_0. The most commonly used reference standard is tetramethylsilane where $\delta \equiv 0$. Due to its molecular symmetry, all 12 protons resonate at the same frequency [63].

Shimming

Since the aim of MRS is to identify abundances of metabolites based on their local chemical environments, achieving a high degree of homogeneity (shimming) in B_0 is imperative. Ideally, resonant frequencies within a VOI will vary solely as a result of chemical shift. Realistically, there will always

be some magnetic field inhomogeneity. In regions where there are abrupt variations in magnetic field susceptibility, such as in sinus cavities or near tissue/bone junctions, it becomes very difficult to correct adequately for inhomogeneities. This was a particular concern in this study, since small to medium-size VSs are in close proximity to bone and air cavities of the inner ear.

Once a VOI is selected with the aid of a localizing high resolution MRI sequence, shimming is accomplished by employing specially designed gradient coils. Such coils are designed to generate small, non-uniform magnetic fields to counteract the effects of magnetic susceptibility differences. Linear, quadratic, and even cubic-order corrections can be applied to correct for various magnetic field variations. Due to the small effect of chemical shift, a magnetic field uniformity with ≤ 0.1ppm variation is necessary to accomplish decent metabolite resolution. Usually, the goal is to minimize the line width of the water peak at full-width half-maximum[63].

Water suppression

Since the signal from water can be $\sim 1000 - 20000$ times larger than the signals from metabolites, the water signal must be suppressed to allow for observations of metabolites. One method of water suppression involves the use of chemical-shift selective pulses. Following shimming, an RF excitation pulse - tuned specifically to the resonant frequency of water - is used to tip the magnetization from water into the transverse plane. Immediately following excitation, the transverse magnetization is destroyed. The spectroscopy sequence commences before the magnetization from water can recover, so there is no magnetization from water available for excitation during acquisition of the spectrum [63].

Volume localization

One technique used for selecting a cubic VOI in MRS is point resolved spectroscopy (PRESS). Typically, volumes of $1 - 10$ mL are acquired. In PRESS, a 90° selective pulse is used in the presence of a gradient to excite a small slab of spins. Next, a 180° selective pulse (also in the presence of a gradient) refocuses magnetization where the two slabs intersect. Finally, a second 180° selective pulse causes a second echo where all three slabs intersect. Therefore, the echo is generated from a cubic region formed at the intersection of all three excited slabs. Often, spoiling gradients are used to destroy undesired magnetization from outside of the VOI. This sequence

is illustrated in Figure 2.4.

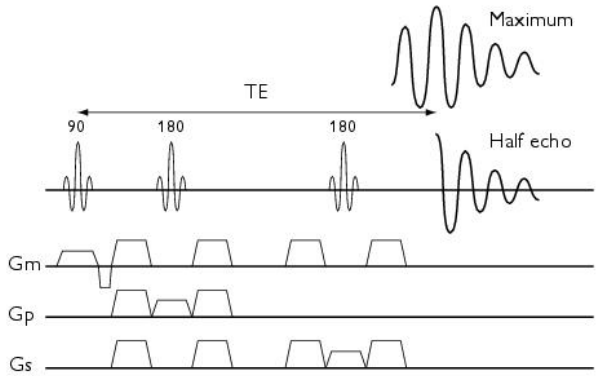

Figure 2.4: PRESS imaging sequence. Notice the slice selective gradients applied along three orthogonal directions (G_m, G_p, and G_s) during the application of excitation pulses. Spoiling gradients are used before and after refocussing pulses to destroy undesirable magnetization [2].

By using shorter T_E times ($\leq$ 50ms), more metabolite peaks can be resolved due to reduced T_2 losses. When analyzing data, signal is plotted as a function of frequency, and proton concentration is proportional to the area under a metabolite peak when

$$T_R \gg T_1 \tag{2.44}$$

$$T_E \ll T_2. \tag{2.45}$$

Equation 2.44 is usually satisfied by making $T_R = 2$ or 3 seconds, thus allowing almost complete recovery of longitudinal magnetization. The second condition of equation 2.45 is never completely satisfied, as many metabolites have sub-millisecond values of T_2. However, many important metabolites can be resolved by using $T_E \leq$ 50ms.

To achieve adequate signal to noise ratios (SNR), many acquisitions or echoes are necessary for signal averaging and noise reduction. SNR is increased by averaging according to

$$SNR = SNR_0 \left(\frac{T_{exam}}{T_R}\right)^{1/2} VOI \tag{2.46}$$

where SNR_0 is the SNR for one acquisition, $T_{exam} = NEX \cdot T_R$, NEX is the number of averages or acquisitions, T_R is the sequence repetition time, and VOI is the size of the VOI [63].

Quantifying Metabolite Concentrations

Following signal acquisition, signal peaks are fitted using reference models to estimate metabolite concentrations. A popular method of curve fitting is the linear combination model (LC Model) [63]. One implementation of the LC Model fits the signal/frequency curve by using a 'basis set' composed of a separate spectrum for each metabolite that is likely to be present in the data set (based on the scanner, particular sequence parameters, and physiological location). The acquired spectrum is compared with a linear combination of the basis set to generate a spectrum of best fit. The coefficients for the basis functions are found to provide the best fit possible (based on a pre-decided minimization scheme), and they yield the estimated concentration of each basis metabolite. Uncertainty in the estimates is measured with Cramer-Rao minimum variance bounds. A pre-processing step for eddy-current correction is made by using an unsuppressed water spectrum from the same VOI [63].

An empirical expression for the *in vivo* metabolite concentration $C(r)$ at location r as derived from an external standard is

$$\begin{aligned} C(r) &= \frac{S(r)}{S_s b_1(r)} C_s \frac{n_p^s}{n_p} \frac{VOI_s}{VOI} \frac{1}{f_v} \frac{V}{V_s} \frac{T_{37}}{T_s} \\ &\times \frac{1}{R[b_1(r)\pi/2]} \frac{f_1(T_1^s)}{f_1(T_1)} \frac{f_2(T_2^s)}{f_2(T_2)} \end{aligned} \tag{2.47}$$

where $S(r)$ is the signal acquired at r, $S_s b_1(r)$ is an externally acquired signal from a standard phantom, and $b_1(r)$ is an RF field map that describes RF non-uniformity - this is usually taken as 1 from the centre of a bird-cage head coil where the field is fairly uniform. n_p equals the number of protons in the metabolite *in vivo* or in the standard n_p^s. For example, $n_p = 9$ for choline and 3 for creatine. VOI is the size of the volume of interest from which the signal is obtained, f_v is the volume fraction of the VOI containing brain parenchyma (vs. containing cerebrospinal fluid - which has very few metabolites), V is the transmitter voltage for the *in vivo* experiment, and V_s is the transmitter voltage in the standard experiment. T is the absolute temperature, T_{37} is body temperature, and T_s is the standard (phantom) temperature. $R(\theta)$ is the response function for a given spectroscopic imaging

sequence. Note that $R(\pi/2) = 1$. $f_1(T_1)$ and $f_2(T_2)$ represent the signal losses due to T_1 and T_2 decay and are approximately equal to

$$\begin{aligned} f_1(T_1) &= 1 - exp(-T_R/T_1) \\ f_2(T_2) &= exp(-T_E/T_2) \end{aligned} \tag{2.48}$$

for the PRESS imaging sequence [63].

Physiological Significance of Metabolite Levels

Table 2.1 summarizes the major metabolites in the brain observable with a short-T_E PRESS imaging sequence. Healthy concentration ranges of metabolites in the adult brain are provided. These ranges help to identify elevated or depressed metabolite concentrations that can be associated with the pathologies described in the table.

Table 2.1: Description of primary brain metabolites [63].

Metabolite	Quantification		Physiology	↑ or ↓
	Chemical Shift (ppm)	Concentration (mean/range in mmol)		
N-acetyl aspartate (NAA)	2.02	7.8/6.5-9.7	-marker of healthy neurons -only observed in nervous tissue -exact physiological function unknown	↓ with neuron losses, dysfunction, ischaemia, trauma, inflammation, **tumors**, infection, dementia, gliosis
Total Choline (Cho) - various forms	3.2	1.3/0.8-1.6	-indicator of membrane turnover -higher in white matter than gray matter -↑ with age	↑ in **tumors**, inflammation, chronic cell hypoxia
Creatine (Cr)	3.0	4.5/3.4-5.5	-possible indicator of energetic/metabolic state of cells -associated with compounds involved in energy storage -often described as ratio to Cr	-↑ with trauma, hyperosmolar states -↓ in hypoxic states, stroke, **tumors**
Myo-inositol (mI)	3.56	3.8/2.2-6.8	-pentose sugar that is involved in inositol triphosphate intracellular second messenger cycle -osmolyte (organic molecule affecting cellular osmosis) -marker of glial cells	↑ neonates, Alzheimer's, diabetes, low-grade glioma, postencephalopathy, hyperosmolar states ↓ malignant tumors, chronic hepatic encephalopathy, stroke
Continued on next page				

Table 2.1 – continued from previous page

Metabolite	Quantification		Physiology	↑ or ↓
	Chemical Shift (ppm)	Concentration (mean/range in mmol)		
Lactate	1.35	≥ 1 to detect	-not observable in healthy brain -final product of anaerobic respiration -higher in foamy macrophages	↑ ischemia, native metabolic problems, **tumors - all grades**, abscesses, inflammation
Lipids	0.9/1.3	need very short T_E	-not seen in healthy brain -indicative of cell membrane degeneration and lipid droplet formation -may precede necrosis	↑ high-grade tumors, abscesses, acute inflammatory states, acute stroke

As mentioned earlier, MRS of small to medium-VSs is expected to be quite difficult. To date, few MRS studies of VSs have been published. In proton MRS of VSs and other BTs, Cho et al. [15] report markedly elevated levels of mI in 10 of 11 pathologically confirmed VSs. Furthermore, there were elevated levels of Choline which the authors attributed to increased membrane synthesis in rapidly proliferating cells, and the breakdown of phosphatidylcholine - a compound that releases MRS-detectable cholines in viable BTs. Phosphatidylcholine degradation is not, however, dependent on tumor malignancy. Also, reduced levels of NAA and Cr were noted in many VSs. Relatively large lipid signals were detected in 7 of 13 VSs.

Based on the description of their experiment, Cho et al. examined fairly large VSs. A VOI was selected within the center of the tumor in the CPA, so shimming was probably relatively straightforward. This will not likely be the case in this study, since smaller VSs are more commonly encountered and shimming presents considerable difficulties. However, the findings of Cho et al. provide some trends to watch for in MRS of VSs. Success of radiotherapy of VSs could be marked by reductions in previously elevated mI and Cho levels, or increases in formerly depressed NAA and Cr concentrations.

2.4 Positron Emission Tomography

2.4.1 Imaging with Radioisotopes

Atomic nuclei with excess numbers of protons or neutrons are unstable and decay to more stable states by emitting various forms of radiation. In positron emission tomography (PET), positron emitting radioisotopes are used for *in vivo* imaging of different metabolic processes in the body. Positrons are produced by nuclei with an excess number of protons via β^+ decay, where a bound proton is converted into a neutron n, positron β^+, and neutrino ν_e

$$p \rightarrow n + \beta^+ + \nu_e. \tag{2.49}$$

Energy and momentum are conserved by neutrino emission, and positrons are ejected with variable energies. After emission, the positron loses kinetic energy as it interacts with local matter. Eventually, the positron comes to rest and annihilates with an electron (its anti-matter counterpart) to produce two anti-parallel 511 keV photons. This form of decay occurs in radioisotopes such as ^{11}C, ^{13}N, ^{15}O, and ^{18}F.

A widely used method of producing radioisotopes for PET imaging is charged particle bombardment. This technique employs the use of a parti-

cle accelerator, such as a LINAC or a cyclotron, to bombard stable nuclei with charged particles. Charged particles like protons or D^+ are accelerated through potentials of up to 100 MeV to overcome the repulsive nuclear forces of the target material. Upon impact, proton rich radioisotopes result [20].

Once the desired radioisotope is produced, it may be inserted into a molecule of biological interest to create a radiopharmaceutical or radiotracer. Through this radioactive labelling, distributions of molecules can be mapped as they progress through various biochemical pathways in the body. Theoretically, any type of molecule can be labelled with a radioisotope. Qualities affecting chemical behavior include electronegativity and volume, for example. In addition, the amount of radiotracer introduced should be small enough so as not to perturb the dynamics of the system being studied. The sensitivity of PET detectors allows the implementation of this "tracer principle". Many compounds native to the human body, such as glucose and amino acids, can be effectively radiolabelled to enable the study of processes like glucose metabolism and protein synthesis, respectively. The biochemistry of various pharmaceuticals can also be studied with appropriate radioisotope labelling.

2.4.2 Positron Emission Tomography Overview

A PET scanner detects the colinear 511 keV annihilation photons produced by radiotracers that are introduced to the body via injection or inhalation. A bolus of radiotracer can be introduced at the beginning of the scan or it may be continuously infused throughout the scanning period. Most PET detectors consist of inorganic scintillators, such as lutetium oxyorthosilicate (LSO) or bismuth germanium oxide (BGO). These materials are ideal for detecting γ-rays since they have high stopping power, fast response, and large light output. Using detectors with higher stopping powers, or linear attenuation coefficients, allows for increased absorption of γ-rays. Scintillators emit visible or near visible light in response to exposure from radiation. Light output is typically coupled to a photocathode that produces electrons proportional to the light input. Subsequently, the signal is amplified within a photomultiplier tube (PMT) and digitized with an analog to digital converter for later processing. Ultimately, the digitized signal is proportional to the initial photon energy absorbed by the scintillator, and this can be related to the radioactivity distribution within the object being imaged with reconstruction techniques.

A ring arrangement of detectors is common in PET brain imaging. Fig-

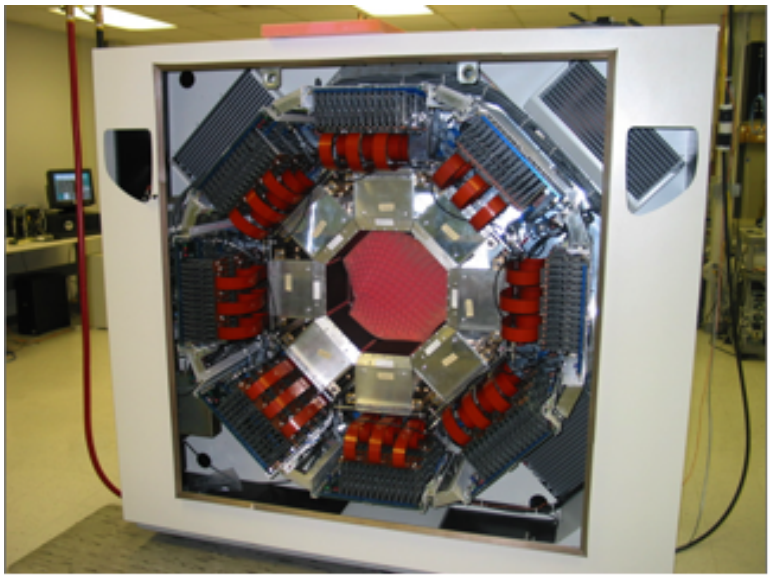

Figure 2.5: Cross-section of High Resolution Research Tomograph (HRRT). Notice the octagonal detector geometry.

ure 2.5 shows the UBC Pet Center's High Resolution Research Tomograph without its casing, revealing its octagonal detector geometry. Patients typically lie supine with the detector ring surrounding the head. Detectors are arranged spatially such that anti-parallel photons can be detected coincidentally. Temporal coincidence is specified by electronic timing windows of less than 10 ns duration that enable localization of the annihilation event to a line connecting opposite detectors. This line is known as the line of response (LOR), and further localization of the annihilation event is prohibited by limited hardware time resolution. When two opposing detectors record the arrival of two photons within the specified timing window, then a coincidence event is counted. By summing several LORs, regions where intersections occur will reflect locations of the original annihilation events. Conjunctively, the distribution of radiotracer within the body can be determined. Figure 2.6 illustrates the basic principle behind annihilation coincidence detection [69].

Factors affecting the inherent spatial resolution of a PET scanner include the finite positron range, non-colinearity of annihilation photons, scintillator size, and the number and density of detector elements. For example, the

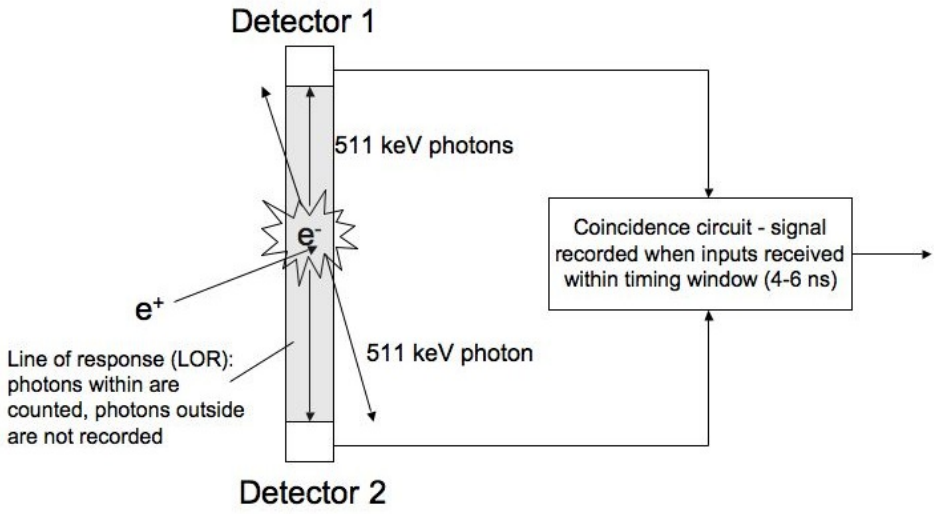

Figure 2.6: Annihilation coincidence detection.

average range of positrons emitted from ^{11}C and ^{18}F (in water) is 1.1 mm and 0.6 mm, respectively. In addition, when electrons or positrons annihilate when not completely at rest, annihilation photons will deviate from colinearity in accordance with momentum conservation. All of these factors act to skew the true LOR and degrade spatial resolution. An empirical description of scanner resolution is

$$FWHM = \sqrt{\left(\frac{d^2}{2}\right) + (0.0022D)^2 + R^2 + b^2} \tag{2.50}$$

where spatial resolution is expressed as the full-width half-maximum (FWHM) of the line spread function, d is detector width, D equals detector cylinder diameter, R equals effective positron range, b is the crystal decoding factor, and $0.0022D$ accounts for decreases in resolution attributable to photon non-colinearity [42].

During list mode data acquisition, detector addresses for a given coincidence event are time stamped to the nearest millisecond. In this manner, a dynamic representation of radiotracer behavior can be described. By fitting these dynamic data, or time activity curves, with models describing the biological processes affecting uptake, entrapment, and clearance of the radiotracer, parameters of clinical interest can be estimated.

2.4.3 Corrections

For meaningful quantitative data analysis, several corrections must be made prior to data reconstruction in order to maximize the correspondence between emitted and detected numbers of photons. Since 511 keV photons suffer primarily from Compton scattering as they travel through tissue, correction factors must be determined to account for photons that are scattered out of the detection range. Attenuation factors for each LOR are calculated by performing a transmission scan before injecting the patient with a radiotracer. An external point or ring source of radiation is moved around the patient in the scanner, and the transmitted intensity is recorded for each LOR. This process is then repeated without the patient in the scanner, and the ratios of the acquired signals enable the determination of attenuation factors for each LOR.

Another form of scatter that contributes significantly to erroneous counts redirects a photon that is subsequently recorded. These events, as well as random coincidences - which occur when photons arising from independent annihilation events are recorded as a single event - lead to events being incorrectly assigned to LORs. Spurious events are also recorded due to the finite energy resolution of the scintillator. Typically, photons within a relatively broad energy range of about 250 to 650 keV are included as coincidence events. Such photons may arise from Compton scattered annihilation γ-rays or may be unscattered, nonannihilation photons. These cases are illustrated in Figure 2.7. Furthermore, corrections for detector dead time and nonuniform responses of the detectors must be determined. These factors can be greatly compensated for by using iterative image reconstruction techniques like those described by Rahmim [51] [69].

2.4.4 Image Reconstruction

Despite being computationally intensive, numerical reconstruction techniques confer many improvements upon final image quality. Many of the physical processes in PET requiring correction can be modeled and included in the iterative reconstruction method. Analytical reconstruction methods, such as filtered back-projection, lack the corrective power associated with iterative techniques and were not used in this study . An iterative statistical, OP-OSEM, method was used for image reconstruction in this study. The estimate of the image is iteratively refined in order to minimize a cost function that provides a measure of the estimated image's correspondence to the true tracer distribution. In addition, this technique enables the inclusion of

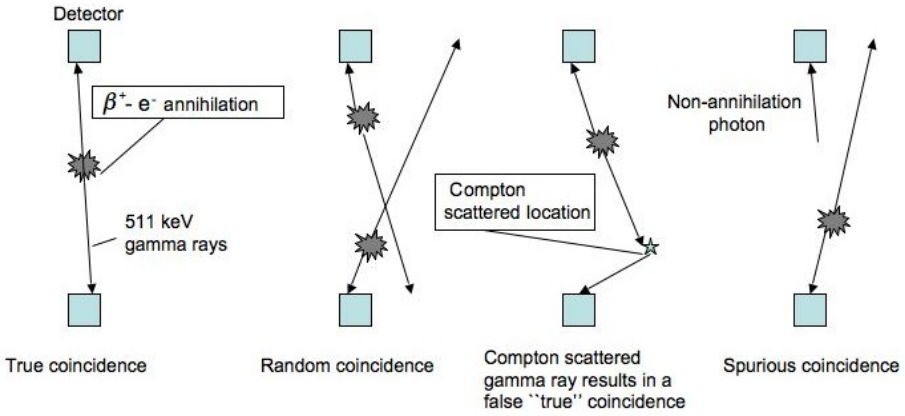

Figure 2.7: Illustration of different events associated with annihilation coincidence detection. Only a "true" coincidence event correctly localizes the annihilation. All other events result in erroneous lines of response and must be corrected for prior or during reconstruction of PET data. Note: LOR recorded as line joining two opposing detectors.

correction factors accounting for scatter, random counts, attenuation, and detector normalization.

2.4.5 Positron Emission Tomography of Brain Tumors with ^{11}C-Methionine

Methionine is considered an essential amino acid, since it cannot be synthesized by humans and it must be ingested in some form. Methionine participates in many biochemical reactions including protein synthesis and methylation reactions, where a methyl (CH_3) group is added to a compound. By substituting one of the carbon atoms of methionine with a positron-emitting carbon atom (^{11}C), the distribution of methionine within the body can be traced with PET. The proper chemical name for this radioactive substitute is called L-[*methyl* -^{11}C]-Methionine or MET for short, and its chemical structure is shown in Figure 2.8 [1].

MET has been used extensively in PET (MET-PET) of primary brain tumors. As MET uptake it is thought to reflect amino acid transport in addition to blood-brain barrier disruption, it may be used for indirect assessment of protein synthesis [11]. More specifically, increased MET uptake

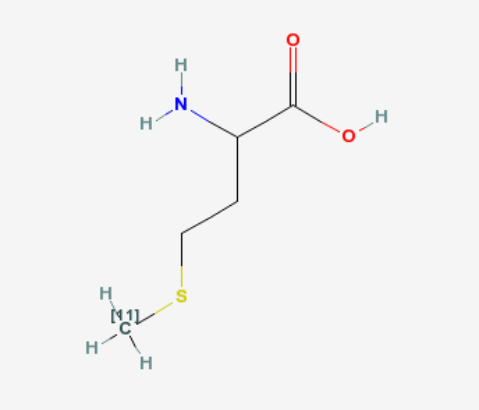

Figure 2.8: Chemical structure of L-[*methyl* -^{11}C]Methionine [1].

is apparently caused by escalated transport mediated by type L amino acid carriers, rather than by direct increases in protein synthesis rates [32]. Increased trans-membrane transport is known to be affected by the cell's requirement for protein synthesis precursors, and hence may be correlated to cellular proliferation and tumor malignancy. The proliferative potential of a tumor may be evaluated by immunohistochemically staining tumor cells for nuclear antigen Ki-67 - which is expressed during proliferative phases of the cell cycle - with mouse monoclonal antibody MIB1. Uptake of MET in gliomas (malignant brain tumors) has been linked to cellular proliferation in cell culture, in vitro Ki-67 expression, proliferating nuclear cell antigen expression, and microvessel density - all of which are features reflecting tumor cell metabolism and proliferation [11, 14, 19, 24, 27, 32, 41, 45].

Due to its low uptake in healthy brain tissue and increased uptake in many types of primary brain tumors, MET is a good tracer for neuro-oncological imaging. In fact, MET is reportedly superior to the widely-used radiotracer ^{18}F-FDG in delineating the extent of gliomas [64]. As normal brain matter has high glucose metabolism, ^{18}F-FDG (FDG-PET) is not ideal for tumor detection - especially for slower growing, low-grade tumors like VSs. FDG is also known to accumulate in abscessed and inflamed regions of tissue that arise after radiotherapy. In response to the local tissue injury inflicted by radiotherapy, a heightened immune response ensues that demands higher energy requirements (and glucose) than normal. Therefore, FDG-PET is apt to be poorly suited for predicting radiotherapy responses [64]. MET has been shown to have high sensitivity in tumor de-

tection, delineation, and differentiation of benign from malignant tumors [11, 14, 19, 27, 32, 45].

In a PET study of gliomas that compared two amino acid tracers, Jacobs et al. [27] reported that MET provided superior sensitivity to primary brain tumor detection versus ^{18}F-FLT (another amino acid radiotracer). All tumors that were visualized with CE-MRI were also detected with MET-PET. Also, the data suggested a larger tumor volume was shown with MET-PET when compared to CE-MRI tumor extent. Accumulation of MET in regions not demonstrating enhancement with CE-MRI indicated that MET-PET is capable of detecting tumor regions that do not present with gross destruction of the BBB. These results confirm the combined mechanisms of BBB disruption and active transport as contributors to MET uptake in neoplastic tissue.

As this study aimed to identify treatment responses of VSs to radiotherapy, an imaging modality capable of distinguishing necrotic or inflamed regions from areas of recurrence would be very useful. Kracht et al. [32] reported that infiltrative regions of low-grade astrocytoma (a type of glioma) showed higher MET uptake than solid tumor regions. Solid regions are generally slower growing, while actively invasive tissue tends to penetrate brain parenchyma and exhibit processes such as cell-cell adhesion, proteolytic remodeling, synthesis of extracellular matrices, and expression or activation of growth factors and integrins. It was hoped that these techniques could be extensible to MET-PET of VSs.

Kubota et al. [33] reported that FDG uptake was high in tumors that had been treated with radiotherapy leading to false positive results for recurrence. Autoradiography findings confirmed high accumulation of FDG in macrophages and young granulation tissue. In contrast to FDG-PET, MET-PET was relatively insensitive to the inflammatory responses of tumor tissue following radiotherapy.

In a separate study, Kubota et al. [34] demonstrated low MET uptake in prenecrotic cells, macrophages, focal necrotic cell debris, and in tissues with extensive areas of necrosis. These results confirmed the potential utility of MET-PET in distinguishing VS recurrence from post-radiotherapeutic events and predicting treatment outcome. It was concluded that MET uptake reflected the presence and extension of viable cancer cells since its uptake in non-tumoral components was relatively low. Furthermore, Ogawa et al. [45] reported increased accumulation of MET in meningiomas (benign brain tumors with characteristics similar to those of VSs), with a concurrent lack of uptake in surrounding edematous tissue. FDG-PET failed to yield lesion enhancement in all but one of the low grade tumors examined.

Also supporting the possible efficacy of MET-PET in distinguishing recurrence from radiation necrosis, Terakawa et al. [60] examined metastatic brain tumors and gliomas post-radiotherapy with MET-PET. The authors concluded the uptake indices tended to be higher for recurrences versus necroses. However, analysis indicated that some necrotic regions demonstrated high MET uptake. It was postulated that the usefulness of MET-PET may be limited in some circumstances where the BBB is not intact, since some necrotic tissues exhibit BBB breakdown.

2.4.6 ^{11}C-Methionine Positron Emission Tomography of Vestibular Schwannomas

In a PET study of VSs, Sakamoto et al. [54] highlighted the challenges of monitoring post-treatment progress due to difficulties in distinguishing residual tumor from scarring and necrosis. No cases were identified with FDG-PET, and 4 of 6 cases were visualized with MET-PET. A heterogeneous pattern of MET accumulation was observed. This could be attributable to preferential uptake of MET in active tumor regions coupled with a lack of MET build-up in necrotic or cystic regions. The lack of MET uptake seen in two tumors was attributed to limitations of scanner resolution. One tumor's diameter ($4\ mm$) was smaller than the scanner's spatial resolution, and one tumor was extremely cystic with little solid tumor tissue.

In a study involving FDG-PET and immunohistology of VSs, Chen et al. [14] reported there was no relationship between FDG uptake and tumor size and recurrence. Using MIB1 staining techniques, there was no correlation found between tumor size and FDG uptake or FDG uptake and MIB1 immunoreactivity. The significance of these results, however, are limited by the study's small sample size of 5 tumors.

Nyberg et al. [44] reported results from a dynamic MET-PET study of meningiomas and skull-based neuromas (VSs). MET uptake was normalized for a given amount of injected radioactivity and patient weight, and then plotted versus time for each case. VSs were noted to have lower uptake ratios (of tumor to cerebellum - the control region) than meningiomas. In addition, uptake in meningiomas was relatively homogeneous while accumulation in VSs tended to be heterogeneous. Regions of heterogeneity were noted to correspond to computed tomography findings, and they were thought to have arisen from small cystic or necrotic regions. This was later confirmed histologically. In the cerebellum, uptake maximized at approximately $2-3$ minutes post-injection. Five minutes post-injection, the mean tumor to cerebellum ratios for meningiomas and VSs were 5.5 and 2.5, re-

spectively. A full separation of the meningioma and VS populations was achieved by simultaneously plotting all tumors' time activity curves. Finally, the authors suggested excluding cystic regions of VSs during analysis to augment differences in uptake between small and large VSs. Inclusion of cystic regions tended to reduce the mean uptake value for a tumor as MET tended to accumulate in solid tumor regions only. This finding further supported the promise of MET-PET in identifying active VS tissue.

Chapter 3

Materials and Methods

3.1 Experimental Design

Potential study candidates were typically identified by a multidisciplinary team during a stereotactic radiotherapy disposition conference at the British Columbia Cancer Agency (BCCA), Vancouver Center. The team that discussed and deemed patients eligible for the study included neurosurgeons, radiation oncologists, neuroradiologists, and medical physicists. The radiation oncologists that primarily cared for patients included: Dr. Richard Shaffer, Dr. Roy Ma, Dr. Alan Nichol, and Dr. Michael McKenzie. All patients received clinical examinations, MRI scans, and audiometric evaluation. Due to the relatively low occurrence of VS, inclusion criteria was kept broad to maximize candidate recruitment. Patients who had been previously treated with microsurgery were included as well as patients with bilateral VSs. Provided that patients were in relatively good health and resided within a reasonable distance from the imaging sites, they were considered as candidates for the study. After candidates had agreed to radiation treatment (either SRS or FSRT), caring physicians requested their voluntary participation in the study.

Informed consent was acquired from all participants, and ethical approval was obtained from the Clinical Research Ethics Board of the University of British Columbia (UBC) in accordance with the Tri-Council Policy Statement: Ethical Conduct for Research Involving Humans [12].

Patients were scanned within 8 weeks prior to receiving treatment, and then scanned at a minimum of 6 months following treatment. One patient received MRI scans only, as the PET tracer was not available for use at that time. Also, one patient received only PET due to MRI incompatibilities. For reasons previously described in Section 2.2, follow-up scans were delayed until 6 months post-treatment to discern true pathological changes from transient effects of radiation treatment. Due to logistical reasons, patients received their scans at separate visits.

The UBC 3T Research Facility was selected as the site for DTI and MRS scanning. As this center did not have a power injector when the study

began, the BCCA was chosen for the DCE-MRI component of the study.

The BCCA 1.5T MRI facility had a power injector that enabled consistent CA delivery. Furthermore, the DCE-MRI scan was easily appended to patients' radiation treatment planning scan, so inconveniencing patients with a second research MRI scan was not necessary.

The High Resolution Research Tomograph (HRRT), situated at the UBC PET Center, was selected as the site for PET imaging. This facility boasts one of the highest resolution PET scanners available in the world. and a dedicated team of experts in the field of positron emission tomography facilitated its use. Radioisotopes were produced at TRIUMF by chemist Salma Jivan following the method of Berger et al. [9], and transported to the UBC PET center via a double-tube underground pneumatic rabbit line.

Nine patients in total participated in the pilot study. One patient did not receive MET-PET, and one patient did not receive DCE-MRI, DTI, or MRS (did receive MPRAGE for radiotherapy planning). General patient data is summarized in Table 3.1.

Table 3.1: Summary Patient Data

Patient No.	Weight (kg)	Age	Sex	Tumor Laterality	Imaging received
1	87.6	60	F	R	MRI
2	104.5	62	M	R	both
3	80.9	78	M	L	both
4	63.6	61	M	R	both
5	78.2	61	M	R	both
6	63.6	57	M	L	both
7	75.0	67	F	R	both
8	40.9	58	F	L	both
9	96.4	74	M	L	PET

3.2 Protocols

3.2.1 Radiotherapy

Patients with serviceable hearing, as defined by a Garner-Robertson Class 1 or 2 hearing level, were treated with FSRT. SRS was prescribed for patients who were functionally deaf on the affected side. Both SRS and FSRT were administered using 6-MV photons from a Varian 2100C LINAC modified for stereotactic dose delivery. After being fitted with a stereotactic head frame

that was secured to the skull's periosteum and then anchored to the treatment couch, SRS patients were typically prescribed a single dose of 12 Gy. 12 radiation fields were usually employed in conjunction with one isocenter to achieve maximal dose conformity. For FSRT, a relocatable stereotactic thermoplastic mask system (BrainLAB AG) with an associated bite-block, occipital impression, and facial Aquaplast was used to minimize head motion for each treatment fraction. The thermoplastic shells were secured to the treatment couch as well to reduce patient motion. The standard dosing scheme was 1.8 Gy in 28 fractions to yield a total dose of 50.4 Gy [61].

3.2.2 3T Magnetic Resonance Imaging

All scans at the UBC MRI Research Centre were acquired using a 6-element sensitivity encoding (SENSE) head coil with a Philips Achieva 3.0 Tesla MRI scanner. Following the acquisition localizing images, single-shot EPI and PRESS were employed for DTI and MRS, respectively. DTI was accomplished with single-shot EPI. In addition to a baseline image without a diffusion-weighted gradient ($b = 0$), four b-values equal to 50, 200, 400, and 600 were used in 6 non-coplanar, non-collinear gradient directions. $T_R = 2441$ ms, and $T_E = 49$ ms. FOV was 224×224 mm, with a slice thickness of 2.2 mm. There were no slice gaps. An acquisition matrix of 100×100 (zero-filled to 256×256) was used with a 90° flip angle.

PRESS was used for single-voxel spectroscopy. $T_R = 3000$ ms or 2000 ms, depending on results obtained. $T_E = 35$ ms, and 1024 samples were acquired per repetition. The number of repetitions or signal averages was 64 or 128 depending on the results seen during scanning. In addition, a chemical shift-selective (CHESS) pulse was employed to suppress signal from water prior to exciting the voxel of interest for spectrum acquisition. In order to apply eddy-current corrections, an unsuppressed spectrum was also taken with the same acquisition parameters as the corresponding, water-suppressed spectrum.

3.2.3 1.5T Magnetic Resonance Imaging

A Siemens Symphony 1.5T MRI scanner was used at the BCCA. Following localizing scans, a fast 3D gradient echo sequence was used for DCE-MRI. Parameters were: $T_R = 4.3$ ms, $T_E = 1.54$ ms, matrix $= 256 \times 154 \times 14$, FOV $= 230 \times 230 \times 21$ mm^3, and flip angle of 15°. Prior to CA injection, a proton density-weighted scan was acquired using the same FLASH sequence with a flip angle of 5° to enable T_1 quantification during analysis. Next, 6

repetitions of the T_1-weighted sequence (flip angle = 15°) were taken prior to injecting the patient with a bolus of 4.8 ml/kg (in solution) Gadovist gadobutrol at a rate of 3 ml/s. Dynamic scanning continued throughout the injection and lasted for 4.25 minutes. The sequence provided a time resolution of 7.29 s. A full-brain Magnetization Prepared Rapidly Acquired Gradient Echo (MPRAGE) sequence (parameters T_R = 1810 ms, T_E = 3.49 ms, matrix = 224×256, FOV = 218.75×250 mm^2 acquired post-CA administration was used as a basis for image co-registration and region of interest analysis.

3.2.4 Positron Emission Tomography

Several days prior to scanning, patients were advised to avoid ingestion of protein-rich foods on the day of the scan. By reducing protein intake, it hoped that some sources of signal variability would be alleviated. In theory, ingested quantities of methionine and other large, neutral amino acids could compete against radio-labelled methionine for uptake by transporter proteins [19]. Patients were fitted with a thermoplastic head mask to reduce motion during scanning and improve reproducibility. After a 10 minute transmission scan, patients were injected intravenously with approximately 15 mCi ^{11}C-Methionine in a 10 ml saline solution. A Harvard pump (power injector) delivered the dose remotely within 60 seconds. Specific patient data is given in Table 3.2.4. Emission scanning began just prior to tracer injection and lasted for 80 minutes. After examining the first data set, the scan length was reduced to 60 minutes since the last 20 minutes of data did not contain signal above the noise level.

Table 3.2: Summary Patient PET Data

Patient No.	Injected Dose (mCi)	Specific Activity (Ci/mM)
2	15.01	2451
3	14.86	4703
4	15.12	10,420
5	10.98	1286
6	15.02	5444
7	14.95	13,644
8	13.53	8113
9	14.89	8811

3.3 Analysis

3.3.1 PET Reconstruction, Image Registration, and Regions of Interest

^{11}C-methionine PET (MET-PET) data were acquired in list mode and reconstructed using an iterative statistical sinogram-based OP-OSEM algorithm. MET-PET data were framed so as to generate adequate time-resolution while maintaining reasonable signal-to-noise. As little literature existed that pertained to optimal framing of MET-PET dynamic data, the framing protocol used for ^{11}C-raclopride dynamic PET studies at the brain research center was adopted after consulting with experienced PET researchers. Framing was: 4×60s, 3×120s, 8×300s, and 1×600s.

All functional image data were registered to full-brain MPRAGE images using FMRIB FLIRT software [28]. Rigid-body registrations were used with either correlation ratio or mutual information cost functions. DTI image data were motion corrected using FLIRT software while DCE-MRI data were not corrected for motion due to inherent difficulties in their registration.

Several regions of interest (ROIs) were defined manually using custom software for both summed MET-PET and MPRAGE images. Tumor ROIs that both included and excluded visibly cystic regions were drawn on MPRAGE. Cystic regions were identified as non-enhancing regions of tumor on MPRAGE. Tumor ROIs were also drawn on summed MET-PET images and included pixels perceived as enhancing or abnormal as compared to the contra-lateral, un-enhancing internal auditory canal. ROIs on the contra-lateral cerebellum and corpus callosum were chosen as gray and white matter controls, respectively, over 3-4 image slices for each patient. ROIs defined on MPRAGE were masked to set all pixels within ROI bounds to 1, then transformed to DTI, DCE-MRI, and PET spaces using inverted registration matrices obtained using FLIRT. ROI masks were re-sampled to functional image space resolutions and interpolated tri-linearly.

3.3.2 Functional MRI Analysis

MRS

The LC Model of S .W. Provencher was used for all single-voxel spectroscopic analysis [49]. A basis set appropriate for 3T MRI scanning and $T_E = 35$ms was used along with eddy-current correction to generate spectra for each patient. Eddy-current correction was accomplished by referencing water-supressed spectra to their corresponding water un-suppressed spectra.

DCE-MRI

To detemine CA relaxivity, 5 phantoms containing known concentrations of Gadovist CA were scanned with variable flip angles of the FLASH scanning sequence described in Section 3.2.3. Flip angles used were: 5, 10, 15, 20, 40, and 60 degrees. Signal intensity curves for ROIs within homogeneous regions of phantom images were plotted as a function of flip angle and fitted with equation 2.26 to detemine T_1 for each given concentration of CA. Relaxivity was determined by fitting a plot of ${T_1}^{-1}$ vs. concentration with equation 2.30.

Arterial input functions (AIFs) were experimentally derived from the anterior inferior cerebellar arteries (AICAs) - one of the main arterial supplies to the internal auditory canal. AICAs for one patient are shown in Figure 3.1 for a dynamic DCE-MRI image. Circular ROIs were drawn on AICAs when they were clearly visible on both tumor and contra-lateral side. An averaged signal intensity from all ROIs was calculated for each patient which was then fitted from the time of injection onwards with a phenomenological linear bi-exponential curve to construct a smooth AIF. Figure 3.2 shows AICA signal intensity fitted phenomenologically for one patient. Further, a population-averaged signal intensities were computed from all patients' AICA ROIs and fitted with the same equation to determine a population-averaged AIF. A population-averaged AIF was calculated in order to investigate the sensitivity of pharmaco-kinetic models to the AIF. Furthermore, the use of a population-averaged AIF could be warranted in situations where an individual AIF is difficult to measure (i.e. an indiscernible AICA). However, there were no such cases in this study to-date. Figure 3.3 shows all patients' AICA signal intensity fits overlaid with the population-averaged AIF fit. It is evident from Figure 3.3 that there is significant variation in the AIFs for different patients.

Two- and three- parameter pharmaco-kinetic (PK) models were fitted to DCE-MRI data to generate pharmacokinetic parameters including K_{trans}, v_e, and v_p using custom software as described in Section 2.3.3, where the experimentally derived AIF was taken as $C_p(t)$. The three-parameter model is given by equation 2.35, while the two-compartment model is simply equation 2.35 with the first term omitted. Fitting was accomplished using mpfit.pro, an IDL function written by Craig Markwardt employing a Levenberg-Marquardt least-squares minimization algorithm [39]. PK parameters were calculated on a pixel-wise basis and also for tumor ROIs that excluded non-enhancing (cystic) regions. Integrated area under the curve for first 60 s post-contrast ($IAUC_{60}$) was calculated both parametrically and for the same

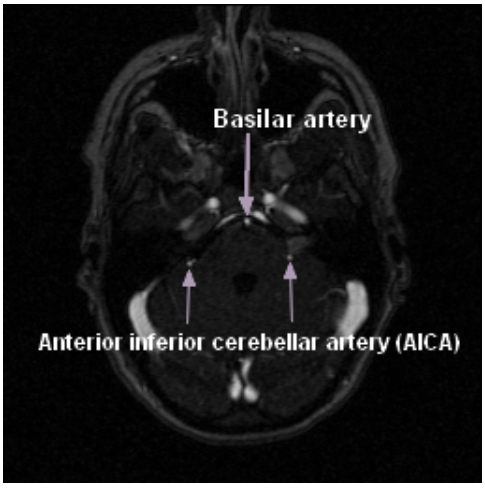

Figure 3.1: Anterior Inferior Cerebellar Artery (AICA) used for arterial input function determination in DCE-MRI pharmaco-kinetic modeling.

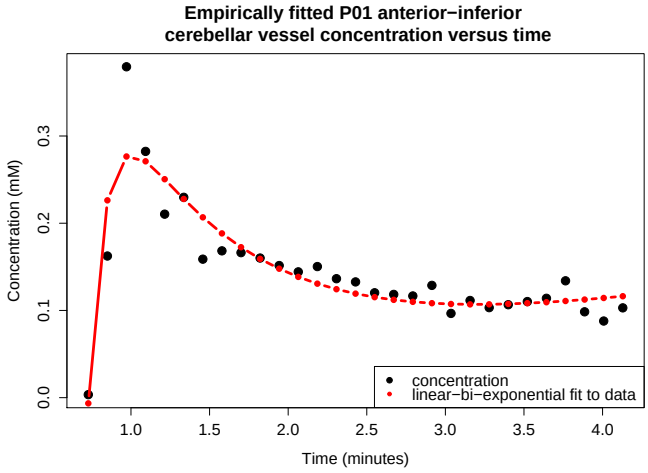

Figure 3.2: Fitted AIF and measured signal intensity for ROI of AICA for one patient.

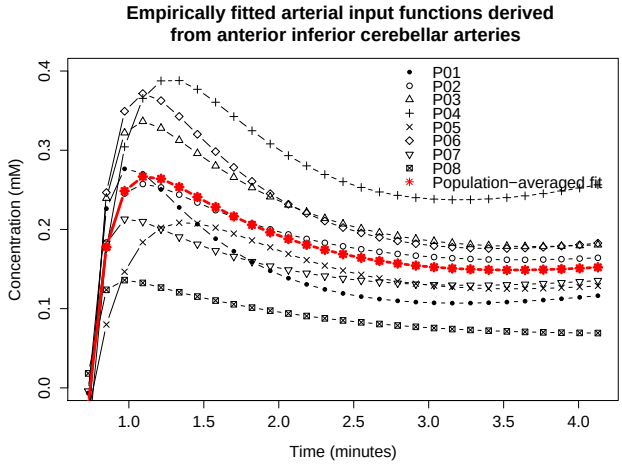

Figure 3.3: Fitted AIFs for all patients with population averaged-AIF for ROI of AICAs.

tumor ROIs with custom software. IAUC_{60} was computed numerically using:

$$IAUC_{60} = \sum_{n=1}^{N} \frac{(C_t(n) + C_t(n-1))(t(n) - t(n-1))}{2} \tag{3.1}$$

where $C_t(n)$ is concentration of CA in tissue at time, $t(n)$, and $t(n)$ is time in seconds. Summation was for $t(n)$ immediately post-CA injection up to $t_n \leq$ 60 s. $IAUC_{60}$ and PK parameter values that were negative or excessively larger than tumor ROI means ($(0 \leq K_{trans} \leq 0.5)$ min^{-1}, $0 \leq v_e, v_p \leq 0.5$) were considered to arise from noise and these pixels were filtered out.

DTI

Pixel-wise maps of mean diffusivity (MD) and fractional anisotropy (FA) were generated by fitting each voxel signal using equation 2.38 with FMRIB's DTIfit software [6]. For instance, a linear fit of:

$$ln\left(\frac{\vec{S}(b_{11})}{\vec{S}(b_{11}=0)}\right) = -b_{11}D_{11} \tag{3.2}$$

for all signals, $\vec{S}(b_{11})$, acquired along one of the six gradient directions denoted as $< 11 >$, with b-values = 0, 50, 200, 400, and 600 gives the diagonal

element of $\vec{D} = D_{11}$ (apparent diffusion coefficient along $< 11 >$ direction). This method is repeated for all six gradient directions to determine the full diffusion tensor. MD and FA were then calculated with equations 2.39 and 4.3, respectively. In addition to pixel-wise maps of MD and FA, mean MD and mean FA were calculated for cystic and non-cystic tumor ROIs, and for cerebellum control ROIs.

3.3.3 PET

Time activity curves for the mean activity per pixel in cerebellum, corpus callosum, and tumor ROIs were examined to determine if tumors exhibited unique activity patterns. Tumor volumes, calculated by multiplying the number of pixels contained within all 2D-ROIs outlining the tumor by the pixel volume, were measured using summed activity MET-PET images and compared to the volumes measured using MPRAGE MRI images that both included and excluded visibly cystic components. In order to correct for varying doses and patient weights, a standardized uptake value was calculated using:

$$SUV = \frac{\text{mean activity per pixel in tumor (mCi)} \times \text{body weight (kg)}}{\text{injected dose (mCi)}} \quad (3.3)$$

where mean activity in the tumor was calculated by manually defining a ROI on summed MET-PET images. SUVs were plotted for tumors as a function of time in order to compare the activities of different tumors. SUVs were also calculated for cerebellum, corpus callosum, and tumor ROIs for summed MET-PET. All calculations were completed with custom IDL software. Fused MPRAGE and summed MET-PET images were generated to aid in examining the variation of enhancement provided by both modalities.

3.3.4 Statistical Analysis

All statistical tests were completed using R, a statistical programming environment [59], and estimation of errors was accomplished using custom IDL software. One or two-sided Student's t-tests at the 95% confidence level were employed to test the equivalence of population means. When testing the equivalence of the means of two populations or samples with a 2-sided Student's t-test, the null hypothesis, H_0, was that the difference between the means was zero, and the alternative hypothesis, H_A, was that the difference between the means was not zero. For a 1-sided Student's t-test, H_0 was the same, but H_A was that the difference between the means was either

greater than or less than zero, as indicated. A probability value (p-value), is defined as the likelihood of observing a test statistic at least as extreme as the one that would be observed if the null hypothesis were true. For all of the Student's t-tests, a significance level of 0.05 was chosen such that a p-value < 0.05 resulted in the rejection of H_0 and the acceptance of H_A (i.e. the difference between the means was considered to be non-zero at the 95% confidence level).

Chapter 4

Results

4.1 Representative Case Studies

Parametric maps for P03 and P08 are presented as representatives of the tumor population. P03 had a tumor that was relatively large (third largest volume in population) and contained cysts, while P08 had a moderately sized tumor (5th largest volume) that did not contain any visible cysts. Parametric maps for K_{trans}, v_e, and v_p were calculated using the patients' individual arterial input functions. All images are presented in radiological orientation as indicated in Figure 4.1. The small, non-enhancing regions in the tumor as exhibited in Figure 4.1 were considered to be cystic or necrotic tissue. These regions were both included and excluded in ROI analyses. Only four patients had tumors with cystic or necrotic components. Further, Figures 4.1 and 4.6 exhibit vestibular schwannomas that have grown into the cerebello-pontine angles and internal auditory canals of both patients.

In order to put parametric results into morphological context, Figures 4.2 and 4.7 (parametric maps) have been registered to full-brain T_1-weighted volumes (for the slices shown in Figures 4.1 and 4.6, respectively). The parametric maps shown in Figures 4.2 and 4.7 are depicted for tumor ROIs that included cystic/necrotic components. As described previously, these ROIs were drawn using post-contrast T_1-weighted images. The parametric maps shown in Figures 4.2 and 4.7 correspond to the tumor ROIs derived from Figures 4.1 and 4.6, respectively.

The variable enhancement observed in Figure 4.1 seems to correspond to the inhomogeneity seen in the parametric maps of Figure 4.2. Non-enhancing tumor regions in T_1-weighted images appear to have correspondingly low values of $IAUC_{60}$, K_{trans}, and v_e. Non-enhancing regions seem to correlate roughly to elevations in v_p and MD, although the signficance of these correlations may be limited by the lower resolution of the functional MRI sequences as compared to the resolution of the T_1-weighted images that were used for definition of ROIs. Despite limits to resolution, a clear pattern of inhomogeneity is evident in the parametric maps for P03. Similar patterns of inhomogeneity were observed for apparently non-cystic tumors

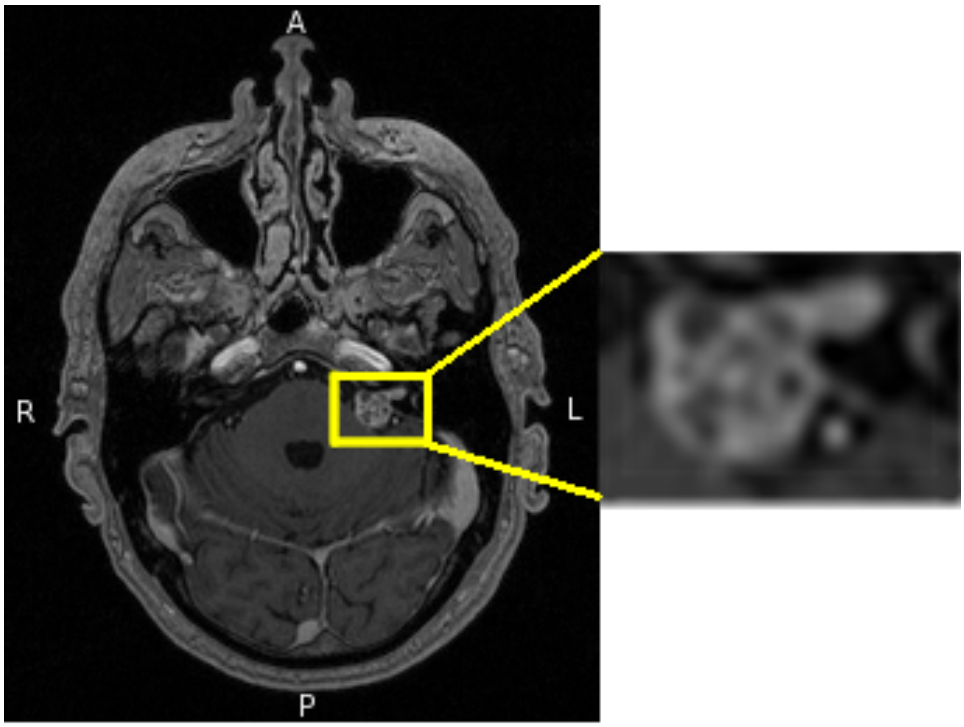

Figure 4.1: Post-contrast T_1-weighted image (MPRAGE) for P03. Tumor enclosed in yellow box and blown up for easier viewing, with radiological orientation directions indicated as: R = right, L = left, A = anterior, P = posterior. Small, non-enhancing regions of the tumor were considered to be cystic or necrotic.

as seen in Figure 4.7.

The fractional anisotropy (FA) maps depicted in Figures 4.3 and 4.8 suggest that there may be some level of anisotropy in VSs. FA maps seem to be rather variable within the tumor regions, perhaps reflecting the inhomogeneous morphological structure of VSs. However, there does not seem to be a clear association between non-enhancing regions (cysts) and reduced FA, as would be expected for aqueous tissue. The lack of this association may be a consequence of the relatively low spatial resolution of DTI (2.24 mm in-plane, without zero-filling) as compared to the T_1-weighted image (0.976 mm in-plane). The effects of cystic regions, due to their smaller sizes, could be overlooked as a result of partial volume effects. Partial volume effects

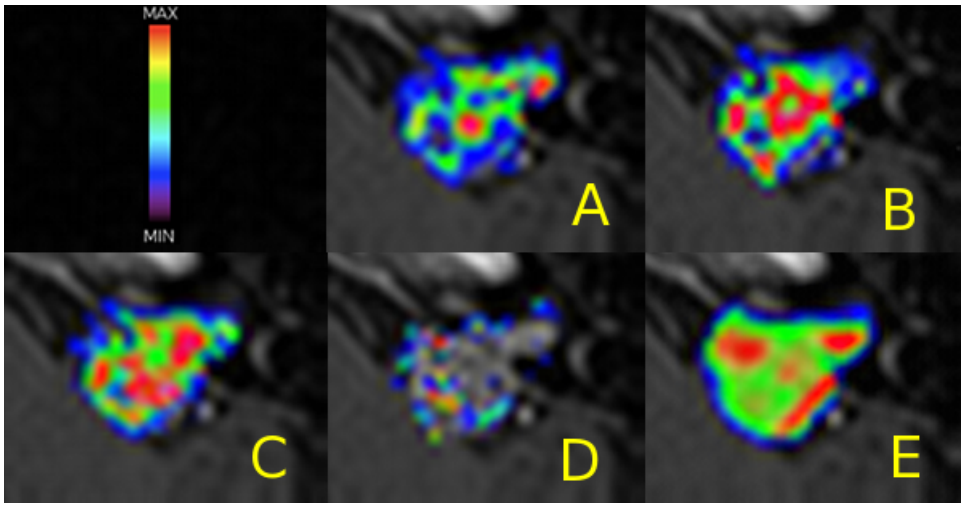

Figure 4.2: A: $IAUC_{60}$ map, B: K_{trans} map, C: v_e map, D: v_p map, and E: mean diffusivity (MD) map for P03 about the tumor region identified in Figure 4.1. This color scale also applies to all (A thru E) parametric maps, although the ranges differ as follows :($0 \leq K_{trans} \leq 0.5$) min^{-1}, $0 \leq v_e, v_p \leq 0.5$. All maps are registered to T_1-weighted images and overlaid on corresponding T_1-weighted slice for morphological reference.

occur when a single voxel contains contributions from a mixture of different tissues. The observed signal is a weighted average of the signals from all tissues contained in the voxel. Partial volume effects are most substantial when the voxel size is large relative to the scale of the tissue of interest (cyst in this case). Much nervous tract structure is visible in the FA maps of Figures 4.3 and 4.8. In particular, the brain-stem appears as a circular, green structure that is medial to the tumor, where green indicates that nerve tracts run along the inferior-superior direction.

Figure 4.4 shows a MET-PET image of summed activity for P03. The color scale used in Figure 4.2 also applies to this image, except highest intensities are shown as gray/white. The central portion of the tumor, with gray/white pixels, exhibits the highest activity, with activity gradually dissipating to the tumor's periphery. The section of the tumor still confined to the internal auditory canal does not demonstrate enhancement on MET-PET. Cysts are not evident in the MET-PET image of Figure 4.4. Since cysts are essentially comprised of a-biotic, fluidic materials, they were not expected to demonstrate much metabolic activity. However, this could sim-

ply be a consequence of the lower resolution of MET-PET (2 mm in-plane), where cysts are under-sampled due to partial volume effects. Other regions of the brain demonstrate marked enhancement under MET-PET for most patients, such as the nasal region and the cerebellum. Some patients also displayed enhancement in gray matter anterior to the cerebellum and the brain-stem. The increased MET uptake seen in nasal tissue is not surprising since this is a rapidly proliferating part of the body. However, the reasons for increased MET uptake that was variably observed in the brain-stem and gray matter are not clear. To qualitatively explore the nature of these tissues' MET uptake, time-activity curves for several ROIs taken from nasal, cerebellum, and tumor tissue were plotted in Figure 4.5. The nasal and cerebellum tissues were selected as controls since they showed enhancement in all patients. These regions were used to compare the uptake patterns observed in tumors to those seen in normal tissues that exhibited MET uptake.

Despite a seeming lack of heterogeneity, the parametric maps for P08 indicate that the tumor exhibits variable properties throughout its volume. In particular, the MD map indicates elevated MD in the medial part of the tumor. The parametric maps seem to provide much more information about the tumor structure than post-contrast T_1-weighted image alone - which implies a homogeneous, highly regular tumor design.

The FA map for P08 is consistent with that observed for all tumors. There is seemingly little organized structure within the tumor, although there are regions that exhibit distinct variations in FA.

Consistent with the trend observed for other tumors, Figure 4.10 shows that regions of high MET-PET activity in tumor tissue tended to enhance later than other highly active regions of the brain, such as the nose and cerebellum. Furthermore, time activity curves for tumors indicated that enhancement peaked, and then persisted without severe metabolic washout for nearly the entire scan duration. Perhaps the most marked feature of MET-PET was the enhancement of all tumors relative to their contra-lateral internal auditory canals. Regardless of their activity level relative to other parenchyma, such as the cerebellum, all tumors enhanced to some extent under MET-PET.

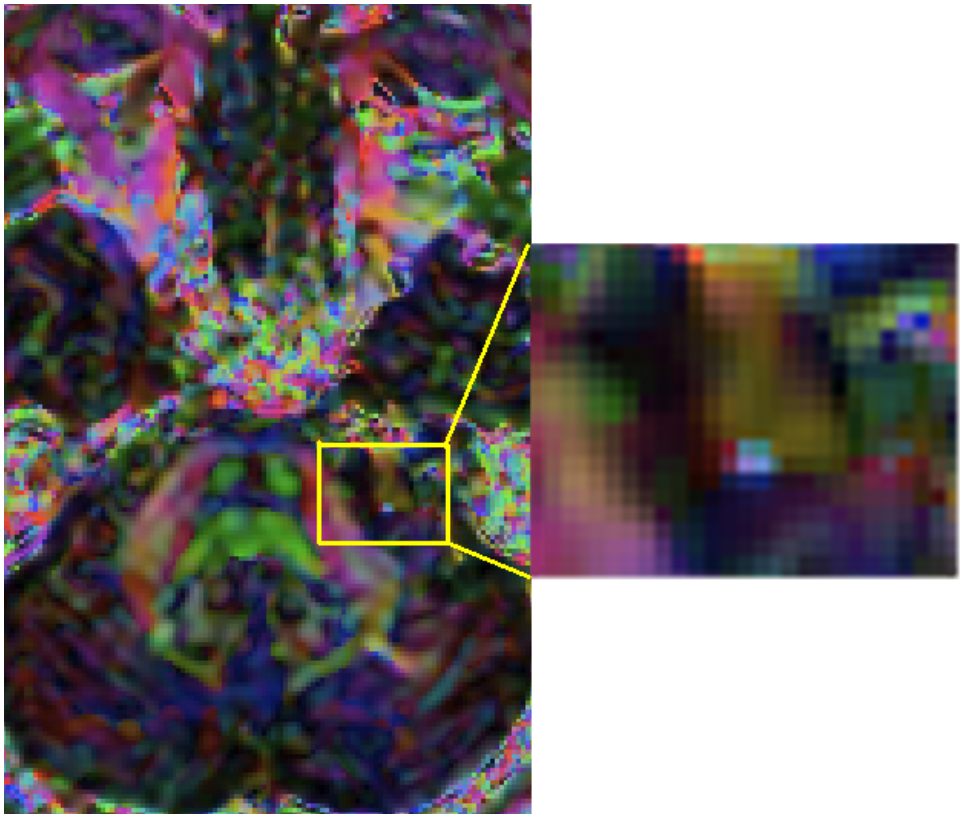

Figure 4.3: Fractional anisotropy (FA) map for P03 modulated with respect to an eigenvector of the diffusion matrix. A yellow box encloses the location of the tumor. Regions where FA is high (close to one) appear opaque, with red, green, and blue indicating principal diffusion along the anterior-posterior , superior-inferior, and right-left directions, respectively. Mixtures of colors indicate principal diffusion along directions that are linear combinations of the principal diffusion directions described. Regions where FA is low (close to zero) appear more transparent.

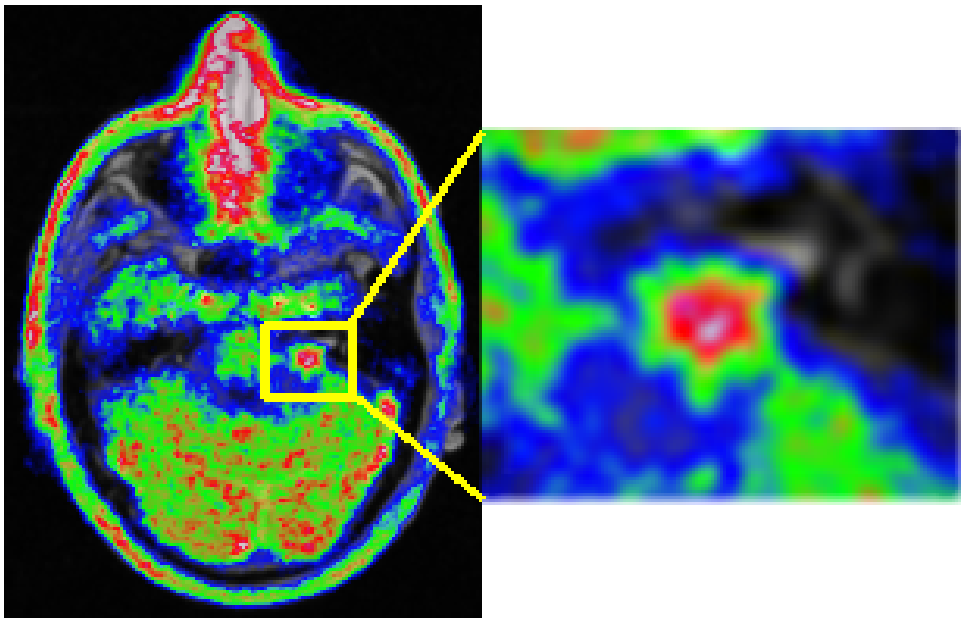

Figure 4.4: MET-PET summed image for P03 overlaid with T_1-weighted image that has been registered to MET-PET space. A color scale for intensity similar to that shown in Figure 4.2 applies to this image with the exception that pixels appearing gray-white (as in the central portion of the tumor and the nose) have the highest activities.

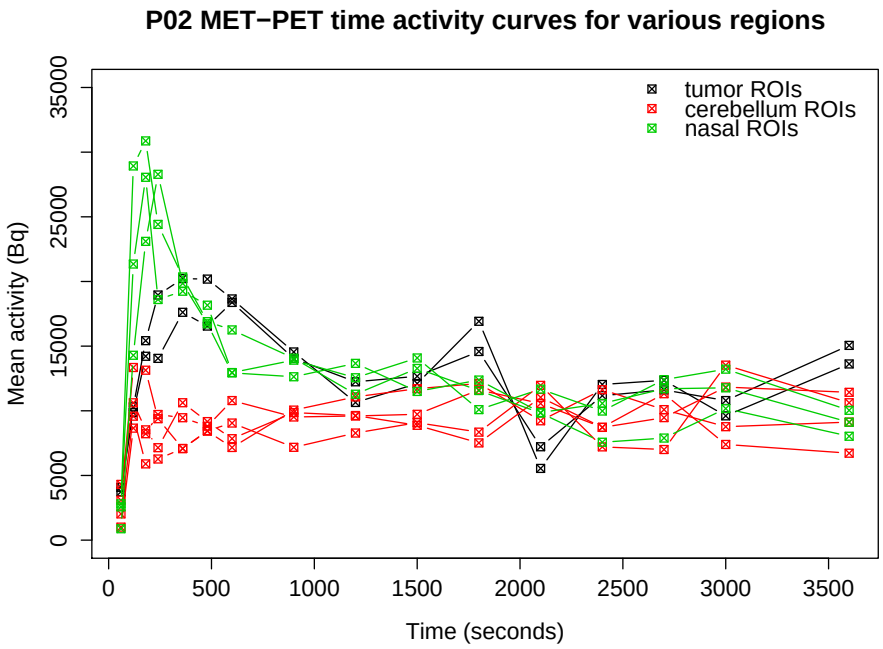

Figure 4.5: Time activity curves for ROIs chosen within various tissues exhibiting increased activity on MET-PET for P03. Tumor ROIs seem to enhance later than both cerebellum and nasal tissues.

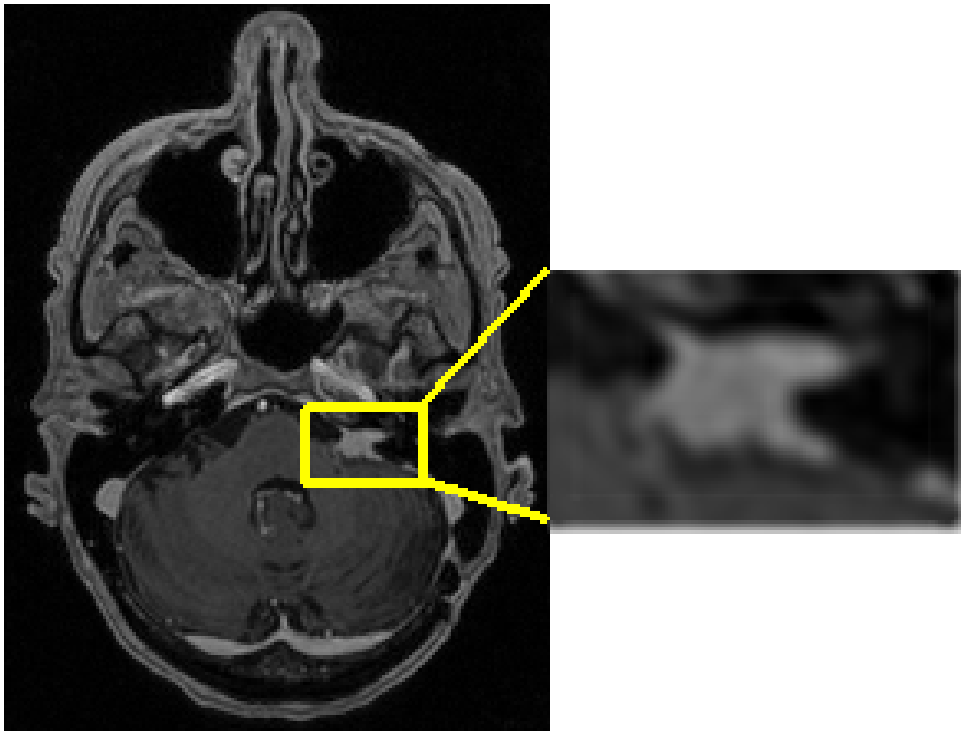

Figure 4.6: Post-contrast T_1-weighted image for P08. Tumor enclosed in yellow box. Unlike the tumor seen in Figure 4.1, this tumor displays homogeneous enhancement.

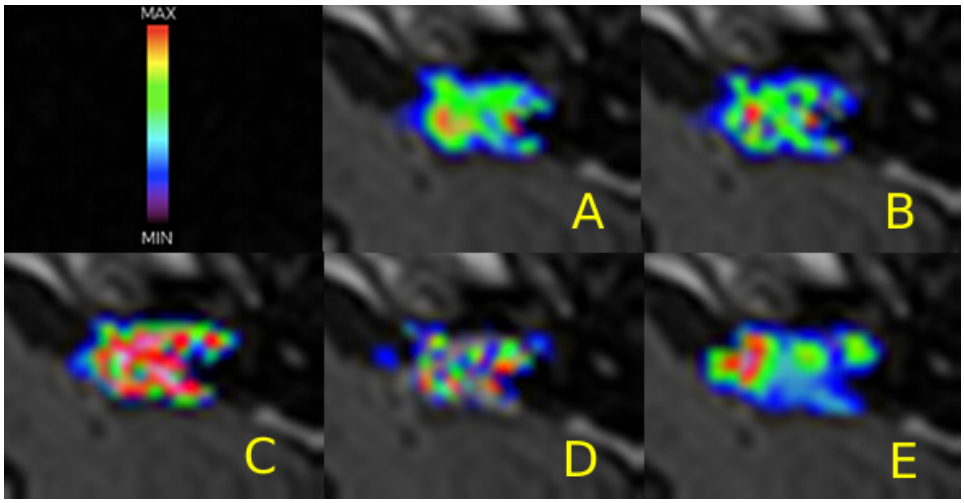

Figure 4.7: A: $IAUC_{60}$ map, B: K_{trans} map, C: v_e map, D: v_p map, and E: mean diffusivity (MD) map for P08 about the tumor region identified in Figure 4.1. This color scale also applies to all (A thru E) parametric maps, although the ranges differ as follows :$(0 \leq K_{trans} \leq 0.5)$ min^{-1}, $0 \leq v_e, v_p \leq 0.5$. All maps are registered to T_1-weighted image and overlaid on corresponding T_1-weighted slice for morphological reference.

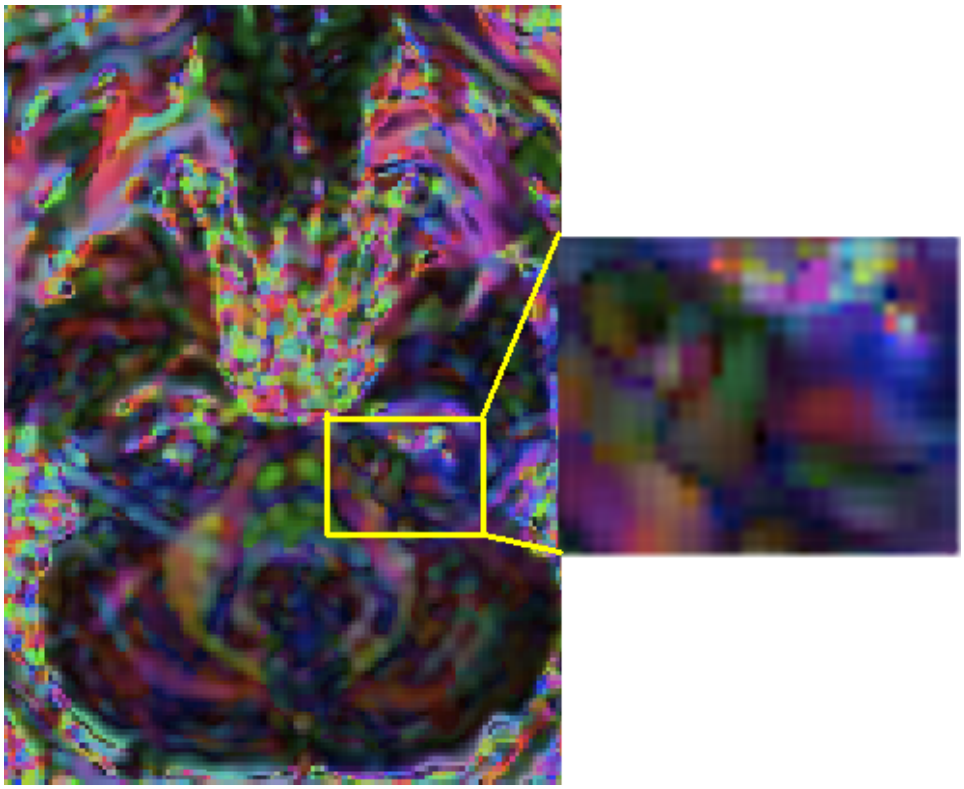

Figure 4.8: Fractional anisotropy (FA) map for P08 modulated with respect to an eigenvector of the diffusion matrix. A yellow box encloses the location of the tumor. Regions where FA is high (close to one) appear opaque, with red, green, and blue indicating principal diffusion along the anterior-posterior , superior-inferior, and right-left directions, respectively. Mixtures of colors indicate principal diffusion along directions that are linear combinations of the principal diffusion directions described. Regions where FA is low (close to zero) appear more transparent.

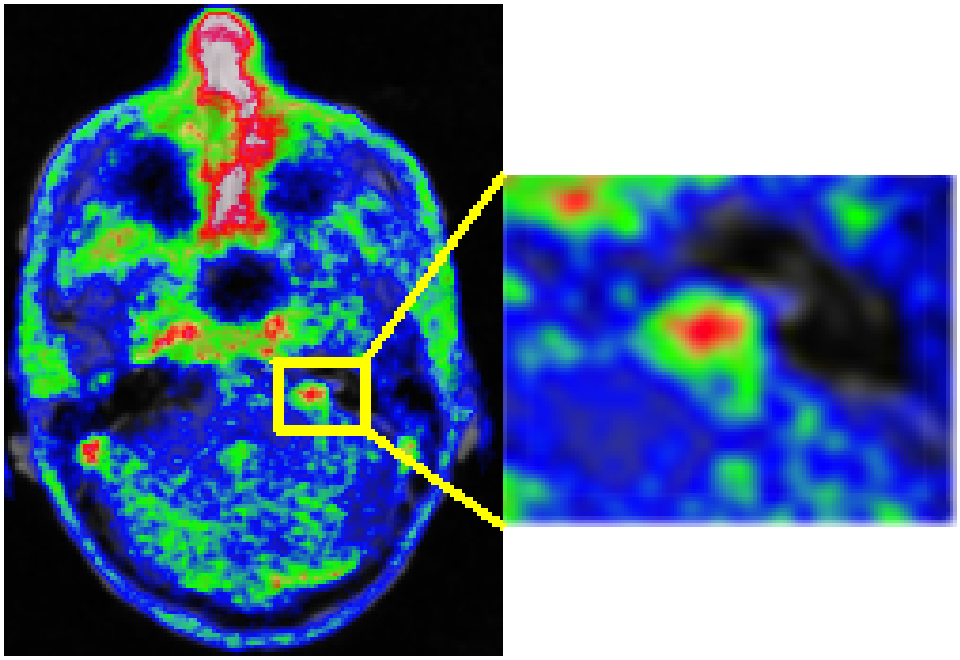

Figure 4.9: MET-PET summed image for P08 overlaid with T_1-weighted image that has been registered to MET-PET space. A color scale for intensity similar to that shown in Figure 4.2 applies to this image with the exception that pixels appearing gray-white (such as the nose) have the highest activities.

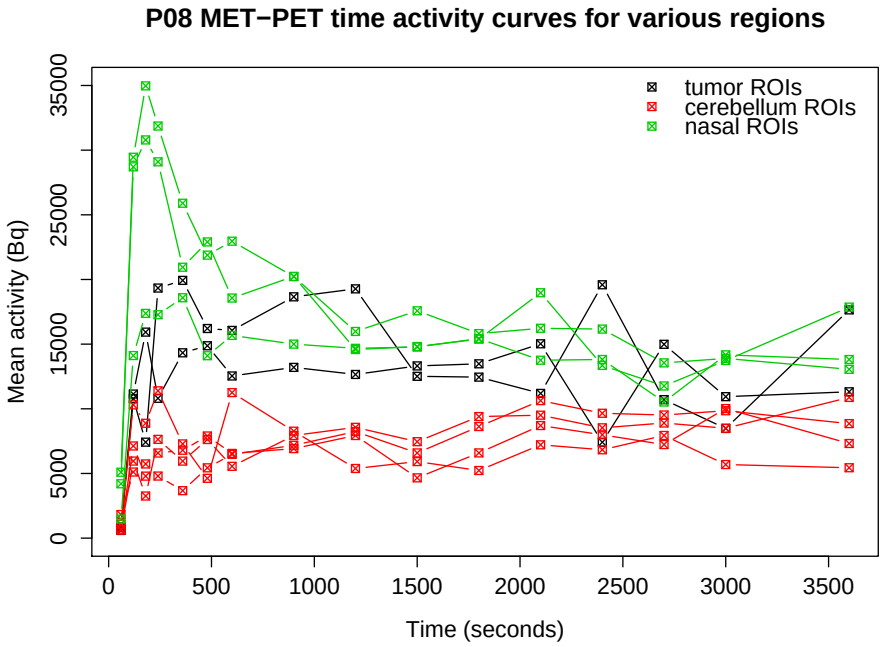

Figure 4.10: Time activity curves for ROIs chosen within various tissues exhibiting increased activity on MET-PET for P08. Tumor ROIs seem to enhance later than both cerebellum and nasal tissues.

4.2 Region of Interest Results

This section presents results obtained using ROIs that both included and excluded visibly cystic portions of tumors. Population means are represented as lines, and P-values are for two-sided Student's t-test, unless otherwise indicated. Furthermore, error-bars on graphs are ± 0.5 standard deviation from the mean of the pixel population comprising the ROI.

4.2.1 DCE-MRI Results

Figure 4.11 presents mean concentration-time curves for all tumor ROIs that excluded non-enhancing regions (presumably cysts). These tumors exhibit initially abrupt, and then gradual increases in concentration of contrast agent. This result is consistent with previous observations [25, 65]. All tumors, with the exception of P06, fail to reach peak concentration levels within the scan duration. Although the prognostic implications of this observation are yet to be identified, the absence of a peak in contrast enhancement could be reflective of a large EES fraction in the vestibular schwannomas examined. Since P06 had one of the smallest tumors in this population, the presence of a peak in the concentration-time curve could indicate that there was a relatively small EES, as compared to the other tumors, for contrast agent to diffuse into. Alternatively, P06 could have unique histological features as compared to the other tumors. However, these propositions remain speculative since there were no histological tests to confirm their validity.

Figure 4.12 shows the average concentration-time curve for P01's tumor ROI with both 2- and 3- parameter pharmaco-kinetic (PK) model fits. 3-parameter model fits are shown with both the individual AIF and population-averaged AIF. For most patients, the 3-parameter model fit the data better than the 2-parameter model. Patient 5 was exceptional, in that the 3-parameter model fit failed (gave v_p value outside of set bounds) when the population-averaged AIF was used. The 3-parameter model fit for patient 5 was successful when the individual AIF was used. Also, despite that both individual and population-averaged AIFs resulted in good 3-parameter model fits to data, they yielded substantially different PK parameters. These differences are shown in Figures 4.14, 4.15, and 4.16 which show the average 3-parameter model fits for each tumor ROI using both individual and population-averaged AIFs. Figure 4.16 shows that the 3-parameter model fit failed for patient 5 when the population-averaged AIF was used. Thus, this result reduces to a 2-parameter model fit for patient 5. Figure 4.16 also indicates the sensitivity of the model fits to the AIF, since patient 5 was

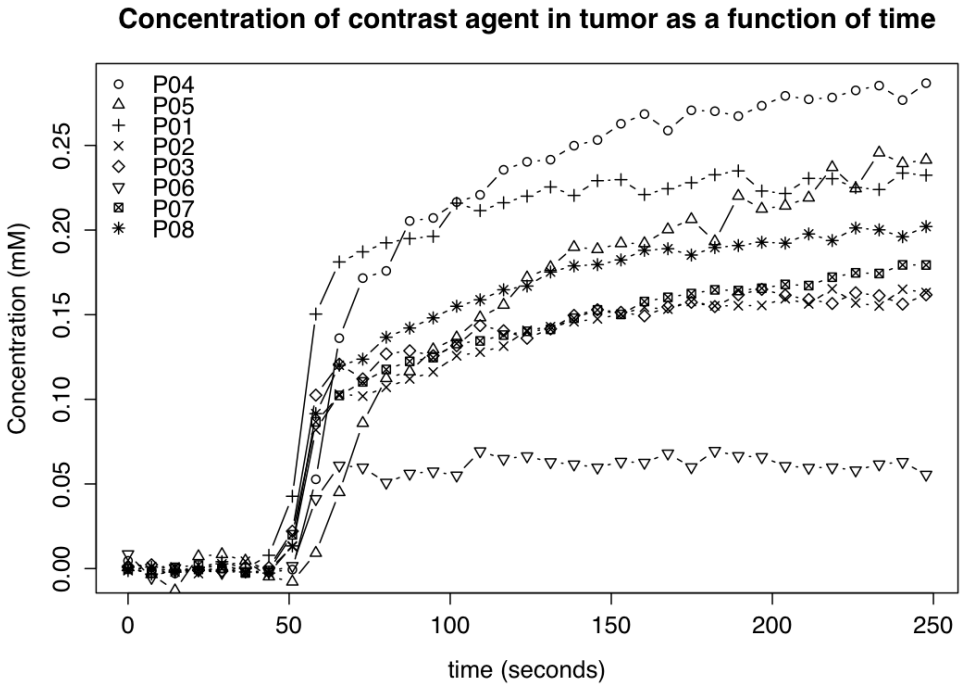

Figure 4.11: Mean concentration-time curves for all tumor ROIs. ROIs excluded non-enhancing tumor regions.

successfully modeled with a 3-parameter fit when the individual AIF was used. Average PK parameter values were calculated by fitting the mean concentration values of each ROI. Mean $IAUC_{60}$ is shown for all tumors in Figure 4.13. Even after excluding visibly cystic components of tumors from the ROIs in this analysis, there seem to be differences between the PK parameters obtained for tumors that did and did not contain visible cysts. For instance, tumors that had cysts (P01, P02, P03, and P07) tended to have reduced mean v_e and elevated v_p relative to non-cystic tumors (P04, P05, P06, and P08). However, this trend is not exactly observed for all patients. Despite showing differences in uptake curves for ROI mean concentrations, tumors tended to accumulate, on average, the same amount of contrast agent 60 s post-injection.

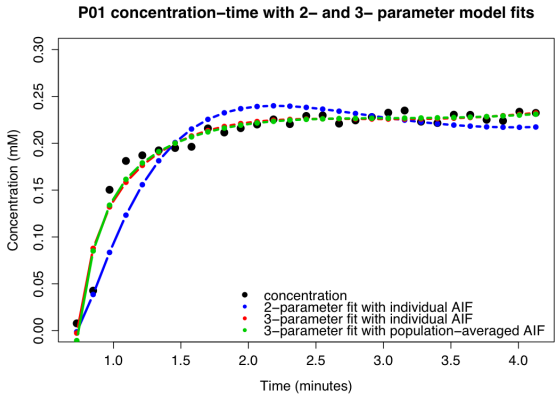

Figure 4.12: Mean concentration-time curve for P01's tumor ROI including 2- and 3- parameter pharmaco-kinetic model fits. Note that 3- parameter model fits are shown for both individual and population-averaged AIFs.

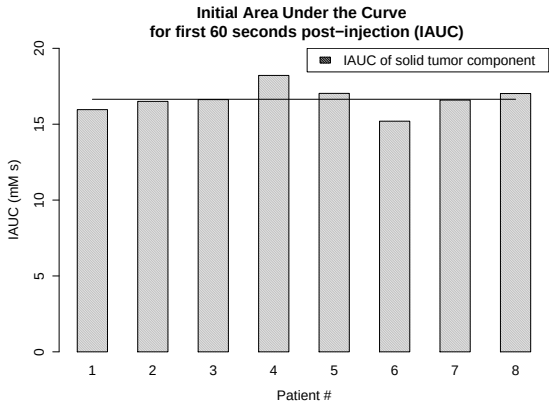

Figure 4.13: $IAUC_{60}$ for mean of concentration of tumor ROIs.

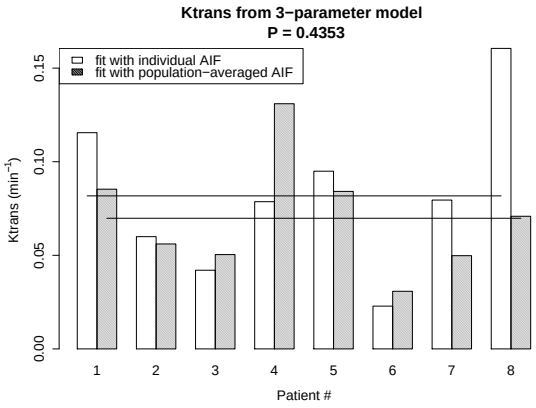

Figure 4.14: Mean K_{trans} for tumor ROIs from 3-parameter fit. P01, P02, P03, and P07 had visibly cystic tumors.

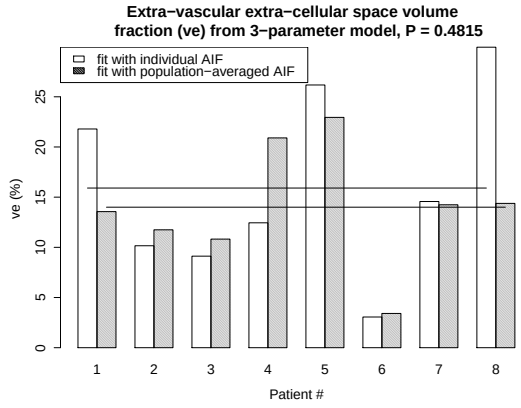

Figure 4.15: Mean v_e for tumor ROIs from 3-parameter fit. P01, P02, P03, and P07 had visibly cystic tumors.

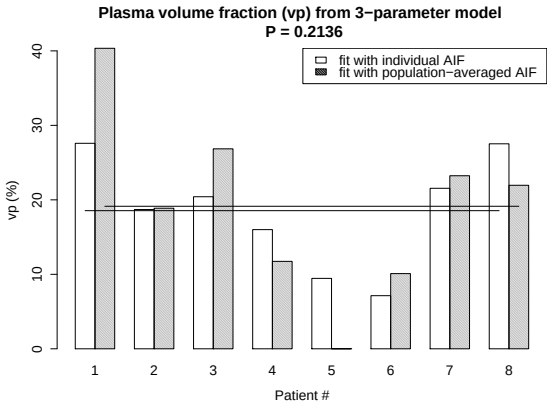

Figure 4.16: Mean v_p for tumor ROIs from 3-parameter fit. P01, P02, P03, and P07 had visibly cystic tumors.

4.2.2 DTI Results

As b-values less than 50 s·mm^{-2} are widely considered to be more sensitive to perfusion effects than larger b-values [35], analyses were completed with b-values $(0, 50, 200, 400, 600)$ s·mm^{-2} and $(50, 200, 400, 600)$ s·mm^{-2}. Since these results did not significantly differ, it can be assumed that the values of mean diffusivity and fractional anisotropy are not strongly affected by perfusion effects. From this point forward, all results are derived from multiple regression of data containing the full set of b-values (0, 50, 200, 400, 600) s·mm^{-2}. Figure 4.17 shows average mean diffusivity (MD) values for tumor ROIs that both included and excluded cystic components. It was hoped that tumor ROIs containing cysts would give elevated values of MD. However, this trend was not observed, and the differences in MD as measured by including and excluding cysts was not significant. This could be because cysts constituted too small a portion of the tumor volume to significantly affect average MDs. Figure 4.21 shows that the cystic component of tumors was quite small ($< 20\%$). In order to detect measurable differences in MD when including and excluding cysts, cysts would need to be large enough ($\sim$ 2.5 mm diameter) to overcome excessive partial volume artifacts, and they would also need to constitute a significant portion of the tumor. The cystic tumors examined tended to have several small cysts with sizes less than the resolution of DTI, which could explain why there is not a significant increase in MD when cystic components are included. It was possible to outline cysts that were smaller than the resolution of DTI, since ROIs were drawn using T_1-weighted MRI images with an in-plane resolution of 0.975 mm. It is reasonable to expect that cysts would display MD values similar to that of water (0.003 mm^{-2}·s). In the best possible scenario, if 20% of a tumor was cystic, and there were no partial volume effects, and assuming that cysts had MD values equivalent to that of water (approximately double the MD of solid tumor), the average MD of that tumor would only increase by about 20%. Since the measurement variability differs by more than this amount, we do not expect to see such small changes in MD based on the inclusion of cysts for these tumors.

Figure 4.18 shows average MD for tumor ROIs that excluded cystic components and average MD for ROIs chosen in the contra-lateral cerebellum. Consistent with previous reports, these VSs show elevated MD values relative to the cerebellum [10, 47, 57]. Larger error bars for tumor ROIs are mostly reflective of tissue heterogeneity, rather than measurement error. The smaller error bars for cerebellum ROIs reflect the more homogeneous nature of that tissue.

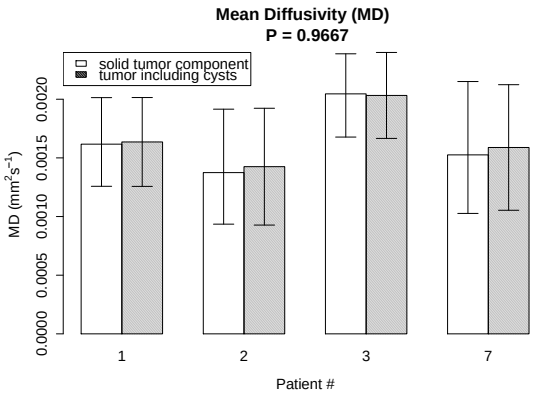

Figure 4.17: Average mean diffusivity (MD) for tumor ROIs that both included and excluded cystic components.

Figure 4.19, showing mean fractional anisotropy (FA) for tumor ROIs, demonstrates again that there are no significant differences to be seen when considering ROIs that either include or exclude visible cysts. The reasons for this could be due to partial volume effects, or may reflect a relatively large noise level in FA. Figure 4.20 fails to show any clear difference between the FA of solid tumor tissue and the contra-lateral cerebellum.

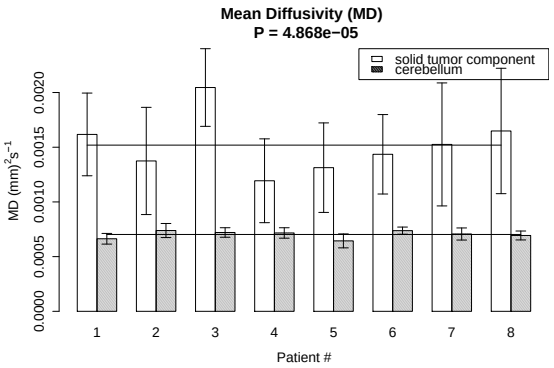

Figure 4.18: Average mean diffusivity (MD) for tumor ROIs that excluded cysts and contra-lateral cerebellum ROIs.

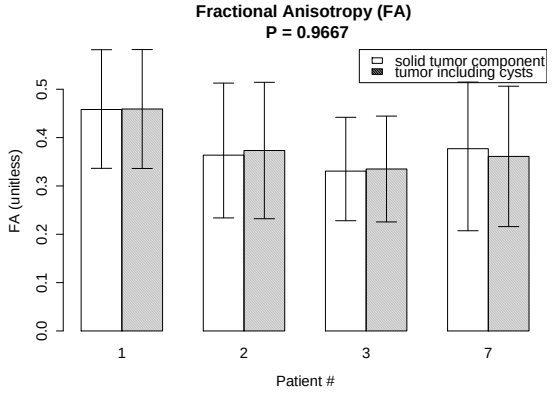

Figure 4.19: Average FA for tumor ROIs that both included and excluded cysts.

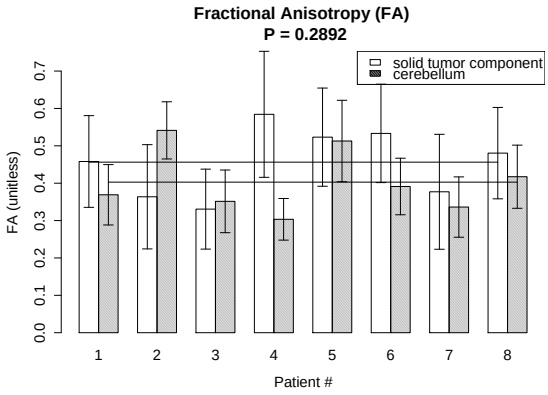

Figure 4.20: Average FA for tumor ROIs that excluded cysts and contralateral cerebellum ROIs.

4.3 MET-PET Results

The inspection of summed MET-PET images revealed that most tumors exhibited uptake in regions that did not identically correspond to the patterns of enhancement on post-contrast T_1-weighted images. In order to quantify the differences in enhancement in T_1-weighted MRI and MET-PET, ROIs were defined on summed MET-PET images where enhanced activity was noted in the tumor. Results for volume measurements of tumors are presented in Figure 4.21 and population means are indicated with horizontal lines. Figure 4.21 reveals that the cystic component of tumors is quite small. The student's one-sided t-test suggested that the population mean for tumor volumes that included cysts, as measured with T_1-weighted MRI, was significantly larger than the population mean for tumor volumes as measured with MET-PET (p-value = 0.04378, at 95% confidence level). The population mean for tumor volumes that excluded cysts, as measured with T_1-weighted MRI, was not significantly different than the population mean for tumor volumes as measured with MET-PET (Student's two-sided t-test, p-value = 0.1544, 95% confidence level). These results indicate that the tumor volumes measured with post-contrast T_1-weighted MRI and MET-PET correspond well when visibly cystic regions of the tumor are excluded from MRI measurements. However, despite that some volume measurements were in good agreement, the locations of activity or enhancement tended to differ in MET-PET and T_1-weighted MRI. In addition, the utility of the comparison of tumor volumes as measured using MRI and MET-PET is limited due to the different spatial resolutions of the two modalities ($\sim$ 1mm and $\sim$ 2.5mm in-plane, respectively). Despite this drawback, most tumor diameters were much larger than the limiting resolution of MET-PET, and the comparisons helped to show general correlations between tumor extent observed on MRI and MET-PET.

In order to compare the amount of MET activity across patients, dynamic standardized uptake values are presented for all tumors in Figure 4.22. Calculation of SUVs is via equation 3.3. Despite normalizing for patient weight and injected dose, tumors exhibit highly variable uptake. However, the pattern of uptake seems to be very similar for all tumors. This pattern of uptake was observed as distinct from that of other highly enhancing regions in the brain, such as the nose (see Figures 4.5 and 4.10).

Figure 4.23 shows average SUV values of tumor, cerebellum, and corpus callosum ROIs defined for summed MET-PET images. Cerebellum may be viewed as a mixed grey/white matter control, and the corpus callosum can be treated as a white matter control. Five of eight tumors displayed

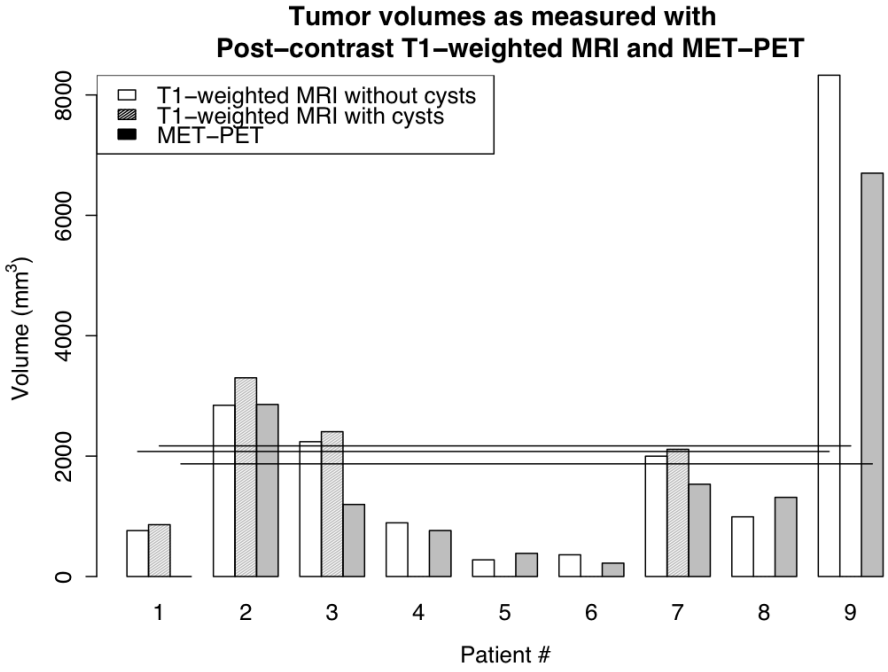

Figure 4.21: Tumor volumes as measured from post-contrast T_1-weighted images and MET-PET.

elevated SUVs relative to the corpus callosum. The absence of an elevated SUV relative to control tissues may not be that useful in evaluating the amount of tumor activity as any amount of tumor enhancement relative to the contra-lateral internal auditory canal is indicative of the presence of pathology.

Pharmaco-kinetic modeling of MET-PET data was contemplated, however, after a careful review of the available literature, the author decided against such modeling. The lack of available information detailing the pharmaco-kinetics of MET in vestibular schwannomas coupled with the absence of arterial sampling rendered well-informed modeling of the MET dynamics impossible for this particular study.

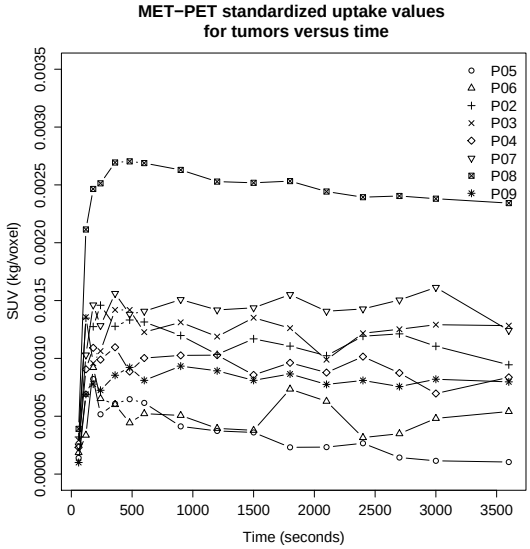

Figure 4.22: Stardardized uptake values (SUVs) for all tumors plotted versus time. Tumor ROIs were derived from summed MET-PET images, and SUV represents mean activity of the tumor normalized for injected dose and patient weight.

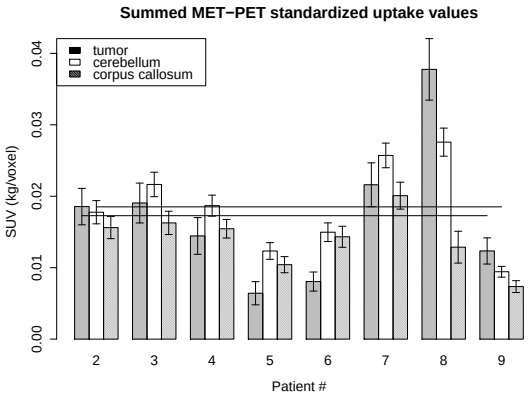

Figure 4.23: SUVs for tumor and control ROIs for summed MET-PET.

4.4 Single-voxel MRS

Single voxel MR spectroscopy was not, in general, successful for these patients. Sources of poor spectra included: small tumor sizes, and therefore low signal-to-noise ratio, and proximity to bone/air cavities that resulted in poor shimming of the main magnetic field. The poor shimming, which most likely resulted from the heterogeneity of the tissues about the tumors (air cavities and bone juxtaposed with soft tissues), frequently resulted in an insufficiently narrow water linewidth. Since the width of the water peak was so large, the CHEmically Selective Saturation (CHESS) sequence employed for water suppression was ineffective in nulling the water signal. Figure 4.24 shows one of the two spectra that were acquired that provided somewhat meaningful results. Significant identifications of metabolites are indicated by red arrows, and descriptions of their physiological relevance are provided in Section 2.1. The fit to the spectrum is plotted as a thick red line, and acquired signal is plotted as a thin, variable black line. The sloping baseline (solid, light black line running under the spectrum) indicates that there is a large water signal that was not adequately suppressed by the CHESS sequence. The residuals are plotted at the top of Figure 4.24. Further, the residuals - defined as the difference between the fitted spectrum and the measured signal - do not appear to be completely random in some regions. Non-random residuals can lead to erroneous fitting of the spectrum with the LCModel. The table to the right of the spectrum provides the abundances of metabolites relative to the amount of creatine (Cr) detected in the voxel. Standard deviation is calculated in LCModel using Cramer-Rao bounds, and values of ≤ 20 % for measured metabolite quantities are usually considered to be significant [49]. These metabolites are highlighted in blue.

Figure 4.25 shows the second meaningful spectrum that was acquired. However, as indicated by the baseline, there appears to be a large lipid contribution that shifts the spectrum upwards near $\sim 1.2 - 2.0$ ppm. The standard deviation of myo-inositol (mI) was slightly high (22%), but it's location is indicated.

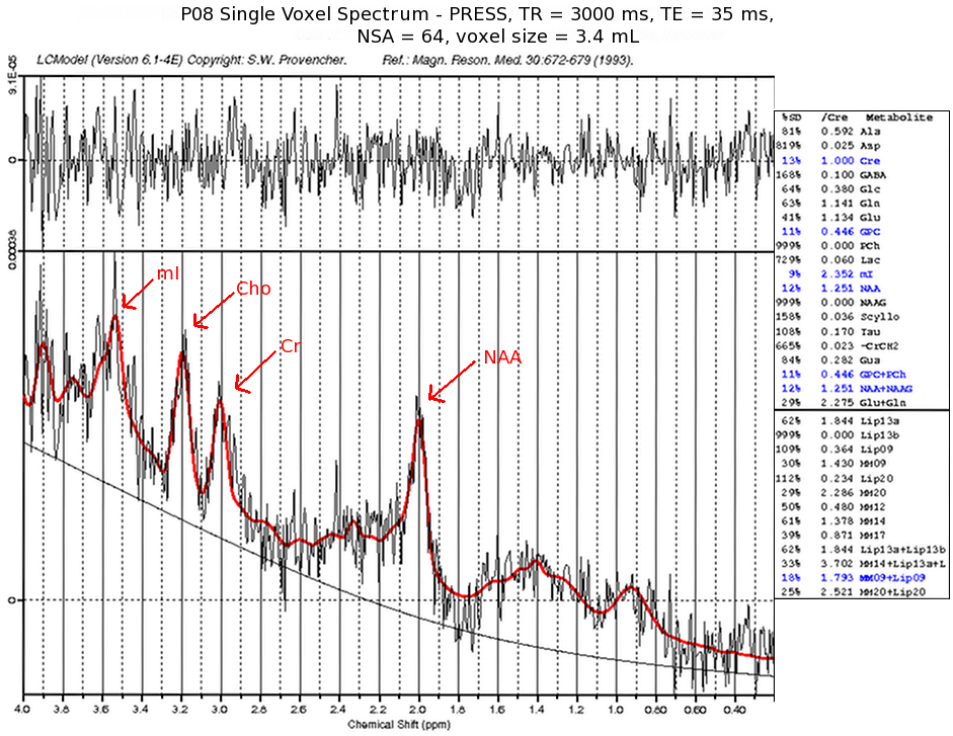

Figure 4.24: PRESS acquired single-voxel spectrum for P08. Metabolites identified using the LCModel are indicated with red arrows. The table to the right displays the ratios of the relative concentrations of metabolites to creatine (Cr). Only metabolites highlighted in blue have acceptable levels of measurement error.

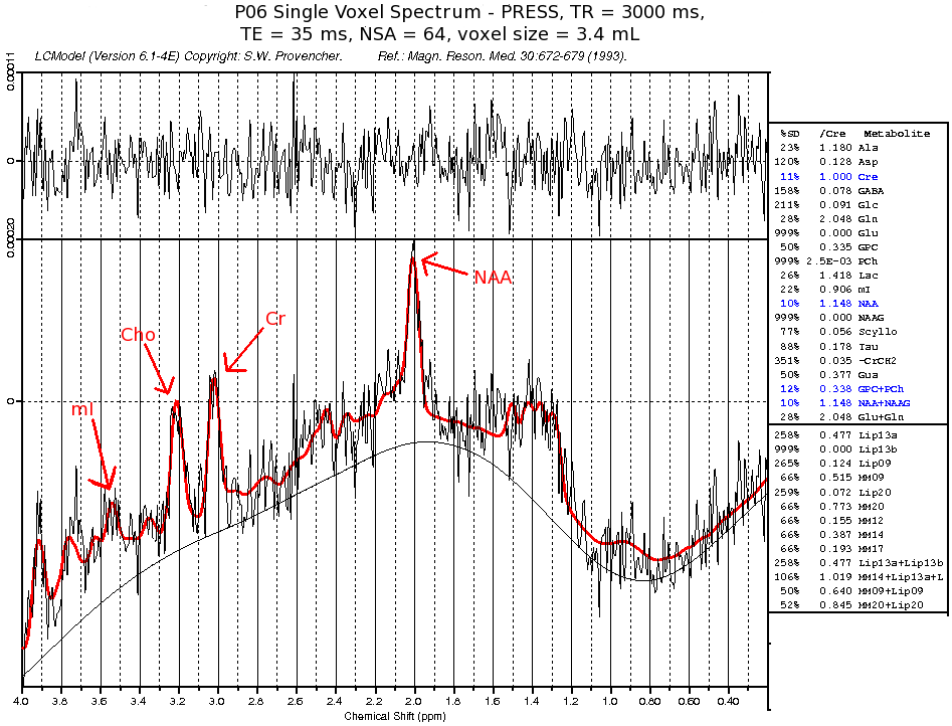

Figure 4.25: PRESS acquired single-voxel spectrum for P06. Metabolites identified using the LCModel are indicated with red arrows. The table to the right displays the ratios of the relative concentrations of metabolites to Creatine. Only metabolites highlighted in blue have acceptable levels of measurement error.

Chapter 5

Discussion

5.1 DCE-MRI

The reduced value of K_{trans} for non-enhancing tumor regions (see Figures 4.2 and 4.7), post-CA administration, reflects that these tumor areas exhibit less blood-brain barrier breakdown (are less leaky) than enhancing portions of tumor. Such regions could be comprised of cystic structures or necrotic tissue. Further, low values of v_e in non-enhancing regions could indicate that these portions of the tumor act to reduce the effective EES volume fraction. In other words, CA does not "see" non-enhancing tissues as they are either walled off (cysts) or impenetrable within the period of observation (necrotic). As seen in Figures 4.2 and 4.7, larger values of v_e are observed in enhancing tumor sections, which could indicate lower cellular density in these regions (i.e. there is a large EES fraction available for CA to leak into). The abundance of zero values for v_p in parametric maps of v_p (Figures 4.2 and 4.7) demonstrates that the 3-parameter model frequently fails to yield physically meaningful values of v_p. This is likely a result of the unavoidable noise that is introduced during pixel-wise parametric modeling. Thus, it seems that v_p is more sensitive to noise than the other parameters, and the 3-parameter model does not seem to provide any information additional to that provided by the 2-parameter model.

Some of the heterogeneity observed in the PK maps does not have clear correspondence to the morphological features seen in T_1-weighted MRI. For this reason, the PK maps suggest that tumor tissue is highly variable and differentiated. PK maps may help to identify changes in tumor pathology post-radiotherapy that cannot be visualized under basic post-contrast morphological MRI. Central tumor necrosis has been extensively documented for VSs following radiotherapy (see Section 2.2.3). Such necrotic regions could be associated with reductions in K_{trans} and v_e as compared to baseline results. Reduced K_{trans} values could reflect the vascular damage and tissue death that frequently results from radiotherapy. Based on these results, reductions in enhancement could manifest as decreases in v_e as there seems to be a positive correlation between enhancement and v_e.

Observed measurements of K_{trans} seem within reason based on previously reported values of K_{trans} for meningiomas (0.04 to 1.4 min^{-1}) [13]. However, the observed range for this population was lower than that observed for meningiomas (0.02 to 0.16 min^{-1}). This difference could be highlighting the pathological differences between these tumors.

$IAUC_{60}$ maps could also reveal changes in tumor vascularity post-radiotherapy. However, due to low inter-patient variability in ROI $IAUC_{60}$ values, this measure may not be as sensitive to pathological response as the other PK parameters. Further, as stated by others, initial-area under the curve simply summarizes information that is already known - namely the concentration time-course of the CA [66]. Despite having a good signal-to-noise ratio, IAUC does not provide insight to the physiological processes effectuating CA kinetics. In monitoring response to radiotherapy, it may be crucial to examine changes at the pixel-level since regional changes in tumor properties could be averaged-out, and consequently overlooked, in ROI analyses. For instance, histograms of parameters for whole tumor volumes could help to identify trends in treatment responses. Since VSs seem to be quite heterogeneous, histogram analyses could enhance sensitivity to detecting changes in tissues post-treatment that may be overlooked by ROI approaches. Figure 5.1 helps to show the heterogeneous nature of VS. T_1-weighted MRI signal intensity for the tumor exhibits asymmetry and does not resemble a straight-forward Gaussian distribution. Mean intensity is 456.155 and standard deviation from mean is 210.843 - again reflecting tumor heterogeneity.

The AIF-dependent variability that arose in DCE-MRI model fitting indicates that modeling is highly sensitive to the AIF chosen. Since changes to local vasculature are likely following radiotherapy, the choice of AIF may be particularly relevant in evaluating response. Differences in PK parameters calculated from individual and population-averaged AIFs reflect the level of individual AIF variation from the population-averaged AIF. However, in situations where there is not a clear vessel from which to measure an individual AIF, the use of the population-averaged AIF yields superior fits as compared to other literature-derived AIFs.

5.2 DTI

Mean diffusivity (MD) maps revealed a highly anisotropic tumor structure. Some regions of the tumor that were apparently homogeneous on T_1-weighted MRI demonstrated variability in their MDs. Again, this sug-

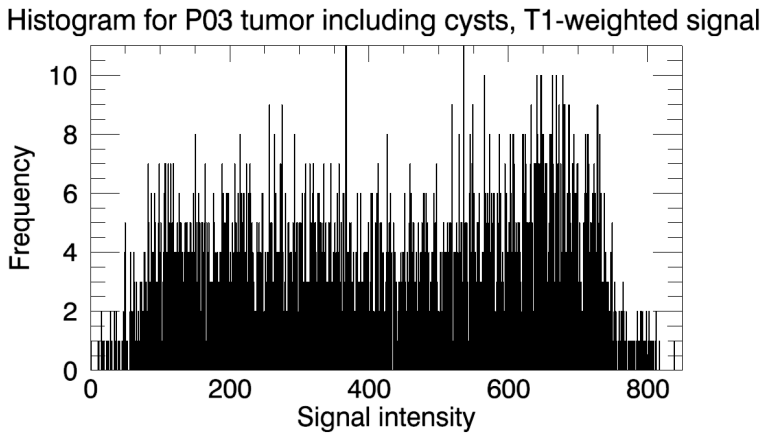

Figure 5.1: Histogram for T_1-weighted signal intensities observed in P03 tumor (including cysts).

gests that results need to be examined at the pixel-level to identify small changes induced by treatment. Histograms of parametric maps could help identify trends in treatment responses. However, all tumors exhibited elevated MD values as compared to cerebellum control ROIs. This indicates that tumor tissue is fairly loose as compared to cerebellar tissue. Tumors with elevated MDs, relative to others in the population, may possess more of the Antoni Type B cellularity, while tumors with lower MDs may consist more of the Antoni Type A cell type. However, coupled with a lack of histological assays, it is impossible to know if this is indeed the case. The onset of wide-spread necrosis post-radiotherapy would likely manifest as a decrease in MD.

Fractional anisotropy (FA) maps and ROI analyses did not reveal any particular pattern for VSs. All tumors tended to exhibit variable amounts of FA, and this could again be reflecting the local variations in tumor tissue that seems apparent from DCE-MRI and MD parametric maps.

5.3 MET-PET

MET-PET results indicated that some segments of tumor were not very active, with respect to MET enhancement. Tumor volumes defined using post-contrast T_1-weighted MRI frequently did not correspond identically to active tumor on MET-PET. This indicates that although certain regions of

the tumor may enhance on post-contrast MRI, they may not exhibit elevated MET metabolism and vice-versa. Thus, despite exhibiting characteristics of BBB breakdown, some tumor regions may not be metabolically active. Since post-contrast MRI is generally used for radiotherapy planning, these results indicate that there are potentially some regions of the tumor being treated unnecessarily, or inadequately. The metabolic information gleaned from MET-PET could see implementation in radiotherapy planning some day. In fact, most intra-canalicular portions of the tumors did not exhibit enhancement. Following successful treatment, one would expect to see reduced levels of MET activity in tumors (especially centrally, where necrosis is typically observed). Although it was difficult to evaluate MET activity in tumor tissue relative to healthy parenchyma, comparing pre-to post- treatment tumor activity should be fairly straightforward. Also, the consistent pattern of uptake seen in all tumors may help to identify particular changes post-treatment. Successfully treated tumors could present with reduced uptake and/or modified uptake patterns. Since all tumors enhanced to some extent under MET-PET, this modality seems particularly promising as a tool with which to evaluate response to radiotherapy.

5.4 Spectroscopy

Single-voxel spectroscopy with PRESS sequence was determined to not be a useful tool to examine VSs with (at least at 3T). Only two of eight spectra gave somewhat meaningful, or interpretable, results. Also, these spectra were far from ideal in that they had large, contaminating lipid and water signals. SVS is problematic for most tumors since they are simply so small. Attempting to exclude non-tumor tissue while maintaining a voxel size that delivers a large enough signal is very difficult. The low signal, coupled with the difficulties of shimming in the tumor region, make SVS particularly challenging. It may be worth attempting SVS again at a 1.5T site where the challenges of shimming are not as great. The two spectra that were acquired, however, did show mI - a metabolite previously identified as unique to VS by Cho et al. [15].

5.5 Summary of author's contributions

The author contributed to the development and implementation of novel functional MRI and MET-PET protocols for imaging vestibular schwannomas. Also, the author assisted in the procurement of ethical approval for

this study by developing and writing the relevant documents for ethics applications. Furthermore, the author regularly organized appointments for patients enrolled in the study and was able to accompany almost all of them to their research scans.

All region of interest analyses, which included statistical analyses of various functional imaging parameters, were completed by the author using custom software written by the author and Stefan Reinsberg for IDL. Image registrations were implemented by the author using custom software written by the author and Stefan Reinsberg for IDL. Existing DCE-MRI models were put into practice using software written by the author for IDL, and the use of the anterior inferior cerebellar artery for the calculation of the arterial input function for DCE-MRI modeling was a new technique that was developed by the author.

DTI analysis was completed with FMRIB's DTIfit software [6] that is in widespread use in the scientific community. Also, the esteemed LC Model of S .W. Provencher was used for all single-voxel spectroscopic analysis [49].

All processing of reconstructed MET-PET data was completed by the author using custom software written by the author for IDL.

Chapter 6

Conclusions

The functional MRI techniques developed for this pilot study seem promising as tools to evaluate vestibular schwannoma (VS) response to radiotherapy. DCE-MRI results indicate that there is a high degree of variability in VS structure, and that DCE-MRI has good potential to display sensitivity to changes induced by treatment. DTI, in particular MD, results further suggest that VSs are heterogeneous in nature, and elevated MDs indicate that they have a relatively loose structure as compared to neighboring cerebellar tissue. It may be important to examine parametric maps when evaluating response to radiotherapy as ROI analyses seem to wash-out important contributions from smaller tumor structures such as cysts. Further, histogram analyses may increase sensitivity to detecting changes in structure post-treatment by taking into account the full-heterogeneity of the tumor.

MR spectroscopy was not, in general, an effective tool for examining VSs. Meaningful spectra were only acquired for two patients, so this modality will not be useful for evaluating tumor response to radiotherapy at 3T. Better results may be obtained with acquisition on a 1.5T scanner.

MET-PET was a highly sensitive imaging technique for VSs. All tumors displayed enhancement under this modality, and tumors seemed to exhibit unique uptake patterns as compared to other enhancing regions of the brain. The tumor volumes defined from summed MET-PET images frequently did not correspond identically to the tumor volumes outlined on MPRAGE MRI. These results indicate that regions of tumor exhibiting blood-brain barrier breakdown do not necessarily have high levels metabolic activity. This modality has excellent potential to evaluate VS response to radiotherapy.

In light of these results, the follow-up protocol for VS patients treated with radiotherapy could benefit from the information obtained with DTI and DCE-MRI. These modalities, in particular, lend themselves to immediate implementation at BC Cancer Agency. DTI analysis could be accomplished on-site, with potentially more-detailed analysis to be completed externally. DCE-MRI analysis would include 2-parameter pharmaco-kinetic modeling with an individually obtained AIF whenever possible as well as initial area

under the curve analysis. MET-PET results seem promising, however, clinical meaning has yet to be fully understood. The true efficacy of these techniques will emerge as follow-up data is collected in years to come.

Bibliography

[1] *In: Molecular Imaging and Contrast Agent Database (MICAD) [database online].*, chapter L-[methyl-11C]Methionine. National Library of Medicine (US), NCBI, Bethesda (MD), 2004.

[2] *Philips Gyroscan Achieva 3.0 Tesla Scanner Manual.* Royal Philips Electronic N.V., Netherlands, 2006.

[3] D.W. Andrews, O. Suarez, H.W. Goldman, M.B. Downes, G. Bednarz, B.W. Corn, M. Werner-Wasik, J. Rosenstock, and W.J.J. Curran. Stereotactic radiosurgery and fractionated stereotactic radiotherapy for the treatment of acoustic schwannomas: comparative observations of 125 patients treated at one institution. *International journal of radiation oncology, biology, physics*, 50:1265–1278, 2001.

[4] K. Asaoka, D.M. Barrs, J.H. Sampson, J.T.J. McElveen, D.L. Tucci, and T. Fukushima. Intracanalicular meningioma mimicking vestibular schwannoma. *AJNR. American journal of neuroradiology*, 23:1493–1496, 2002.

[5] P.J. Basser and D.K. Jones. Diffusion-tensor mri: theory, experimental design and data analysis ? a technical review. *NMR in biomedicine*, 15:456–467, 2002.

[6] P.J. Basser and D.K. Jones. Diffusion-tensor mri: theory, experimental design and data analysis ? a technical review. *NMR in biomedicine*, 15:456–467, 2002.

[7] A. Battaglia, B. Mastrodimos, and R. Cueva. Comparison of growth patterns of acoustic neuromas with and without radiosurgery. *Otology & neurotology : official publication of the American Otological Society, American Neurotology Society [and] European Academy of Otology and Neurotology*, 27:705–712, 2006.

[8] R.D. Beegle, W.A. Friedman, and F.J. Bova. Effect of treatment plan quality on outcomes after radiosurgery for vestibular schwannoma, 2007.

[9] G. Berger, M. Maziere, R. Knipper, C. Prenant, and D. Comar. Automated synthesis of 11c-labelled radiopharmaceuticals: imipramine, chlorpromazine, nicotine and methionine. *The International journal of applied radiation and isotopes*, 30:393–399, 1979.

[10] F. Bonneville, J. Savatovsky, and J. Chiras. Imaging of cerebellopontine angle lesions: an update. part 1: enhancing extra-axial lesions. *European radiology*, 17:2472–2482, 2007.

[11] K. Borbely, I. Nyary, M. Toth, K. Ericson, and B. Gulyas. Optimization of semi-quantification in metabolic pet studies with 18f-fluorodeoxyglucose and 11c-methionine in the determination of malignancy of gliomas. *Journal of the neurological sciences*, 246:85–94, 2006.

[12] Natural Sciences Canadian Institutes of Health Research and Engineering Research Council of Canada. Tri-council policy statement: Ethical conduct for research involving humans., 1998.

[13] S. Cha, L. Yang, G. Johnson, A. Lai, M.-H. Chen, T. Tihan, M. Wendland, and W.P. Dillon. Comparison of microvascular permeability measurements, k(trans), determined with conventional steady-state t1-weighted and first-pass t2*-weighted mr imaging methods in gliomas and meningiomas. *AJNR. American journal of neuroradiology*, 27:409–417, 2006.

[14] J. M. Chen, S. Houle, L. C. Ang, D. Commins, K. Allan, J. Nedzelski, and D. Rowed. A study of vestibular schwannomas using positron emission tomography and monoclonal antibody ki-67. *The American journal of otology*, 19:840–5, 1998.

[15] Y.-D. Cho, G.-H. Choi, S.-P. Lee, and J.-K. Kim. (1)h-mrs metabolic patterns for distinguishing between meningiomas and other brain tumors. *Magnetic resonance imaging*, 21:663–672, 2003.

[16] R. Chopra, D. Kondziolka, A. Niranjan, L.D. Lunsford, and J.C. Flickinger. Long-term follow-up of acoustic schwannoma radiosurgery with marginal tumor doses of 12 to 13 gy. *International journal of radiation oncology, biology, physics*, 68:845–851, 2007.

[17] David J. Collins and Anwar R. Padhani. Dynamic magnetic resonance imaging of tumor perfusion. approaches and biomedical challenges. *IEEE engineering in medicine and biology magazine : the quarterly magazine of the Engineering in Medicine & Biology Society*, 23:65–83, 2004.

[18] S.E. Combs, C. Thilmann, J. Debus, and D. Schulz-Ertner. Long-term outcome of stereotactic radiosurgery (srs) in patients with acoustic neuromas. *International journal of radiation oncology, biology, physics*, 64:1341–1347, 2006.

[19] D.J. Coope, J. Cizek, C. Eggers, S. Vollmar, W.-D. Heiss, and K. Herholz. Evaluation of primary brain tumors using 11c-methionine pet with reference to a normal methionine uptake map, 2007.

[20] T.A. Delchar. *Physics in Medical Diagnosis*. Chapman and Hall, London, UK, 1 edition, 1997.

[21] W.A. Friedman, P. Bradshaw, A. Myers, and F.J. Bova. Linear accelerator radiosurgery for vestibular schwannomas. *Journal of neurosurgery*, 105:657–661, 2006.

[22] E. Mark Haacke, Robert W. Brown, Michael R. Thompson, and Ramesh Venkatesan. *Magnetic Resonance Imaging: Physical Principles and Sequence Design*. Wiley-Liss: John Wiley & Sons, New York, USA, 1 edition, 1999.

[23] E. H. Haselhoff. Optimization of flip angle for t1 dependent contrast: a closed form solution. *Magnetic Resonance in Medicine*, 38:518–9, 1997.

[24] Ming-Chao Huang, Yang-Hsin Shih, Ming-Hsiung Chen, Wen-Yuh Chung, Donald Ming-Tak Ho, Ren-Shyan Liu, Liang-Ming Lee, Chun-I Huang, Liang-Shong Lee, and Henrich Cheng. Malignancy of intracerebral lesions evaluated with 11c-methionine-pet. *Journal of clinical neuroscience : official journal of the Neurosurgical Society of Australasia*, 12:775–80, 2005.

[25] I. Ikushima, Y. Korogi, J. Kuratsu, T. Hirai, S. Hamatake, M. Takahashi, and Y. Ushio. Dynamic mri of meningiomas and schwannomas: is differential diagnosis possible? *Neuroradiology*, 39:633–638, 1997.

[26] Magnetic Resonance Imaging. *Vlaardingerbroek, M.T.; den Boer, J.A.* Springer-Verlag, Heidelberg, Germany, 2 edition, 1999.

[27] A.H. Jacobs, A. Thomas, L.W. Kracht, H. Li, C. Dittmar, G. Garlip, N. Galldiks, J.C. Klein, J. Sobesky, R. Hilker, S. Vollmar, K. Herholz, K. Wienhard, and W.-D. Heiss. 18f-fluoro-l-thymidine and 11c-methylmethionine as markers of increased transport and proliferation in brain tumors. *Journal of nuclear medicine : official publication, Society of Nuclear Medicine*, 46:1948–1958, 2005.

[28] M. Jenkinson and S. Smith. A global optimisation method for robust affine registration of brain images, 2001.

[29] J. Kanzaki, M. Tos, M. Sanna, D.A. Moffat, T. Kunihiro, and Y. Inoue, editors. *Acoustic Neuroma- Consensus on Systems for Reporting Results: Keio University International Symposia for Life Sciences and Medicine*. Springer-Verlag, Tokyo, Japan, 2003.

[30] M. Karpinos, B.S. Teh, O. Zeck, L.S. Carpenter, C. Phan, W.-Y. Mai, H.H. Lu, J.K. Chiu, E.B. Butler, W.B. Gormley, and S.Y. Woo. Treatment of acoustic neuroma: stereotactic radiosurgery vs. microsurgery. *International journal of radiation oncology, biology, physics*, 54:1410–1421, 2002.

[31] Andrew H. Kaye and Edward R. Laws Jr, editors. *Brain Tumors: An Encyclopedic Approach*. Churchill Livingstone(Pearson Professional Ltd.), New York, USA, 1 edition, 1995.

[32] Lutz W. Kracht, Hrvoje Miletic, Susanne Busch, Andreas H. Jacobs, Jurgen Voges, Moritz Hoevels, Johannes C. Klein, Karl Herholz, and Wolf-D Heiss. Delineation of brain tumor extent with [11c]l-methionine positron emission tomography: local comparison with stereotactic histopathology. *Clinical cancer research : an official journal of the American Association for Cancer Research*, 10:7163–70, 2004.

[33] K. Kubota, K. Ishiwata, R. Kubota, S. Yamada, J. Takahashi, Y. Abe, H. Fukuda, and T. Ido. Feasibility of fluorine-18-fluorophenylalanine for tumor imaging compared with carbon-11-l-methionine. *Journal of nuclear medicine : official publication, Society of Nuclear Medicine*, 37:320–5, 1996.

[34] R. Kubota, K. Kubota, S. Yamada, M. Tada, T. Takahashi, R. Iwata, and N. Tamahashi. Methionine uptake by tumor tissue: a microautoradiographic comparison with fdg. *Journal of nuclear medicine : official publication, Society of Nuclear Medicine*, 36:484–92, 1995.

[35] D. Le Bihan, E. Breton, D. Lallemand, M. L. Aubin, J. Vignaud, and M. Laval-Jeantet. Separation of diffusion and perfusion in intravoxel incoherent motion mr imaging. *Radiology*, 168:497–505, 1988.

[36] I. Likhterov, R.M. Allbright, and S.H. Selesnick. Linac radiosurgery and radiotherapy treatment of acoustic neuromas. *Otolaryngologic clinics of North America*, 40:541–70, ix, 2007.

[37] M.E. Linskey. Stereotactic radiosurgery versus stereotactic radiotherapy for patients with vestibular schwannoma: a leksell gamma knife society 2000 debate. *Journal of neurosurgery*, 93 Suppl 3:90–95, 2000.

[38] L.D. Lunsford, A. Niranjan, J.C. Flickinger, A. Maitz, and D. Kondziolka. Radiosurgery of vestibular schwannomas: summary of experience in 829 cases. *Journal of neurosurgery*, 102 Suppl:195–199, 2005.

[39] C. Markwardt. Idl library. 2008.

[40] O.W.M. Meijer, W.P. Vandertop, J.C. Baayen, and B.J. Slotman. Single-fraction vs. fractionated linac-based stereotactic radiosurgery for vestibular schwannoma: a single-institution study. *International journal of radiation oncology, biology, physics*, 56:1390–1396, 2003.

[41] K. Miwa, J. Shinoda, H. Yano, A. Okumura, T. Iwama, T. Nakashima, and N. Sakai. Discrepancy between lesion distributions on methionine pet and mr images in patients with glioblastoma multiforme: insight from a pet and mr fusion image study. *Journal of Neurology, Neurosurgery, and Psychiatry*, 75:1457–62, 2004.

[42] WW Moses, PRG Virador, SE Derenzo, RH Huesman, and TF Budinger. Design of a high-resolution, high-sensitivity pet camera for human brains and small animals. *IEEE Transactions on Nuclear Science*, 44:1487–1491, 1997.

[43] M.D. MOTOHIRO HAYASHI. Current treatment strategy for vestibular schwannoma:. *Journal of neurosurgery*, 105:5–11, 2006.

[44] G. Nyberg, M. Bergstrom, P. Enblad, A. Lilja, C. Muhr, and B. Langstrom. Pet-methionine of skull base neuromas and meningiomas. *Acta Otolaryngologica*, 117:482–9, 1997.

[45] T. Ogawa, A. Inugami, J. Hatazawa, I. Kanno, M. Murakami, N. Yasui, K. Mineura, and K. Uemura. Clinical positron emission tomography

for brain tumors: comparison of fludeoxyglucose f 18 and l-methyl-11c-methionine. *AJNR. American Journal of Neuroradiology*, 17:345–53, 1996.

[46] T. Okunaga, T. Matsuo, N. Hayashi, Y. Hayashi, H.K. Shabani, M. Kaminogo, M. Ochi, and I. Nagata. Linear accelerator radiosurgery for vestibular schwannoma: measuring tumor volume changes on serial three-dimensional spoiled gradient-echo magnetic resonance images. *Journal of neurosurgery*, 103:53–58, 2005.

[47] G. Pavlisa, M. Rados, L. Pazanin, R.S. Padovan, and D. Ozretic. Characteristics of typical and atypical meningiomas on adc maps with respect to schwannomas. *Clinical imaging*, 32:22–27, 2008.

[48] J.R. Perks, E.J. St George, K. El Hamri, P. Blackburn, and P.N. Plowman. Stereotactic radiosurgery xvi: Isodosimetric comparison of photon stereotactic radiosurgery techniques (gamma knife vs. micromultileaf collimator linear accelerator) for acoustic neuroma–and potential clinical importance. *International journal of radiation oncology, biology, physics*, 57:1450–1459, 2003.

[49] S.W. Provencher. Estimation of metabolite concentrations from localized in vivo proton nmr spectra. *Magnetic resonance in medicine : official journal of the Society of Magnetic Resonance in Medicine / Society of Magnetic Resonance in Medicine*, 30:672–679, 1993.

[50] A. Radu, A. Pica, J.-G. Villemure, and R. Maire. [indications and results of stereotactic radiosurgery with linac for the treatment of acoustic neuromas: preliminary results]. *Annales d'oto-laryngologie et de chirurgie cervico faciale : bulletin de la Societe d'oto-laryngologie des hopitaux de Paris*, 124:110–114, 2007.

[51] Arman Rahmim. *Statistical List-Mode Image Reconstruction and Motion Compensation Techniques in High Resolution Positron Emission Tomography (PET)*. PhD thesis, University of British Columbia, 2005.

[52] I. Rutten, B.G. Baumert, L. Seidel, S. Kotolenko, J. Collignon, B. Kaschten, A. Albert, D. Martin, J.-M. Deneufbourg, J.-P. Demanez, and A. Stevenaert. Long-term follow-up reveals low toxicity of radiosurgery for vestibular schwannoma. *Radiotherapy and oncology : journal of the European Society for Therapeutic Radiology and Oncology*, 82:83–89, 2007.

[53] A.I. Saito, C.G. Morris, K. Ito, F. Watanabe, K. Karasawa, W.M. Mendenhall, and Y. Naoi. Comparing size evaluation methods for acoustic neuroma after stereotactic radiosurgery. *Radiation medicine*, 25:339–345, 2007.

[54] H. Sakamoto, Y. Nakai, M. Matsuda, Y. Ohashi, N. Tsuyuguchi, J. Kawabe, T. Okamura, and H. Ochi. Positron emission tomographic imaging of acoustic neuromas. *Acta oto-laryngologica. Supplementum*, 542:18–21, 2000.

[55] Davide Schiffer. *Brain Tumors: Biology, Pathology, and Clinical References*. Springer-Verlag, Heidelberg, Germany, 2 edition, 1997.

[56] M.T. Selch, A. Pedroso, S.P. Lee, T.D. Solberg, N. Agazaryan, C. Cabatan-Awang, and A.A.F. DeSalles. Stereotactic radiotherapy for the treatment of acoustic neuromas. *Journal of neurosurgery*, 101 Suppl 3:362–372, 2004.

[57] R. Nuri Sener. Diffusion magnetic resonance imaging of solid vestibular schwannomas. *Journal of Computer Assisted Tomography*, 27:249–52, 2003.

[58] R. Spiegelmann, Z. Lidar, J. Gofman, D. Alezra, M. Hadani, and R. Pfeffer. Linear accelerator radiosurgery for vestibular schwannoma. *Journal of neurosurgery*, 94:7–13, 2001.

[59] R Development Core Team. 2008.

[60] Y. Terakawa, N. Tsuyuguchi, Y. Iwai, K. Yamanaka, S. Higashiyama, T. Takami, and K. Ohata. Diagnostic accuracy of 11c-methionine pet for differentiation of recurrent brain tumors from radiation necrosis after radiotherapy. *Journal of nuclear medicine : official publication, Society of Nuclear Medicine*, 49:694–699, 2008.

[61] C. Thomas, S. Di Maio, R. Ma, E. Vollans, C. Chu, B. Clark, R. Lee, M. McKenzie, M. Martin, and B. Toyota. Hearing preservation following fractionated stereotactic radiotherapy for vestibular schwannomas: prognostic implications of cochlear dose. *Journal of neurosurgery*, 107:917–926, 2007.

[62] P. S. Tofts. Modeling tracer kinetics in dynamic gd-dtpa mr imaging. *Journal of Magnetic Resonance Imaging*, 7:91–101, 1997.

[63] Paul Tofts. chapter Quantitative MRI of the Brain: Measuring Changes Caused by Disease, pages 299–339. John Wiley and Sons Ltd., 2003.

[64] K. Torii, N. Tsuyuguchi, J. Kawabe, I. Sunada, M. Hara, and S. Shiomi. Correlation of amino-acid uptake using methionine pet and histological classifications in various gliomas. *Annals of nuclear medicine*, 19:677–683, 2005.

[65] T.J. Vogl, M.G. Mack, M. Juergens, C. Bergman, G. Grevers, T.F. Jacobsen, J. Lissner, and R. Felix. Skull base tumors: gadodiamide injection–enhanced mr imaging–drop-out effect in the early enhancement pattern of paragangliomas versus different tumors. *Radiology*, 188:339–346, 1993.

[66] S. Walker-Samuel, M.O. Leach, and D.J. Collins. Evaluation of response to treatment using dce-mri: the relationship between initial area under the gadolinium curve (iaugc) and quantitative pharmacokinetic analysis, 2006.

[67] F. Yamasaki, K. Kurisu, and K. Satoh. Apparent diffusion coefficient of human brain tumors at mr imaging. *Radiology*, 235:985–991, 2005.

[68] S.-Y. Yang, D.G. Kim, H.-T. Chung, S.-H. Park, S.H. Paek, and H.-W. Jung. Evaluation of tumour response after gamma knife radiosurgery for residual vestibular schwannomas based on mri morphological features. *Journal of neurology, neurosurgery, and psychiatry*, 79:431–436, 2008.

[69] Pat Zanzonico. Positron emission tomography: a review of basic principles, scanner design and performance, and current systems. *Seminars in nuclear medicine*, 34:87–111, 2004.

Appendices

Ethics Certificates

The University of British Columbia
Office of Research Services
Clinical Research Ethics Board – Room 210, 828 West 10th Avenue, Vancouver, BC V5Z 1L8

ETHICS CERTIFICATE OF EXPEDITED APPROVAL: AMENDMENT

PRINCIPAL INVESTIGATOR:	DEPARTMENT:	UBC CREB NUMBER:
Stefan A Reinsberg	UBC/Science/Physics and Astronomy	H07-00156

INSTITUTION(S) WHERE RESEARCH WILL BE CARRIED OUT:

Institution	Site
UBC	Vancouver (excludes UBC Hospital)

Other locations where the research will be conducted:
Recruitment at BCCA MR scanning at UBC High-Field MRI Centre Data analysis: UBC High-Field MRI Centre & Department of Physics

CO-INVESTIGATOR(S):
Megan M. J. Burns
Roy Ma

SPONSORING AGENCIES:
- Natural Sciences and Engineering Research Council of Canada (NSERC) - "MR methods development for imaging biological systems"
- UBC Dean of Science - "New faculty start up grant"

PROJECT TITLE:
Functional MRI of acoustic neuroma, pre and post stereotactic irradiation

REMINDER: The current UBC CREB approval for this study expires: June 2, 2009

AMENDMENT(S):	AMENDMENT APPROVAL DATE:
Addition and deletion of study team members.	**September 10, 2008**

CERTIFICATION:
In respect of clinical trials:
1. The membership of this Research Ethics Board complies with the membership requirements for Research Ethics Boards defined in Division 5 of the Food and Drug Regulations.
2. The Research Ethics Board carries out its functions in a manner consistent with Good Clinical Practices.
3. This Research Ethics Board has reviewed and approved the clinical trial protocol and informed consent form for the trial which is to be conducted by the qualified investigator named above at the specified clinical trial site. This approval and the views of this Research Ethics Board have been documented in writing.

The amendment(s) for the above-named project has been reviewed by the Chair of the University of British Columbia Clinical Research Ethics Board and the accompanying documentation was found to be acceptable on ethical grounds for research involving human subjects.

Approval of the Clinical Research Ethics Board by:

Dr. James McCormack,
Associate Chair

The University of British Columbia
Office of Research Services
Clinical Research Ethics Board – Room 210, 828 West 10th Avenue, Vancouver, BC V5Z 1L8

ETHICS CERTIFICATE OF EXPEDITED APPROVAL: AMENDMENT

PRINCIPAL INVESTIGATOR:	DEPARTMENT:	UBC CREB NUMBER:
Stefan A Reinsberg	UBC/Science/Physics and Astronomy	H07-00206

INSTITUTION(S) WHERE RESEARCH WILL BE CARRIED OUT:

Institution	Site
UBC	Vancouver (excludes UBC Hospital)
Vancouver Coastal Health (VCHRI/VCHA)	UBC Hospital

Other locations where the research will be conducted:
Recruitment at BCCA PET scanning at UBC PET Centre Data analysis: UBC Department of Physics

CO-INVESTIGATOR(S):
Don Wilson
Vesna Sossi
Montgomery Martin
Megan M. J. Burns
Thomas J. Ruth
Roy Ma

SPONSORING AGENCIES:
N/A

PROJECT TITLE:
Assessment of Treatment Response of Acoustic Neuromas using PET Imaging

REMINDER: The current UBC CREB approval for this study expires: June 3, 2009

AMENDMENT(S):	AMENDMENT APPROVAL DATE:
Addition of Study Team Member and Primary Contact	**September 12, 2008**

CERTIFICATION:
In respect of clinical trials:
1. The membership of this Research Ethics Board complies with the membership requirements for Research Ethics Boards defined in Division 5 of the Food and Drug Regulations.
2. The Research Ethics Board carries out its functions in a manner consistent with Good Clinical Practices.
3. This Research Ethics Board has reviewed and approved the clinical trial protocol and informed consent form for the trial which is to be conducted by the qualified investigator named above at the specified clinical trial site. This approval and the views of this Research Ethics Board have been documented in writing.

The amendment(s) for the above-named project has been reviewed by the Chair of the University of British Columbia Clinical Research Ethics Board and the accompanying documentation was found to be acceptable on ethical grounds for research involving human subjects.

Approval of the Clinical Research Ethics Board by:

Dr. Stephen Hoption Cann,
Associate Chair